Observational Study of Lightning Index Using Radar-Derived Parameters of Cloud-Microphysical Properties in Thunderstorm

積乱雲のレーダ観測から導出した雲微物理的特徴を用いた発雷指数の観測的研究

Syugo Hayashi

Department of Aerospace Engineering
Graduate School of System Design
Tokyo Metropolitan University

Abstract

Lightning is a significant cause of human injuries and casualties, as well as house and forest fires. Electronic devices, which have become increasingly important in information-oriented societies in recent years, are damaged by lightning strikes. Furthermore, lightning strikes interfere with aircraft operations, including ground services. Progress in lightning prediction is required to improve human life, traffic, and aviation safety. It is necessary to clarify the relationship between electrification and microphysical properties in thunderstorms for more accurate lightning prediction and nowcasting. Although direct observations such as radiosonde can obtain detailed particle distribution and electric field intensity data in a thunderstorm, it is difficult to use for operational lightning prediction because of its low frequency and limited observation area. Therefore, it is necessary to quantitatively evaluate the thunderstorm electrification that causes lightning by applying the latest remote sensing technology.

In this thesis, the relationship between cloud microphysical properties derived from radar observation and lightning activity from a lightning location system is investigated to reduce the risk of lightning strikes; new lightning indices that lead to improved lightning forecasting and nowcasting using real-time radar remote sensing data are proposed.

Using conventional radars in operation, the relationship between the radar-derived parameters of thunderstorms and lightning activity was investigated. With and without lightning, these characteristics were observed in July 2010 during a day with severe thunderstorms and lightning in the Kanto Plain, central Japan, and statistically analyzed using radar observations with a cell tracking technique. Observed cells were categorized into cells including cloud-to-ground lightning (CG) and intra-cloud lightning (CGIC cell), cells containing only intra-cloud lightning (IC cell), and cells without lightning (NoL cell). These cells were compared to the average and temporal evolutions of the radar observations. Of the 265 identified cells, 103 were CGIC cells, 30 were IC cells, and 132 were NoL cells. Significant differences in the average value of the cell categories were detected in the following parameters: lifetime, size, echo top, vertically integrated liquid (VIL), maximum radar reflectivity, and radar reflectivity at the − 10 °C isotherm height. The temporal evolution of CGIC cell characteristics revealed changes in radar reflectivity

at 0 °C and − 10 °C, synchronized with the lightning activity. The VIL value was elevated only in CGIC cells and tended to decrease with time as the lightning activity. CGIC cells produced the highest echo top and maintained their height during their lifetime. To predict CG within 20 min using "35 dBZ radar reflectivity at − 30 °C" as the criterion, a critical success index (CSI) of 0.82 and false alarm rate (FAR) of 0.64 obtained the best prediction scores.

Using dual-polarization Doppler radar with the hydrometeor classification algorithm (HCA) and lightning location system, radar-derived microphysical properties related to lightning flash rate were further investigated, and new lightning indices were proposed. The ten isolated thunderstorm cases for 2017 and 2018 over the Kanto Plain, Japan, with 351 radar volume scans every 5 min of the Narita airport weather radar during the summer period, were investigated. The ice-related particles within the 35 dBZ volume (V35IC) showed the highest correlation coefficient (r = 0.75) and the lowest normalized root mean square error (NRMSE = 8.3%) in relation to cloud-to-ground lightning (CG) and intra-cloud lightning (IC, r = 0.69, NRMSE = 8.1%). The correlation between the V35IC and CG flash rate was better than that of the mixed-phase (between 0 °C and − 40 °C) 35 dBZ volume (r = 0.64), without considering the microphysical particles. The second-best radar-derived microphysical property was the ice mass consisting of the radar grids of all ice-related particles (ALICMS, r = 0.72). These results suggest that an effective lightning index from the radar-derived properties requires information on ice-related particle volume added to the traditionally used hail and graupel volume or radar reflectivity volume. The ice-related particle volume in the colder region of the thunderstorm (air temperature lower than −10 °C) showed a higher correlation with CG and IC than that in the warmer region, especially in the IC. These results are consistent with the non-inductive charging theory, which has been well accepted for thunderstorm electrification in previous studies. In the time-lag correlation analysis from 0 to −30 min every 5 min before thunderstorm initiation, the ice-related index V35IC demonstrated the slowest decrease (r = 0.75–0.65 in 30 min) in the correlation coefficient with elapsed time. These results encourage the application of V35IC to a lightning nowcast index.

Acknowledgments

I would like to express my gratitude to my supervisor, Professor Shoken Ishii, Tokyo Metropolitan University, for his sincere guidance and valuable advice for this dissertation. I would also like to acknowledge Professor Tomoo Ushio, Osaka University, for his valuable comments on this study.

I am very grateful to Dr. Fumiaki Fujibe, Dr. Nobuhiro Nagumo, Mr. Akihito Umehara and Ms. Chizuru Nakaike for their support and meaningful discussions. I would like to thank the Japan Metrological Agency observatory department for providing cell-tracking data for research purposes.

I would like to dedicate my special thanks to Dr. Yoshinori Yamada, Dr. Tadashi Fujita, Dr. Akihiro Hashimoto, and Dr. Shunichi Watanabe of the Meteorological Research Institute for their discussion and comments.

Finally, I wish to thank my family, Shoko and Mikoto, for their support and encouragement throughout my study.

Contents

List of Figures

List of Tables

Acronyms

ALICMS	ice mass of ALICV [kg]
ALICV	all ice-related (cloud ice, snow, graupel and hail) particle volumes [km^3]
CAPE	convective available potential energy [J kg^{-1}]
CIN	convective inhibition [J kg^{-1}]
CG	cloud-to-ground lightning
CGp	positive polarity CG
CSI	critical success index
DRAW	Doppler radar for airport weather
EL	equilibrium level [hPa]
FAR	false alarm rate
GHMS	ice mass of graupel or hail [kg]
GLM	geostationary lightning mapper
GHV	graupel or hail volume [km^3]
GV	graupel volume [km^3]
HCA	Hydrometeor classification algorithm
IC	intra-cloud lightning
JMA	Japan Meteorological Agency
K_{DP}	specific differential phase shift [deg km^{-1}]
LCL	lifting condensation level [hPa]
LFC	level of free convection [m] or [hPa]
LIDEN	lightning detection network in Japan
LMA	lightning mapping array
LNB	level of neutral buoyancy [m]
NIC	non-inductive charging mechanism
NLDN	National Lightning Detection Network in US
NRMSE	normalized root mean square error
PoD	probability of detection

TITAN	Thunderstorm Identification, Tracking, Analysis, and Nowcasting
TTL	total lightning (summation of CG and IC)
TRMM	Tropical Rainfall Measuring Mission
VOL35	mixed-phased volume of radar reflectivity greater than 35 dBZ [km^3]
V35IC	ice-related particles volume of radar reflectivity greater than 35 dBZ [km^3]
V40IC	ice-related particles volume of radar reflectivity greater than 40 dBZ [km^3]
V35F	above freezing level volume of radar reflectivity greater than 35 dBZ [km^3]
V40F	above freezing level volume of radar reflectivity greater than 40 dBZ [km^3]
VIL	vertically integrated liquid [kg m^{-2}]
WWLLN	Word Wide Lightning Location Network
Z_{DR}	differential reflectivity [dB]
Z_{hh}	radar reflectivity in horizontal polarization [dBZ]
Z_{vv}	radar reflectivity in vertical polarization [dBZ]
Ψ_{DP}	differential phase between copolar received signals [deg]
ϕ_{DP}	propagation differential phase [deg]
ρ_{hv}	co-polar correlation coefficient

Chapter 1
General introduction

1.1 Background

1.1.1 Lightning

Lightning is an electrical phenomenon in the atmosphere and a significant cause of human injuries and casualties, as well as house and forest fires. Curran et al. (2000) showed that lightning was the second leading cause of weather-related casualties in the United States from 1959 to 1991. The National Weather Service (2020) documented that lightning was the fourth leading cause of weather-related casualties in the 30 years from 1990 to 2019. They also reported that the average annual casualties due to lightning in the United States were 41 over the last 30 years. In Japan, the National Police Agency (2010) also reported 14 causalities in the five years from 2005 to 2009. Electronic devices have become increasingly important in information-oriented societies in recent years and are significantly damaged by lightning strikes. Furthermore, lightning interferes with aircraft operations, including ground operations. In addition, lightning frequency is expected to increase in the future owing to climate variability (Romps et al. 2014). Therefore, there is a high social interest in accurate lightning predictions.

It is usually observed that lightning is associated with developed cumulonimbus, also called "thunderstorm." In the 18th century, Benjamin Franklin proved that lightning is an electrical phenomenon in the atmosphere. The initiation of lightning discharge requires an electric field in the atmosphere to increase beyond the critical electric field. This process is achieved by increasing the electric field owing to the charges accumulated in the thunderstorm. The main charge carriers in a thunderstorm are ice-phase particles such as hail, graupel, snow, and ice crystals (MacGorman and Rust 1998). Some laboratory studies have shown that thunderstorm charges are provided by a non-inductive graupel-ice collision mechanism (e.g., Reynolds et al. 1957; Takahashi 1978; Jayaratne et al. 1983). In a laboratory experiment, Takahashi (1978) showed that electric charges are generated by the collision between graupel and ice crystals, and

that the amount of electric charges generated is affected by the ambient air temperature and the amount of cloud liquid water content (Fig. 1.1). Each charged particle generated by collision has a different terminal falling velocity depending on its shape and size, which causes a spatial bias in the particle distribution in the thunderstorm. Takahashi (1984) estimated the charge amount for each particle type by the numerical simulation of a thunderstorm. According to his results, the electric field exceeds the discharge field in the atmosphere (340 kV m^{-1}, Gunn 1948). His simulations also show that the bias of the spatial distribution of charged particles determines the charge distribution in the thunderstorm, intensifies the electric field, and initiates lightning discharge. The charge distribution in his simulation, with positive charges due to ice crystals in the upper part of the thunderstorm, negative charges due to hail in the middle part, and a small number of positive charges in the lower part, was consistent with the results of in-situ observations (Fig. 1.2, e.g., Simpson and Scrase 1937; Williams 1989). It is now widely accepted that the non-inductive charging mechanism (NIC) proposed by Takahashi (1978) and other researchers (e.g., Jayaratne et al. 1983; MacGorman and Rust 1998; Mansell et al. 2005) is the primary charge generation process in thunderstorms.

Methods for measuring the particle distribution and the magnitude of the electric field in a thunderstorm are very limited and include direct observation with a radiosonde (e.g., Marshall and Rust 1991; MacGorman et al. 2005). In addition to the typical tri-pole structures, more complex polarity structure and inverted di-pole structures have been observed (e.g., Stolzenburg et al. 1998; Rust and MacGorman 2002; MacGorman et al. 2005). It remains difficult to quantitatively observe the particle distribution and space charge distribution in a thunderstorm in real-time. Therefore, the quantitative evaluation of thunderstorm electrification that causes lightning by applying the latest remote sensing technology is challenging.

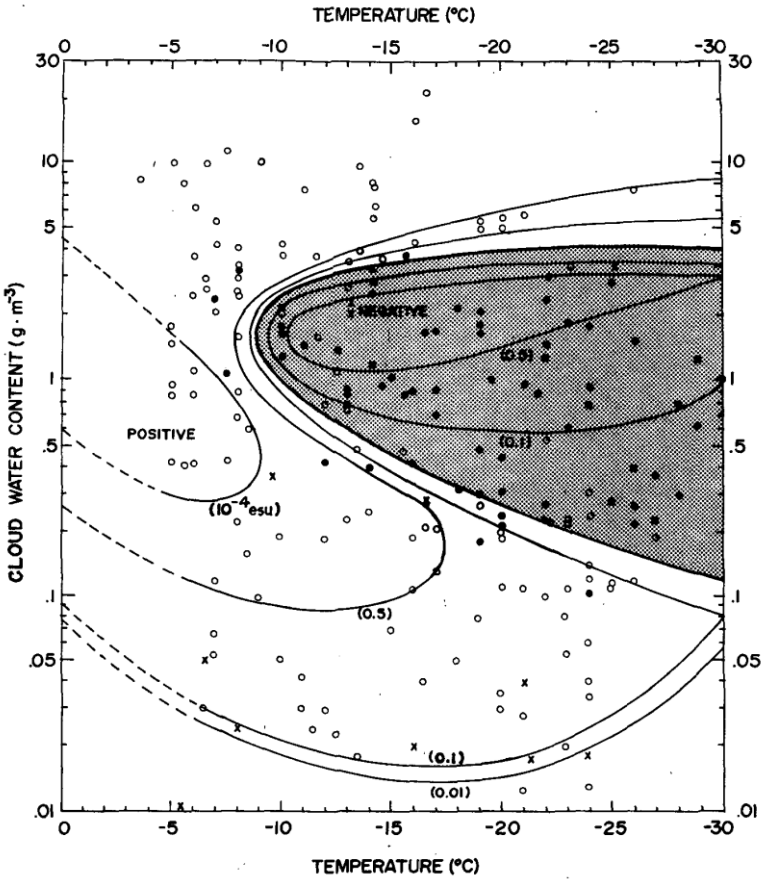

Figure 1.1 Polarity and magnitude of graupel by during collision with ice crystals in a laboratory experiment (Takahashi 1978, Fig. 8).

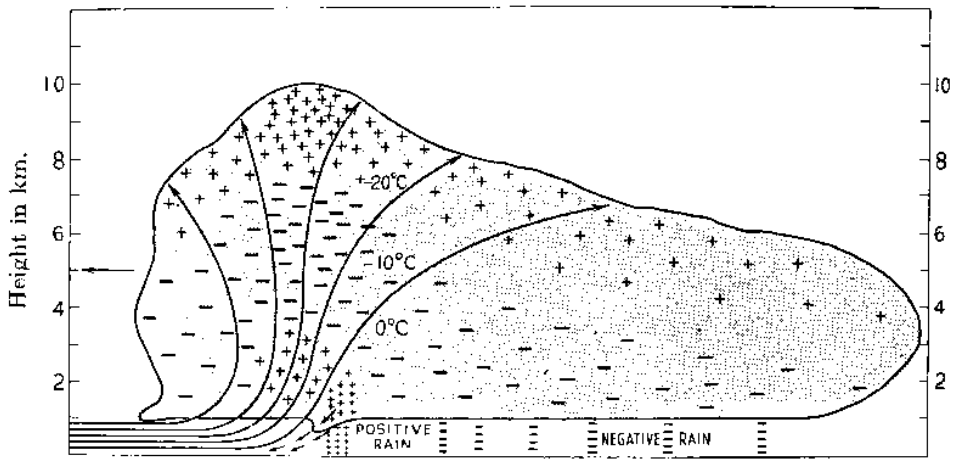

Figure 1.2 Generalized thunderstorm, distribution of electricity by balloon observations (Simpson and Scrase 1937, Fig. 22).

1.1.2 Lightning activity in Japan

Previous studies on statistical research of lightning activity in Japan, in the 1980s were based on visual lightning observations (e.g., Takeuchi 1987; Fujibe 1988; Kitagawa 1989). Since the 1990s, some lightning location systems that use lightning radiation have been installed in Japan (e.g., Lightning Database Working Group 2004; Ishii et al. 2014, Hayashi 2016). The Japan Meteorological Agency (JMA) has been deploying a lightning detection network (LIDEN) since 2000, using 30 observation sites (Fig 1.3). Ishii et al. (2014) summarized the characteristics of lightning activity in Japan using LIDEN as follows: In summer, there are many lightning flashes over the inland area, and the Kanto Plain is the region with the highest number of lightning observations in Japan (Fig. 1.4). The frequency of lightning strikes in summer shows a clear diurnal cycle, with peak lightning activity at 15–19 local times. This indicates that thunderstorms develop due to surface heating by solar radiation during the daytime. On the other hand, in winter, lightning activity is observed along the coast of the Sea of Japan and on the eastern offshore are of the Kanto region. Iwasaki (2014) also pointed out the active lightning region offshore of Kanto by World Wide Lightning Location Network (WWLLN) observations. In the coastal area on the Sea of Japan side, lightning activity is concentrated in a narrow area within 20 km of the coastline, and diurnal changes are small. It is also characteristic that a sudden lightning strike without any warning (called "*Ippatsurai*" in Japanese) is generated in the winter. (Hayashi and Marui 2016). In spring, high lightning density areas have already appeared in plains, such as the Kanto, Noubi, and Osaka Plains. In autumn, lightning activity is high in the northern part of the Sea of Japan coast. Monthly observations indicate that the lightning area notably moved south from September to November (not shown). Thus, in Japan, except in the Pacific region in winter, there is always a risk of lightning strikes.

The target area of this thesis is the Kanto Plain, which has the highest lightning activity observed in summer. This is also the most populated area in Japan, with high aviation and traffic demand. For these reasons, research on accurate lightning prediction for the Kanto Plain has important social significance.

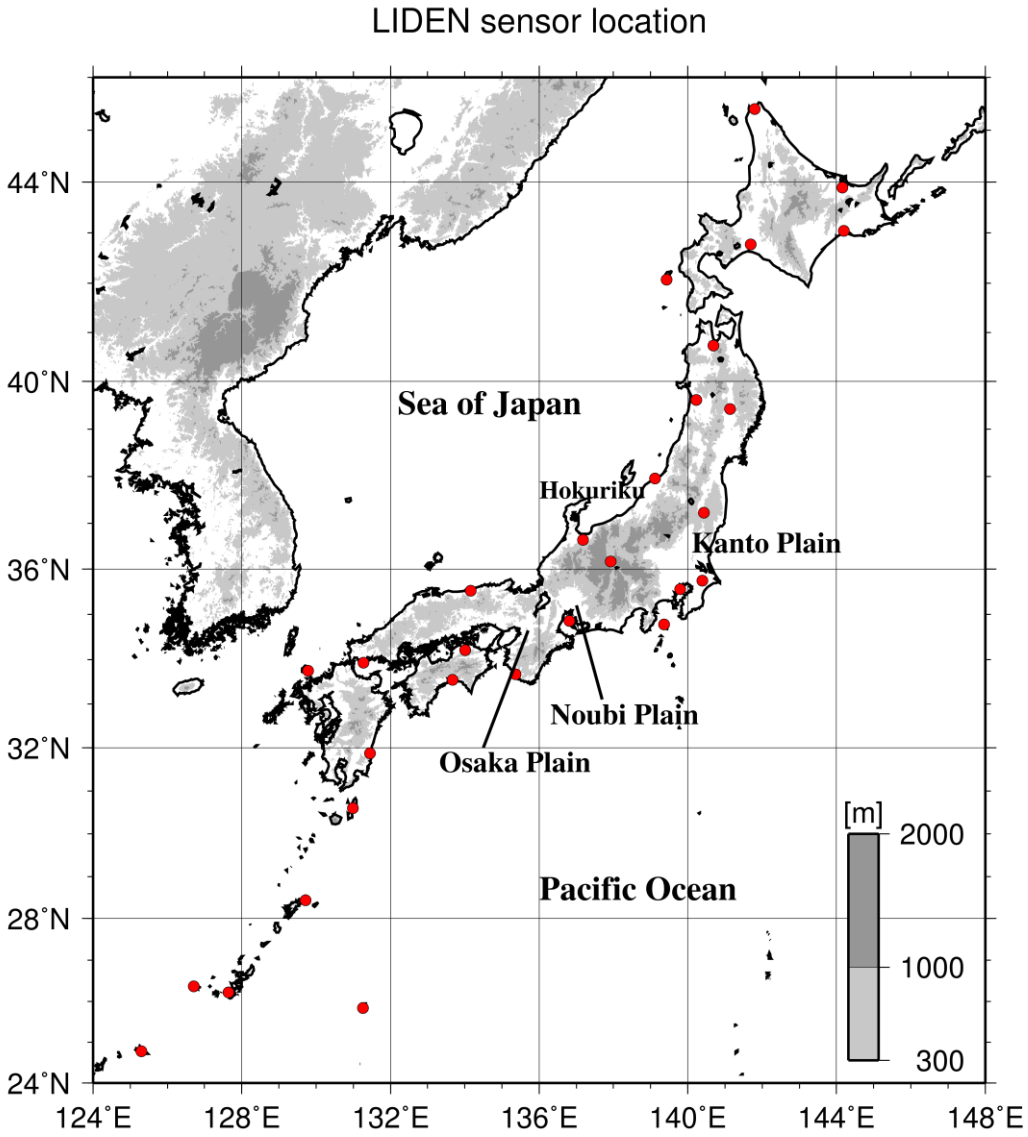

Figure 1.3 LIDEN sensor location (red dot) and topography of Japan.

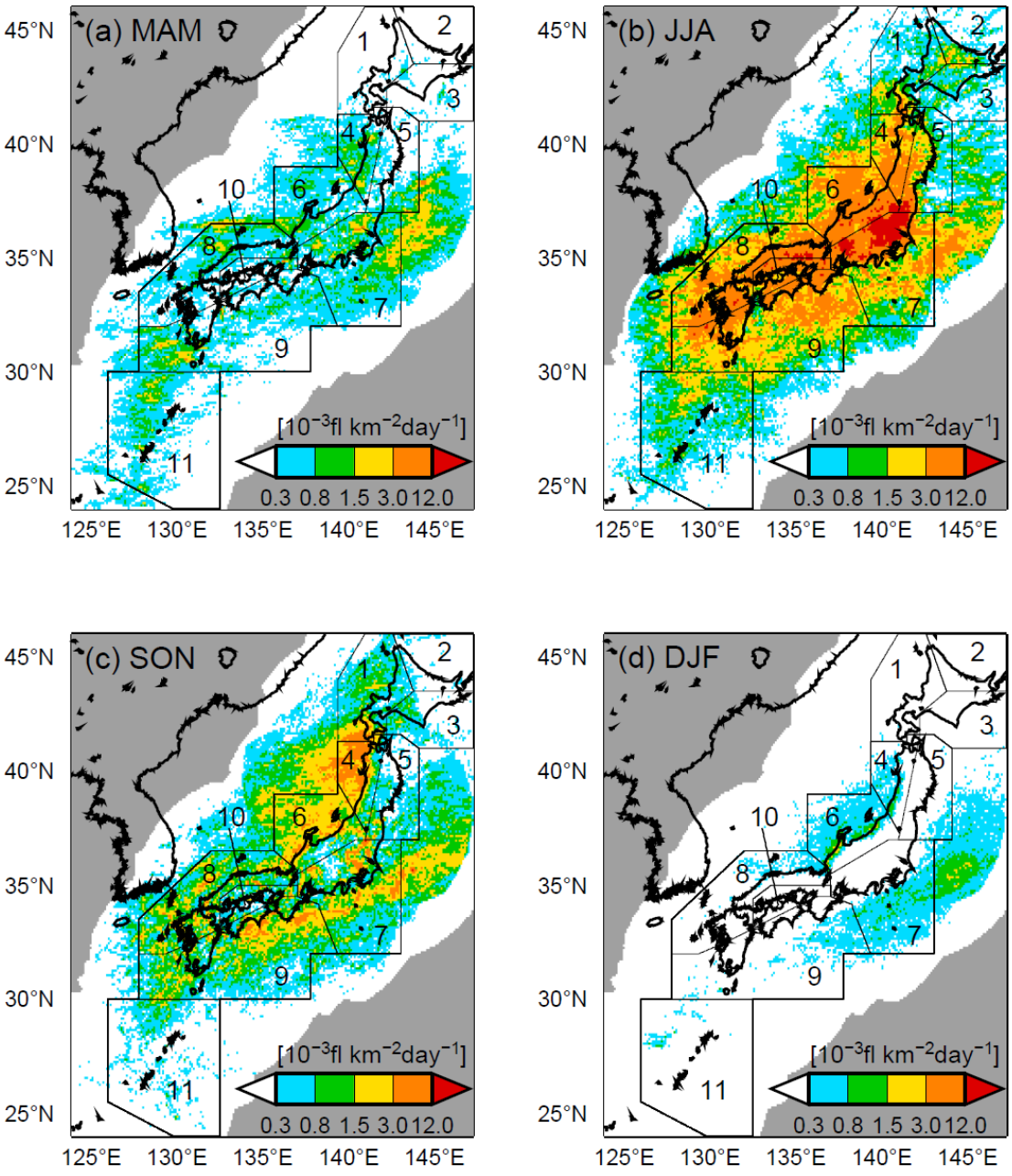

Figure 1.4 LIDEN cloud to ground lightning flash density by 0.1 degree in latitude and longitude for 7years, 2002 – 2008, (a) March-April-May, (b) June-July-August, (c) September-October-November, (d) December-January-February (Ishii et al. 2014, Fig. 2).

1.1.3 Effects of lightning strikes for aviation

Lightning is a threat to the safe operation of aviation as it affects aircraft in many ways, including direct damage during flight, ground service staff and equipment at airports due to lightning strikes, and delays in operations due to these incidents (Yoshikawa and Ushio 2019).

Uman and Rakov (2003) reported that lightning strikes occur once every 3,000-5,000 flight hours per aircraft. This is roughly equivalent to one lightning strike per year on average per aircraft, implying dozens of lightning strikes during an aircraft's designed life. However, it should be noted that the aircraft is designed to operate safely even if lightning strikes during flight; the lightning protection systems do not lead to serious incidents. Even if a lightning strike does not affect the flight, it requires time for repairs on the ground and the cost of rescheduling the flight. According to Sweers et al. (2012), lightning strikes often occur at altitudes in a specific range (1.5 to 4.5 km) around the freezing level. Owing to the limited routes and altitudes around airports during aircraft takeoffs and landings, it is difficult to avoid thunderstorms and increase the risk of lightning strikes (Yoshikawa and Ushio 2019). Moreover, an aircraft causes triggered-lightning strikes through their passage (Mazur 1989). Kobayashi (2007) succeeded in video recording a lightning strike on an aircraft flying under the cloud base around Komatsu Airport on January 6, 1987. No lightning strikes were observed before and after the lightning strike on the aircraft, and a bi-directional leader from the aircraft was observed. Therefore, a lightning strike occurred because of the passage of the aircraft itself.

There is a similar lightning strike risk when launching a rocket. On March 26, 1987, Atlas-Centaur 67, launched from Cape Canaveral Air Force Station, Florida, failed due to a lightning strike (Christian et al. 1989). The incident occurred because the lightning strike caused by the rocket passage through the charged thunderstorm destroyed the onboard computer memory. Subsequently, the National Aeronautics and Space Administration (NASA) established the Lightning Launch Committee Criteria (LLCC, Merceret et al. 2010). Currently, NASA and the Japan Aerospace Exploration Agency (JAXA) are launching rockets based on the launch restrictions proposed by the LLCC. This restriction causes rescheduling and increases the cost of launching.

Therefore, there is significant value for technology to classify charged cumulonimbi that initiate lightning and non-charged cumulonimbi that do not. As it is difficult to observe the charge status in a cloud, it is first necessary to investigate the radar reflectivity and hydrometer particle distribution in a cloud with lightning to clarify the characteristics of a charged cloud.

1.1.4 Current status of lightning forecast

Lightning prediction within one hour is called "lightning nowcast." Previous studies have used radar reflectivity to predict lightning. Gremillion and Orville (1999) used radar reflectivity to perform lightning nowcasts and stated that lightning would occur approximately 7.5 min after the appearance of 40 dBZ at −10 °C. The high radar reflectivity above the freezing level suggests the existence of graupel or hail, which is the cause of lightning based on NIC theory (see Sec 1.1.1). Many studies have also used radar data to forecast lightning using various reflectivities at various isotherm heights (e.g., Buechler and Goodman 1990; Michimoto 1991; Hondl and Eilts 1994; Gremillion and Orville 1999; Vincent et al. 2004; Wolf 2007; Clements and Orville 2008; Antonescu et al. 2013). Their results were documented by Mosier et al. (2011) (Table 1.1).

Recently, research on the lightning index using Doppler and dual-polarization radar data in addition to radar reflectivity has been conducted (e.g., Carey and Rutledge 2000; Deierling and Petersen 2008; Deierling et al. 2008; Bassarb et al. 2015; Mecikalski et al. 2015; Sakurai et al. 2015; Carey et al. 2019). The results are presented in Table 1.2. Basarab et al. (2015) indicated that the 35 dBZ volume of a thunderstorm demonstrated the best correlation for 11 cases in Colorado. Carey et al. (2019) subsequently increased the number of sample cases to 33 to perform a similar analysis in Alabama, where it was found that graupel volume had the best correlation. Although these statistical analyses adopted a similar analysis method, different lightning indices yielded the best results. Further research is needed to clarify the relationship between microphysical properties and lightning activity.

Table 1.1 Results from previous studies of lightning forecasting with radar reflectivity (Mosier et al. 2011, Table 1).

Study	No. of cells	Location	Criteria		PoD	FAR	CSI	Lead time (min)
			Reflectivity (dBZ)	Isotherm (°C)				
Buechler and Goodman (1990)	20	FL, AL, NM	40	−10	1.00	0.20	0.80	4-33
Michimoto (1991)		Japan	30	−20				5
Hondl and Eilts (1994)	23	FL	10	−10	1.00	0.18	0.82	15
Gremillion and Orville (1999)	39	FL	40	−10	0.84	0.07	0.79	7.5
Vincent et al. (2004)	50	NC	25	−15	0.84	0.24	0.67	14.8
			35	−10	1.00	0.41	0.59	17.5
			40	−15	0.86	0.31	0.63	11.0
Wolf (2007)	1,100	FL, GA	40	−10	0.96	0.11	0.86	N/A
Clements and Orville (2008)	37	TX	30	−10				16.14

Table 1.2 Recent studies of lightning index from Doppler-radar or Dual-polarization radar

Study	No. of storms	Location	Index	Correlation coefficient
Carey and Rutledge (2000)	1	Tiwi Islands	Graupel mass	0.9
Deierling and Petersen (2008)	11	Northern Alabama, Colorado/Kansas	Updraft (> 5 m s^{-1}) volume	0.93
Deierling et al. (2008)	11	(the same above)	Precipitation ice mass	0.94
Bassarb et al. (2015)	11	Colorado	35 dBZ volume	0.91
Mecikalski et al. (2015)	1	Alabama	Graupel mass	0.88
Sakurai et al. (2015)	4	Japan	Updraft (> 10 m s^{-1}) volume	0.83
Carey et al. (2019)	33	Alabama	Graupel mass	0.76

For lightning nowcasts in operational usage, the simplified method adds movement prediction after lightning occurs. This cannot be predicted unless lightning is initiated; therefore, the first lightning is overlooked in principle. In addition, it is not possible to detect areas with increased risk before lightning strikes, such as aircraft triggered-lightning. Moreover, there is no information on the development and decay of lightning activity. The JMA now operates lightning nowcast using radar reflectivity, temperature profile, and a moving vector of radar echo in addition to lightning location data (Kasahara 2011). Such developments will increase lightning prediction accuracy to improve the safety of our lives, traffic, and aviation.

On the other hand, in lightning forecasts for several hours to several days, traditional convective indicators such as atmospheric instability from numerical weather prediction (NWP) output are used in operation (JMA 2019). This is intended to predict the probability of convection and does not consider the electrical lightning process. Romps et al. (2014) expected increases in lightning frequency in future climates based on the global warming model. Their results remain uncertain because they predict changes in lightning frequency from the atmospheric instability of the model, which does not include hydrometer particles and electrification information. Research is also underway to directly reproduce the atmospheric electricity process with NWP, but it has not reached operational use because of its complicated lightning process and high computational resource cost (e.g., Takahashi 1984; MacGorman et al. 2001; Mansell et al. 2005; Hayashi 2006; Sato et al. 2019). Figure 1.5 shows the simulated space charge density in the thunderstorm from the results of Hayashi (2006). However, the reproducibility of NWP has not been sufficiently confirmed as it is difficult to obtain sufficient observation data to verify such a space charge distribution. In order to improve the accuracy of the NWP lightning process, the relationship between the hydrometer particles and lightning in the thunderstorm should be clarified.

Recently, with the development of radar remote sensing technology, it has become possible to obtain particle information in addition to reflectivity; therefore, more accurate lightning predictions can be expected.

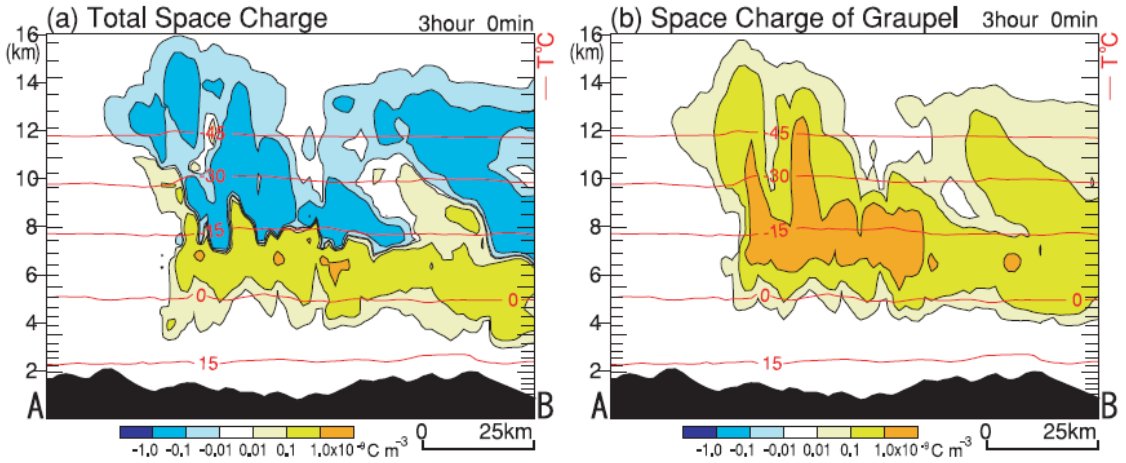

Figure 1.5 Vertical cross section of (a) simulated total space charge density and (b) simulated space charge density by graupel with colored shade, and temperature with red contour (Hayashi 2006, Fig. 3).

1.2 Objectives of this thesis

The objective of this thesis is to develop lightning indices using real-time remote sensing data. Although direct observations, such as radiosonde, can obtain detailed particle distribution and electric field intensity in a thunderstorm, it is difficult to use them for operational lightning prediction because of their low observation frequency. The final objective of this research is to propose a new lightning index that is effective in various thunderstorms using real-time radar remote sensing data. For this purpose, dual-polarization radar, which can observe the particle information in a thunderstorm, is used to create a more effective lightning index, in addition to the use of the conventional single-polarization radar.

1.3 Thesis organization

This thesis is organized as follows.

Chapter 1 briefly describes the background and objectives of this thesis. Lightning mechanisms are introduced based on previous studies, and the lightning activity in Japan and the

impact of lightning strikes on aircraft operations are described. The current status and issues of lightning prediction are documented, and the purpose of this thesis is described.

Chapter 2 describes two types of radar observation systems, single-polarized and double-polarized radar. The hydrometer classification algorithm using the dual-polarization radar data used in this thesis is also described.

In Chapter3, using the conventional radar for operational purposes in the Kanto Plain, central Japan, the life of lightning and non-lightning cells on a summer day in 2010 are tracked, and the radar observation characteristics of each cell are statistically summarized. The relationship between thunderstorm development and lightning activity is reported. The prediction accuracy of the radar-derived parameters for lightning was evaluated by comparing it with the lightning indicators of previous studies.

Chapter 4 investigates the relationship between the spatial distribution of precipitation particles and lightning for the 2017 and 2018 summers in the Kanto Plain. The newly developed hydrometeor classification algorithm was applied to observations from the dual-polarization radar to acquire the spatial distribution of precipitation particles in the thunderstorm. Using the observation of isolated thunderstorms, the relationships between radar-derived parameters and lightning activity are compared. From these results, the index that best represents lightning is shown.

Chapter 5 summarizes the results obtained by this thesis and describes future work.

References of Chapter 1

Antonescu, B., S. Burcea, and A. Tănase, 2013: Forecasting the onset of cloud-to-ground lightning using radar and upper-air data in Romania. *International Journal of Climatology*, **33**, 1579-1584, https://doi.org/10.1002/joc.3533

Basarab, B. M., S. A. Rutledge, and B. R. Fuchs, 2015: An improved lightning flash rate parameterization developed from Colorado DC3 thunderstorm data for use in cloud-resolving chemical transport models. *Journal of Geophysical Research: Atmospheres*, **120**, 9481-9499, https://doi.org/10.1002/2015JD023470

Buechler, D. E., and S. J. Goodman, 1990: Echo size and asymmetry: Impact on NEXRAD storm identification. *Journal of Applied Meteorology*, **29**, 962-969, https://doi.org/10.1175/1520-0450(1990)029%3C0962:ESAAIO%3E2.0.CO;2

Carey, L. D., and S. A. Rutledge, 2000: The relationship between precipitation and lightning in tropical island convection: a c-band polarimetric radar study. *Monthly Weather Review*, **128**, 2687-2710, https://doi.org/10.1175/1520-0493(2000)128%3C2687:TRBPAL%3E2.0.CO;2

Carey, L. D., E. V. Schultz, C. J. Schultz, W. Deierling, W. A. Petersen, A. L. Bain, and K. E. Pickering, 2019: An evaluation of relationships between radar-inferred kinematic and microphysical parameters and lightning flash rates in Alabama storms. *Atmosphere*, **10**, 796, https://doi.org/10.3390/atmos10120796

Christian, H. J., V. Mazur, B. D. Fisher, L. H. Ruhnke, K. Crouch, and R. P. Perala, 1989: The Atlas/Centaur lightning strike incident. *Journal of Geophysical Research: Atmospheres*, **94**, 13169-13177, https://doi.org/10.1029/JD094iD11p13169

Clements, N. C., and R. E. Orville, 2008: The warning time for cloud-to-ground lightning in isolated, ordinary thunderstorms over Houston, Texas. *Third Conf. on Meteorological Applications of Lightning Data*, New Orleans, LA, American Meteorological Society, 6.4, http://ams.confex.com/ams/pdfpapers/132309.pdf

Curran, E. B., R. L. Holle, and R. E. López, 2000: Lightning casualties and damages in the United States from 1959 to 1994. *Journal of Climate,* **13**, 3448-3464, https://doi.org/10.1175/1520-0442(2000)013%3C3448:LCADIT%3E2.0.CO;2

Deierling, W., and W. A. Petersen, 2008: Total lightning activity as an indicator of updraft characteristics. *Journal of Geophysical Research: Atmospheres*, **113**, D16210, https://doi.org/10.1029/2007JD009598

Deierling, W., W. A. Petersen, J. Latham, S. Ellis, and H. J. Christian, 2008: The relationship between lightning activity and ice fluxes in thunderstorms. *Journal of Geophysical Research: Atmospheres*, **113**, D15210, https://doi.org/10.1029/2007JD009700

Fujibe, F., 1988: Diurnal variations of precipitation and thunderstorm frequency in Japan in the warm season. *Papers in Meteorology and Geophysics*, **39**, 79-94, https://doi.org/10.2467/mripapers.39.79

Gremillion, M. S., and R. E. Orville, 1999: Thunderstorm characteristics of cloud-to-ground lightning at the Kennedy Space Center, Florida: A study of lightning initiation signatures as indicated by the WSR-88D. *Weather and Forecasting*, **14**, 640-649, https://doi.org/10.1175/1520-0434(1999)014%3C0640:TCOCTG%3E2.0.CO;2

Gunn, R. 1948: Electric field intensity inside of natural clouds. *Journal of Applied Physics*, **19**, 481-484, https://doi.org/10.1063/1.1698159

Hayashi, S. 2006: Numerical simulation of electrical space charge density and lightning by using a 3-dimensional cloud-resolving model. *SOLA*, **2**, 124-127, https://doi.org/10.2151/sola.2006-032

Hayashi, S., 2016: Statistical relationships of precipitation rate and wind gust intensity to lightning activity in Japan. *Journal of Atmospheric Electricity*, **35**, 43-51, https://doi.org/10.1541/jae.35.43

Hayashi S., and C. Marui, 2016: Frequency and seasonal variation of single lightning flash storm, "Ippatsurai", in Japan (in Japanese). *Journal of Atmospheric Electricity,* **36**, 13-22, https://doi.org/10.1541/jae.36.13

Hondl, K. D., and M. D. Eilts, 1994: Doppler radar signatures of developing thunderstorms and their potential to indicate the onset of cloud-to-ground lightning. *Monthly Weather Review*, **122**, 1818-1836, https://doi.org/10.1175/1520-0493(1994)122%3C1818:DRSODT%3E2.0.CO;2

Ishii, K., S. Hayashi, and F. Fujibe, 2014: Statistical analysis of temporal and spatial distributions of cloud-to-ground lightning in Japan from 2002 to 2008. *Journal of Atmospheric Electricity*, **34**, 79-86, https://doi.org/10.1541/jae.34.79

Iwasaki, H., 2014: Preliminary study on features of lightning discharge around Japan using World Wide Lightning Location Network data. *SOLA*, **10**, 98-102, https://doi.org/10.2151/sola.2014-020

Japan Meteorological Agency, 2019: Outline of the operational numerical weather prediction at the Japan Meteorological Agency. Accessed 01 November 2020, https://www.jma.go.jp/jma/jma-eng/jma-center/nwp/outline2019-nwp/index.htm

Jayaratne, E. R., C. P. R. Saunders, and J. Hallett, 1983: Laboratory studies of the charging of soft-hail during ice crystal interactions. *Quarterly Journal of the Royal Meteorological Society*, **109**, 609-630, https://doi.org/10.1002/qj.49710946111

Kasahara, S., 2011: Launch of lightning nowcast in JMA. *Tenki*, **57**, 847-852 (in Japanese).

Kitagawa, N., 1989: Long-term variations in thunder-day frequencies in Japan. *Journal of Geophysical Research: Atmospheres*, **94**, 13183-13189, https://doi.org/10.1029/JD094iD11p13183

Kobayashi, F., T. Shimura, and K. Masuda, 2007: Aircraft triggered lightning caused by winter thunderclouds in the Hokuriku coast, Japan-A case study of a lightning strike to aircraft below the cloud base. *SOLA*, **3**, 109-112, https://doi.org/10.2151/sola.2007-028

Lightning Database Working Group, 2004: Lightning occurrence data observed with lightning location systems of electric utilities in Japan: 1992-2001. *IEEJ Transactions on Power and Energy*, **124**, 1255-1262, https://doi.org/10.1541/ieejpes.124.1255

MacGorman D. R., and W. D. Rust, 1998. *The Electrical Nature of the Storms.* Oxford University Press, 422pp.

MacGorman, D. R., W. D. Rust, P. Krehbiel, W. Rison, E. Bruning, and K. Wiens, 2005: The electrical structure of two supercell storms during STEPS. *Monthly Weather Review*, **133**, 2583-2607, https://doi.org/10.1175/MWR2994.1

MacGorman, D. R., J. M. Straka, and C. L. Ziegler, 2001: A lightning parameterization for numerical cloud models. *Journal of Applied Meteorology*, **40**, 459-478, https://doi.org/10.1175/1520-0450(2001)040<0459:ALPFNC>2.0.CO;2

Mansell, E. R., D. R. MacGorman, C. L. Ziegler, and J. M. Straka, 2005: Charge structure and lightning sensitivity in a simulated multicell thunderstorm. *Journal of Geophysical Research: Atmospheres*, **110**, D12101, https://doi.org/10.1029/2004JD005287

Marshall, T. C., and W. D. Rust, 1991: Electric field soundings through thunderstorms. *Journal of Geophysical Research: Atmospheres*, **96**, 22297-22306, https://doi.org/10.1029/91JD02486

Mazur, V., 1989: A physical model of lightning initiation on aircraft in thunderstorms. *Journal of Geophysical Research: Atmospheres*, **94**, 3326-3340, https://doi.org/10.1029/JD094iD03p03326

Mecikalski, R. M., A. L. Bain, and L. D. Carey, 2015: Radar and lightning observations of deep moist convection across northern Alabama during DC3: 21 May 2012. *Monthly Weather Review*, **143**, 2774-2794, https://doi.org/10.1175/MWR-D-14-00250.1

Merceret, F., J. Willett, H. Christian, J. Dye, E. Krider, J. Madura, T. O'Brien, W. Rust, and R. Waltersheid, 2010: A history of the lightning launch commit criteria and the lightning

advisory panel for America's space program. *NASA Technical. Report*, NASA/SP-2010-216283.

Michimoto, K., 1991: A study of radar echoes and their relation to lightning discharge of thunderclouds in the Hokuriku district. Part I: Observations and analysis of thunderclouds in summer and winter. *Journal of the Meteorological Society of Japan*, **69**, 327–335, https://doi.org/10.2151/jmsj1965.69.3_327

Mosier, R. M., C. Schumacher, R. E. Orville, and L. D. Carey, 2011: Radar nowcasting of cloud-to-ground lightning over Houston, Texas. *Weather and Forecasting*, **26**, 199–212, https://doi.org/10.1175/2010WAF2222431.1

National Police Agency, 2010: The white paper on police 2020. Accessed 01 February 2021, https://www.npa.go.jp/hakusyo/h22/index.html

National Weather Service, 2020: 2019 Weather related fatality and injury statistics. Accessed 01 November 2020, https://www.weather.gov/hazstat/

Reynolds, S. E., M. Brook, and M. F. Gourley, 1957: Thunderstorm charge separation. *Journal of Meteorology*, **14**, 426–436, https://doi.org/10.1175/1520-0469(1957)014%3C0426:TCS%3E2.0.CO;2

Romps, D. M., J. T. Seeley, D. Vollaro, and J. Molinari, 2014: Projected increase in lightning strikes in the United States due to global warming. *Science*, **346**, 851-854, https://doi.org/10.1126/science.1259100

Rust, W. D., and D. R. MacGorman, 2002: Possibly inverted-polarity electrical structures in thunderstorms during STEPS. *Geophysical Research Letters*, **29**, 12-1, https://doi.org/10.1029/2001GL014303

Sakurai, N., S. Shimizu, Y. Shusse, S. Suzuki, T. Maesaka, K. Kieda, and K. Iwanami, 2015: Relationships between updraft characteristics and cloud-to-ground lightning activity in warm-season convective storms in the Kanto region, Japan. *SOLA*, **11**, 177-180, https://doi.org/10.2151/sola.2015-039

Sato, Y., Y. Miyamoto, and H. Tomita, 2019: Large dependency of charge distribution in a tropical cyclone inner core upon aerosol number concentration. *Progress in Earth and Planetary Science*, **6**, 1-13, https://doi.org/10.1186/s40645-019-0309-7

Simpson, G., and F. G. Scrase, 1937: The distribution of electricity in thunderclouds, *Proc. R. Soc. London, Ser. A*, **161**, 309–352, https://doi.org/10.1098/rspa.1937.0148

Stolzenburg, M., W. D. Rust, B. F. Smull, and T. C. Marshall, 1998: Electrical structure in thunderstorm convective regions: 1. Mesoscale convective systems. *Journal of Geophysical Research: Atmospheres*, **103**, 14059-14078, https://doi.org/10.1029/97JD03546

Sweers, G., B. Birch, and J. Gokcen, 2012: Lightning strikes: protection, inspection, and repair. *Aero Magazine*, **4**, 19-28.

Takahashi, T., 1978: Riming electrification as a charge generation mechanism in thunderstorms. *Journal of the Atmospheric Sciences*, **35**, 1536–1548, https://doi.org/10.1175/1520-0469(1978)035<1536:REAACG>2.0.CO;2

Takahashi, T., 1984: Thunderstorm electrification—a numerical study. *Journal of the Atmospheric Sciences*, **41**, 2541–2558, https://doi.org/10.1175/1520-0469(1984)041<2541:TENS>2.0.CO;2

Takeuchi, T., 1987: *Lightning Discharge*, Nagoya University Press, 191pp. (in Japanese)

Uman, M. A., and V. A. Rakov, 2003: The interaction of lightning with airborne vehicles. *Progress in Aerospace Sciences*, **39**, 61-81, https://doi.org/10.1016/S0376-0421(02)00051-9

Vincent, B. R., L. D. Carey, D. Schneider, K. Keeter, and R. Gonski, 2004: Using WSR-88D reflectivity for the prediction of cloud-to-ground lightning: A central North Carolina study. *National Weather. Digest*, **27**, 35–44.

Williams, E. R., 1989: The tripole structure of thunderstorms, *Journal of Geophysical Research: Atmospheres*, **94**, 13151– 13167, https://doi.org/10.1029/JD094iD11p13151

Wolf, P., 2007: Anticipating the initiation, cessation, and frequency of cloud-to-ground lightning, utilizing WSR-88D reflectivity data. http://nwafiles.nwas.org/ej/pdf/2007-EJ1.pdf

Yoshikawa, E., and T. Ushio, 2019: Tactical decision-making support information for aircraft lightning avoidance: feasibility study in area of winter lightning. *Bulletin of the American Meteorological Society*, **100**, 1443–1452, https://doi.org/10.1175/BAMS-D-18-0078.1

Chapter 2
Observation systems

2.1 Weather radar equation

Radar (RAdio Detection And Ranging) is an observation device that uses radio waves to determine the location and other information of objects. In weather radar, the radio waves transmitted from the antenna are reflected and scattered by precipitation particles in clouds. The properties of the precipitation particles are obtained from the radio waves received by the antenna. The precipitation particles' location is determined by the elapsed time from the radar pulse initiation to the return signal detection. The weather radar equation required to obtain the radar reflectivity factor, which is the most important parameter in radar meteorology (e.g., Fukao and Hamadu 2005; Rauber and Nesbitt 2018), is derived as follows.

The radiated power P_i [W m^{-2}] incident on a target, at range r [m], for antenna gain G, with peak power P_t [W], can be calculated as

$$P_i = \frac{P_t}{4\pi r^2} \cdot G \tag{2.1}$$

The power P_s [W] scattered from the target, is expressed as follows using the backscattering cross section σ [m^2] and P_i. By substituting (2.1), the following equation is obtained:

$$P_s = \frac{\sigma P_i}{4\pi} = \frac{\sigma}{4\pi} \cdot \frac{P_t}{4\pi r^2} \cdot G \tag{2.2}$$

The total received power P_r [W] is obtained by multiplying (2.2) by the effective antenna area A_e [m^2] as

$$P_r = P_s \cdot \frac{A_e}{r^2} = \frac{\sigma}{4\pi} \cdot \frac{P_t}{4\pi r^2} \cdot G \cdot \frac{A_e}{r^2} \tag{2.3}$$

From the antenna theory, the relationship between the antenna gain and the effective area is

expressed by

$$A_{\mathrm{e}} = \frac{\lambda^2 \cdot G}{4\pi} \tag{2.4}$$

where λ [m] is the radar wavelength. Substituting (2.4) into (2.3), the radar equation for a solid target is obtained.

$$P_{\mathrm{r}} = \frac{P_{\mathrm{t}} \cdot G^2 \cdot \lambda^2}{(4\pi)^3 \cdot r^4} \cdot \sigma \tag{2.5}$$

The Rayleigh approximation can be applied when the spherical particle size is relatively smaller than the wavelength. The backscattering cross-section σ when spherical particles are homogeneously filled in a unit volume is expressed as

$$\sum \sigma = \frac{\pi^5}{\lambda^4} \cdot \left|\frac{\varepsilon - 1}{\varepsilon + 2}\right|^2 \sum D^6 \tag{2.6}$$

where D [m] is the diameter of the target particle and ε_{r} [unitless] is the relative dielectric constant of the sphere. Assuming a parabolic antenna, the horizontal and vertical beam widths are equal to θ_{l} [deg], and the pulse length is h [m]. The scattered volume V [m^3] is calculated as

$$V = \frac{\pi \cdot r^2 \cdot h}{2^4} \cdot \frac{{\theta_1}^2}{\log_{\mathrm{e}} 2} \tag{2.7}$$

From (2.5), (2.6) and (2.7), the power $\overline{P}_{\mathrm{r}}$ [W] received from the target volume that is homogeneously filled with spherical particles is expressed as

$$\overline{P}_{\mathrm{r}} = \frac{P_{\mathrm{t}} \cdot G^2 \cdot {\theta_1}^2 \cdot h}{2^{10} \cdot r^2 \cdot \log_{\mathrm{e}} 2} \cdot \frac{\pi^3}{\lambda^2} \cdot \left|\frac{\varepsilon_{\mathrm{r}} - 1}{\varepsilon_{\mathrm{r}} + 2}\right|^2 \sum D^6 \tag{2.8}$$

The weather radar equation is obtained by summarizing the radar-dependent coefficients into the radar constant R_{c} [W m^{-1}] as follows:

$$\overline{P}_{\mathrm{r}} = \frac{R_{\mathrm{c}} \cdot Z}{r^2} \tag{2.9}$$

$$R_{\mathrm{c}} = \frac{P_{\mathrm{t}} \cdot G^2 \cdot {\theta_1}^2 \cdot h \cdot \pi^3}{2^{10} \cdot r^2 \cdot \log_{\mathrm{e}} 2} \cdot \left| \frac{\varepsilon_{\mathrm{r}} - 1}{\varepsilon_{\mathrm{r}} + 2} \right|^2 \tag{2.10}$$

$$Z = \sum D^6 \tag{2.11}$$

The radar reflectivity factor Z [m^6 m^{-3}], the sum of the sixth power of the diameters of all raindrops within the scattered volume, is the most important quantity in weather radar (Rauber and Nesbitt 2018). Assuming an exponential function of the number of drop size distributions is N(D) [m^{-3} m^{-1}], the radar reflectivity factor Z is represented by

$$Z = \sum D^6 = \int_{D_{\min}}^{D_{\max}} D^6 \, N(D) dD \tag{2.12}$$

The radar reflectivity factor is conventionally expressed in units of mm^6 m^{-3} and logarithmic units as

$$\mathrm{dBZ} \equiv 10 \log_{10} \left(\frac{Z}{1 \ \mathrm{mm^6 \ m^{-3}}} \right) \tag{2.13}$$

Furthermore, in actual radar observations, $\overline{P}_{\mathrm{r}}$ is corrected for attenuation due to the atmosphere, mechanical loss, and precipitation particles.

2.2 Dual-polarization radar

The dual-polarization weather radar obtains information on the size, shape, and type of hydrometeors by receiving a signal at horizontal and vertical polarizations. Dual-polarization radar is also called a multi-parameter radar. When perfectly spherical particles are observed, the radar reflectivity of each horizontal and vertical polarization is the same. When observing oblate particles (oblate is defined as an object with an axis larger in the horizontal direction compared with the vertical direction), the radar reflectivity at the horizontal and vertical polarization is different. Particle information is also obtained by the differential phase between horizontal and

vertical polarization depending on the shape and size distribution of particles in the scattered volume.

The variables in the dual-polarization retrievals are as previously introduced. The backscattering matrix $\boldsymbol{S}$ is defined as

$$\boldsymbol{S} = \begin{bmatrix} S_{\mathrm{hh}} & S_{\mathrm{hv}} \\ S_{\mathrm{vh}} & S_{\mathrm{vv}} \end{bmatrix} \tag{2.14}$$

where $\boldsymbol{S}$ depends on the size, shape, composition, and orientation of the particle.

The differential reflectivity (Z_{DR}) [dB] is defined by the radar reflectivity factor (Sec. 2.1) in the horizontal polarization (Z_{hh}) and vertical polarization (Z_{vv}).

$$Z_{\mathrm{DR}} = 10\log_{10}\left(\frac{|S_{\mathrm{hh}}|^2}{|S_{\mathrm{vv}}|^2}\right) = 10\log_{10}\left(\frac{Z_{\mathrm{hh}}}{Z_{\mathrm{vv}}}\right) \tag{2.15}$$

If the radar reflectivity factors are equivalent at each polarization, Z_{DR} is 0, whereas if $Z_{\mathrm{hh}} > Z_{\mathrm{vv}}$, then $Z_{\mathrm{DR}} > 0$, and if $Z_{\mathrm{vv}} > Z_{\mathrm{hh}}$, then $Z_{\mathrm{DR}} < 0$. Note that Z_{DR} is simply related to the ratio of the backscattering cross-sections at each polarization.

The differential phase between the copolar received signals Ψ_{DP} [deg], where the backscatter differential phase δ [deg] and the propagation differential phase ϕ_{DP} [deg], is defined as

$$\Psi_{\mathrm{DP}} = \phi_{\mathrm{DP}} + \delta \tag{2.16}$$

The specific differential phase shift K_{DP} [deg km^{-1}], which represents ϕ_{DP} between the two orthogonal polarization after separating δ from Ψ_{DP} (e.g., Hubbert et al. 1993), is

$$\phi_{\mathrm{DP}} = \phi_{\mathrm{hh}} - \phi_{\mathrm{vv}} \tag{2.17}$$

$$K_{\mathrm{DP}} = \frac{1}{2}\cdot\frac{d(\phi_{\mathrm{DP}})}{dr} \tag{2.18}$$

where ϕ_{hh} and ϕ_{vv} represent the phases in the horizontal and vertical directions, respectively. K_{DP}

is positive for oblate drops and enables the retrieval of the drop size distribution characteristics.

Co-polar correlation coefficient ρ_{hv} [unitless] is defined as

$$\rho_{hv} = \frac{|\langle S_{vv} S_{hh}^{*} \rangle|}{\sqrt{|S_{hh}|^2 |S_{vv}|^2}} \tag{2.19}$$

where the asterisk denotes the complex conjugate operator and the angle brackets denote the average over all pulses. When the size and shape of the particles in the radar resolution volume are mixed, ρ_{hv} is low; when they are uniform, ρ_{hv} is close to 1.

2.3 Hydrometeor classification algorithm (HCA)

Fuzzy logic-based methods (e.g., Liu and Chandrasekar 2000) have been developed and widely used as a hydrometeor classification algorithm (HCA). In recent years, a number of HCAs that have adopted the Bayesian classifier and/or clustering techniques have been proposed (Marzano et al. 2008; Wen et al. 2015; Wen et al. 2016; Yang et al. 2019). The HCA developed by Umehara et al. (2019) also works with a Bayesian classifier and clustering techniques. A primary feature of their method is that the radar performance can be maximized by introducing an objective clustering method.

First, the probability density function (PDF) and prior probability distribution (PPD) are prepared. The PDF is created from seven-dimensional dual-polarization radar data in various precipitation events by applying the GMM and K clustering methods. Seventeen categorized PDFs is obtained in the seven-dimensional dual-polarization radar parameters in the previous section: reflectivity at horizontal polarization (Z_{hh}), differential reflectivity (Z_{DR}), copolar correlation coefficient (ρ_{hv}), specific differential phase (K_{DP}), S(Ψ_{DP}), S(Z_{DR}) and S(ρ_{hv}), where the function S(X) represents the median absolute deviation of X (Fig. 2.1). PPD is expressed as the existence probability of precipitation particles with a temperature membership function used in the fuzzy method of CSU Radar Tools Software (Lang 2015) concerning the existence probability of the temperature (Fig. 2.2). The altitude of 0 ˚C is determined by detection of the melting layer by radar observation itself, radiosonde observation, or NWP model analysis. The

temperature is converted to altitude under the assumption of the standard atmosphere (COESA 1976) and the functions are slightly modified from Lang (2015). According to Bayes' theorem, the probability of a hydrometeor for seventeen categories is proportional to the product of PPD and the likelihood function from PDF, derived from the seven dual-polarization parameters. The hydrometeor type is determined from the highest probability score from the Bayesian technique for each radar bin. Among the seventeen types of particles from HCA, ice-related categories such as hail, graupel, snow, and cloud ice are noted in this study as they are important for cloud electrification and lightning initiation, as mentioned in Chapter 1.

2.4 Lightning observation system

As mentioned in Section 1.1, lightning occurs when the electric field in a thunderstorm increases and the electrical discharge in the atmosphere is initiated. The generated electric current radiates electromagnetic waves and explosively heats the atmosphere to generate light and shock waves. Lightning can be observed by receiving this electromagnetic wave with an antenna, detecting light emission with a camera, or detecting the sound of a shock wave with a microphone. Acoustic observations were conducted by Teer and Few (1974), but because of their difficulty, these are rarely performed now. However, the time difference between lightning and thunder roars can be calculated using the speed of sound. In optical observation, the detection range and observation frequency have made dramatic progress by mounting a lightning sensor on satellites (Christian et al. 2003). A recently launched geostationary meteorological satellite was equipped with a geostationary lightning mapper (GLM, Goodman et al. 2013), which can observe the position and time of lightning over hemispheres in real-time. For ground-based observations, electromagnetic wave observations are widely used for research and operational purposes.

The location decision method for lightning detection using an antenna was explained; although there are several methods, the time of arrival method (TOA) is described as it is also used in LIDEN. When two antennas receive lightning radiation, the location of the radiation source can be obtained on a hyperbola from the time difference between the two antennas (Fig. 2.3). Two-dimensional location and time can be obtained using three or more antennas.

Usually, four or more antennas are used to reduce location errors. In LIDEN, as antennas are installed at intervals of approximately 200 km, the accuracy is several kilometers. On the other hand, the lightning mapping array (LMA, Rison et al. 1999) with an antenna spacing of 5–10 km is capable of three-dimensional lightning location with an accuracy of 100 m. In contrast, in WWLLN, the antenna spacing is several thousand kilometers; although the position accuracy and detection rate decrease, the entire globe can be observed.

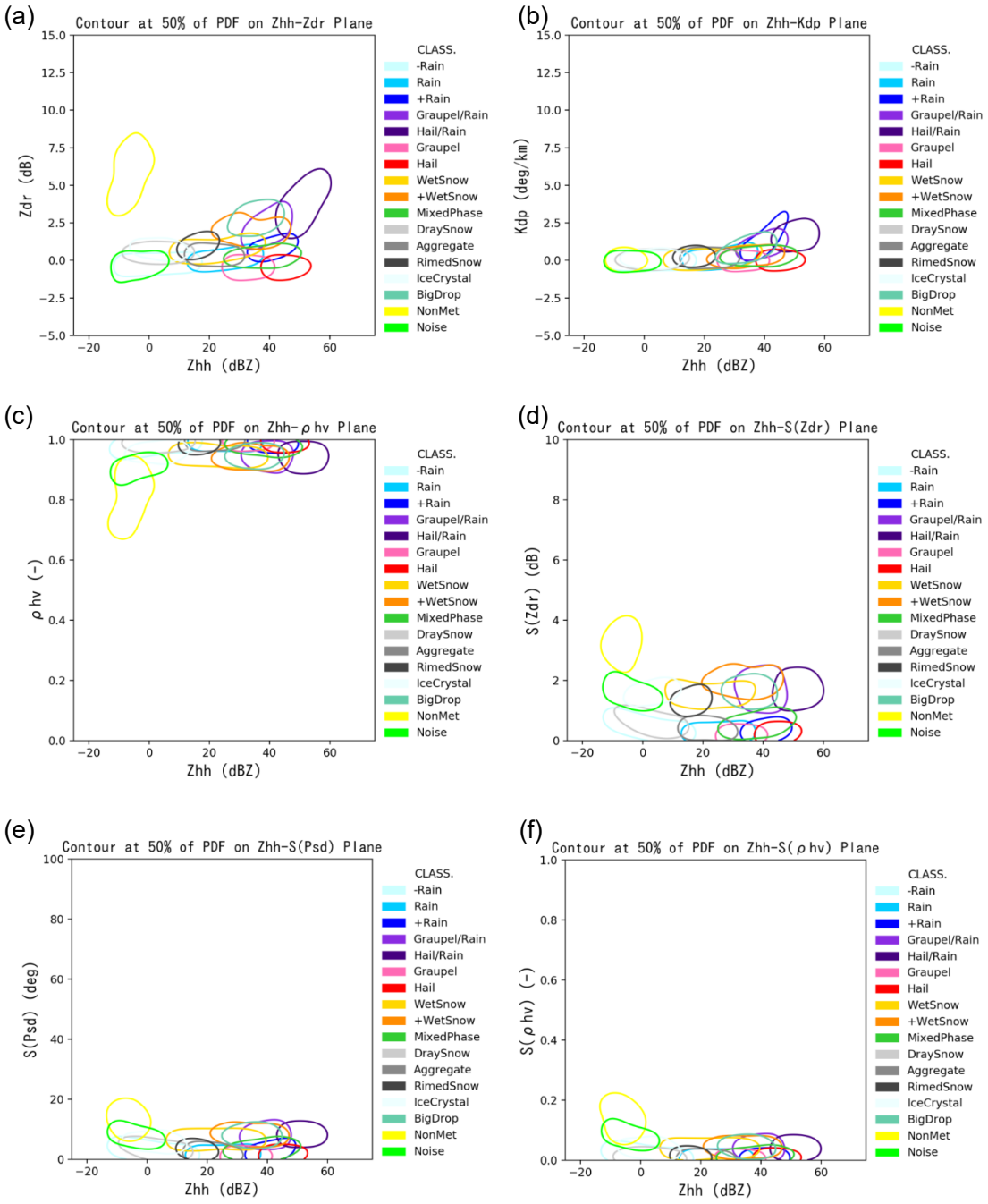

Figure 2.1 Probability density distributions derived from the clustering approach: (a) - (f) shows 17 type's PDF in Z_{hh} vs Z_{DR}, K_{DP}, ρ_{hv}, S(Z_{DR}), S(ψ_{DP}) and S(ρ_{hv}) space, respectively.

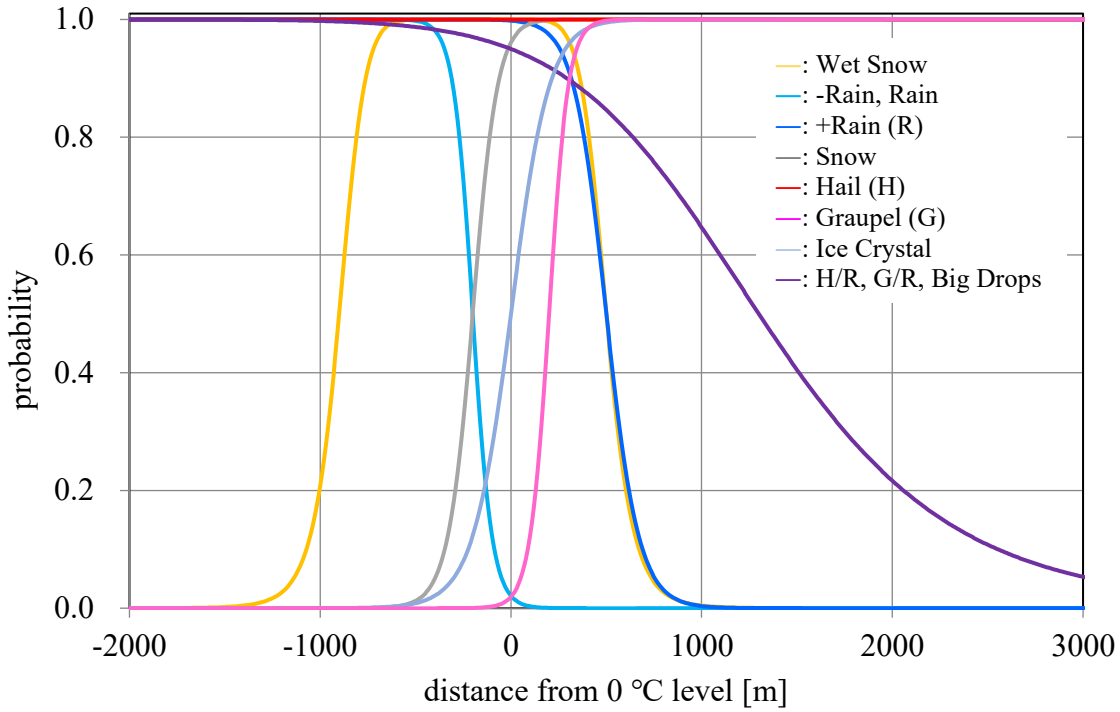

Figure 2.2 Prior probabilities expressed as the existence probability of precipitation particles with respect to the relative height from 0 ℃ altitude.

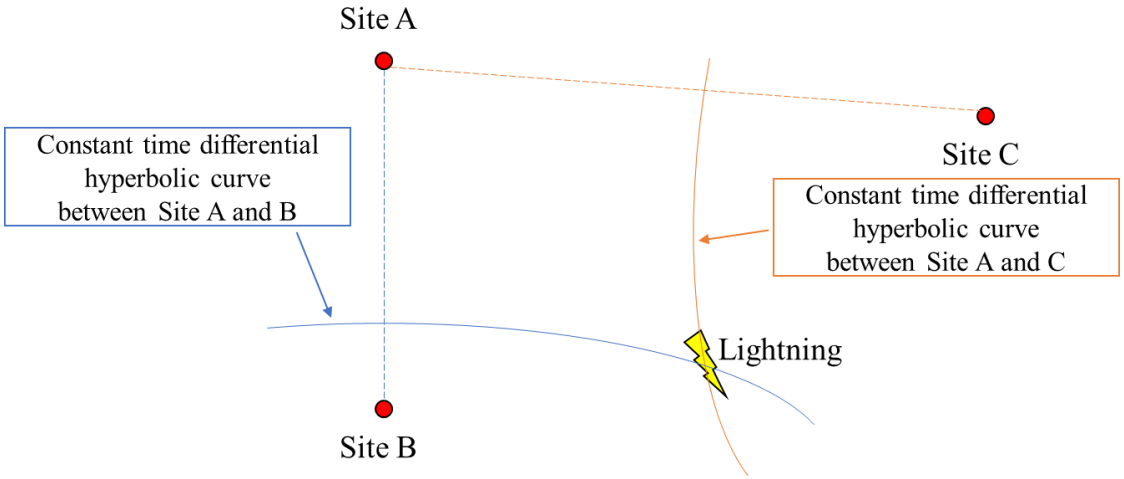

Figure 2.3 Schematic diagram of the time of arrival (TOA) method for a two-dimensional lightning position in a lightning location system.

References of Chapter 2

Christian, H. J., et al., 2003: Global frequency and distribution of lightning as observed from space by the Optical Transient Detector, *Journal of Geophysical Research*, **108**, 4005, https://doi.org/10.1029/2002JD002347

COESA, 1976: *U.S. Standard Atmosphere, 1976*. U.S. Government Printing Office, 243pp.

Few, A. A., and T. L. Teer, 1974: The accuracy of acoustic reconstructions of lightning channels, *Journal of Geophysical Research*, **79**, 5007– 5011, https://doi.org/10.1029/JC079i033p05007

Fukao, S, and K. Hamadu, 2005: *Radar Remote Sensing of Meteorology and Atmosphere (in Japanese)*. Kyoto University Press, 491pp.

Goodman, S. J., and Coauthors, 2013: The GOES-R geostationary lightning mapper (GLM). *Atmospheric Research,* **125**, 34-49, https://doi.org/10.1016/j.atmosres.2013.01.006

Hubbert, J., V. Chandrasekar, V. N. Bringi, and P. Meischner, 1993: Processing and interpretation of coherent dual-polarized radar measurements. *Journal of Atmospheric and Oceanic Technology,* **10**, 155-164, https://doi.org/10.1175/1520-0426(1993)010%3C0155:PAIOCD%3E2.0.CO;2

Lang, T. J., 2015: CSU_RadarTools. Accessed 01 November 2020, https://github.com/CSU-Radarmet/CSU_RadarTools

Liu, H., and V. Chandrasekar, 2000: Classification of hydrometeors based on polarimetric radar measurements: Development of fuzzy logic and neuro-fuzzy systems, and in situ verification. *Journal of Atmospheric and Oceanic Technology,* **17**, 140–164, https://doi.org/10.1175/1520-0426(2000)017%3C0140:COHBOP%3E2.0.CO;2

Marzano, F. S., D. Scaranari, M. Montopoli, and G. Vulpiani 2008: Supervised classification and estimation of hydrometeors from C-band dual-polarized radars: a Bayesian approach.

IEEE Transactions on Geoscience and Remote Sensing, **46**, 85-98, https://doi.org/10.1109/TGRS.2007.906476

Rauber, R. M., and S. W. Nesbitt, 2018: *Radar Meteorology, A First Course*. Wiley Blackwell, 461pp.

Rison, W., R. J. Thomas, P. R. Krehbiel, T. Hamlin, and J. Harlin, 1999: A GPS-based three-dimensional lightning mapping system: initial observations in Central New Mexico. *Geophysical Research Letters,* **26**, 3573-3576, https://doi.org/10.1029/1999GL010856

Umehara, A., T. Koike, K. Yamamoto, N. Nagumo, and H. Yamauchi, 2019: Development of a practical hydrometeor classification algorithm via a Bayesian approach using C-band dual-polarization radar. *39th International Conference on Radar Meteorology*, Nara, Japan, Poster2-63, https://cscenter.co.jp/icrm2019/program/data/abstracts/Poster2-63.pdf

Wen, G., A. Protat, P. T. May, X. Wang, and W. Moran, 2015: A cluster-based method for hydrometeor classification using polarimetric variables. Part I: interpretation and analysis. *Journal of Atmospheric and Oceanic Technology,* **32**, 1320-1340, https://doi.org/10.1175/JTECH-D-13-00178.1

Wen, G., A. Protat, P. T. May, W. Moran, and M. Dixon, 2016: A cluster-based method for hydrometeor classification using polarimetric variables. Part II: classification. *Journal of Atmospheric and Oceanic Technology,* **33**, 45-60, https://doi.org/10.1175/JTECH-D-14-00084.1

Yang, J., K. Zhao, G. Zhang, G. Chen, H. Huang, and H. Chen, 2019: A Bayesian hydrometeor classification algorithm for C-band polarimetric radar. *Remote Sensing,* **11**, 1884, https://doi.org/10.3390/rs11161884

Chapter 3
Radar characteristics of summer thunderstorms in the Kanto Plain of Japan with and without cloud-to-ground lightning

3.1 Introduction

Severe weather phenomena, including tornadoes, exceptional wind gusts, and lightning, are hazardous to society. Lightning strikes, for example, can cause injuries and fatalities (e.g., Curran et al. 2000; Elsom and Webb 2014; Fujibe 2017), as well as considerable disruption to aircraft operation (e.g., Mills et al. 2010). The mechanism of lightning initiation for an observed thunderstorm in real time, however, is yet to be fully elucidated, and accurate predictors for nowcasting remain elusive (e.g., MacGorman and Rust 1998). Therefore, it is imperative for one to better understand the mechanism of lightning in a thunderstorm by radar observation, and constraining its controlling factors is crucial for improved lightning prediction.

Statistical investigations aiming to predict lightning activity have traditionally relied on a combination of lightning location data and radar reflectivity data. Such studies are based on the relationship between radar parameters and lightning occurrence. Gremillion and Orville (1999) investigated the relationship between lightning initiation and radar reflectivity in Florida using meteorological radar and the National Lightning Detection Network (NLDN) data. Their study concluded that the observed 40 dBZ radar reflectivity at the − 10 °C temperature height enabled the most effective prediction of cloud-to-ground lightning (CG), with the threshold of radar reflectivity for CG observed 7.5 min before CG was recorded. Similarly, Vincent et al. (2005) investigated the relationship between radar observation and the NLDN data for 50 thunderstorms occurring over a 13-day period in North Carolina, and noted that the best critical success index (CSI) was found at a threshold of 40 dBZ radar reflectivity, also at the height of the − 10 °C isotherm, followed by 40 dBZ and a − 15 °C temperature height. They obtained 14.7 and 11.0 min as the times between radar observations and between lightning initiations, respectively. Many studies support these observations, suggesting that the 40 dBZ radar reflectivity at the − 10 °C

temperature height is a good indicator for lightning prediction (e.g., Mosier et al. 2010; Yang and King 2010). Another approach for predicting CG involves investigating the relationship between lightning and vertically integrated liquid water content (VIL; Greene and Clark 1972). VIL is obtained using radar volume scanning and radar echo top height. Studying the relationship between CG and echo top height and VIL in Oklahoma on June 9, 1993, Watson et al. (1995) found that the occurrence rate of radar echo with CG increased when the echo top height exceeded 15.2 km; however, the relationship between VIL and CG remained unclear. The echo frequency with CG increased gradually for VIL values between 15 and approximately 40–45 kg m^{-2}, but decreased at values ≥ 45 kg m^{-2}. Shafer et al. (2000), examining the relationship between CG and radar reflectivity and VIL for a severe storm in Oklahoma, noted that CG flashes were absent until the radar reflectivity reached 46 dBZ and VIL exceeded 10 kg m^{-2}, such that storms were generated along and ahead of the dryline. Liu and Zipser (2008) used Tropical Rainfall Measuring Mission (TRMM, Kummerow et al. 2000) satellite observations to demonstrate that the diurnal cycle of the 20 dBZ radar reflectivity above the 14 km altitude over land regions between 20° N and 20° S coincided with CG occurrence frequency. Using TRMM observations, many studies clarified that the diurnal cycle of deep convection indicated by radar reflectivity and echo top height coincided with lightning activity over land in the tropical and subtropical regions (e.g., Xu and Zipser 2011; Yuan et al. 2012; Roy and Balling 2013a, b; Kiany et al. 2018). Michimoto (1991) investigated winter lightning in the Hokuriku region of Japan and indicated that the first lightning strike occurred approximately 5 min after the observation of a 30 dBZ radar reflectivity at a − 20 °C temperature height.

Lang and Rutledge (2011) used a cell identification technique developed by Dixon and Wiener (1993) involving Thunderstorm Identification, Tracking, Analysis, and Nowcasting (TITAN) to automatically track precipitation cells. They performed statistical analyses of the relationships between the lightning flash rate and radar parameters in cells and analyzed CG and intra-cloud lightning (IC) based on radar data obtained from Severe Thunderstorm Electrification and Precipitation Study (STEPS; Lang et al. 2004) of Summer 2000 in the central United States. They applied a modified TITAN (Rowe et al. 2011), combining the identified cells and considering the vertical structure, to evaluate significant features of the radar data in those cells

producing lightning. By classifying cells based on CG, polarity, and radar echoes, 30 dBZ radar reflectivity above the freezing level (0 °C isotherm layer) was deemed to be a necessary condition for CG lightning, whereas 40 dBZ radar reflectivity at the freezing level was deemed a sufficient condition (Gremillion and Orville 1999). Although Lang and Rutledge (2011) utilized a cell-tracking algorithm, snapshot data sets were employed to classify cells based on CG and IC, without considering the life stage of the cell. Consequently, features of individual cells were not tracked in their study, excluding the possibility of examining storm evolution, cell mergers, and splits. These limitations in investigating the characteristics of a radar echo during the lifetime of a cell for each type of lightning discharge mean that Lang and Rutledge's method is not suitable for examining thunderstorm evolution with lightning activity.

The purpose of this chapter is to investigate the characteristics of cells classified based on lightning activity through the combination of radar data, cell-tracking data, and lightning data for summertime thunderstorms in the Kanto Plain, central Japan. Statistical features of radar echoes throughout the lifetimes of thunderstorms with or without lightning are also classified using cell-tracking. The applicability of 40 dBZ radar reflectivity at the − 10 °C temperature height threshold for lightning prediction described in the previous studies is examined for use during Japanese summertime datasets. Furthermore, appropriate indices for lightning prediction are proposed for summertime thunderstorms in Japan.

3.2 Data and methods

3.2.1 Radar and lightning data for the analyzed area

Three-dimensional (3D) conventional weather radar data, two-dimensional (2D) lightning location data, and radiosonde data were used in this study. Detailed descriptions of the data sets are given below.

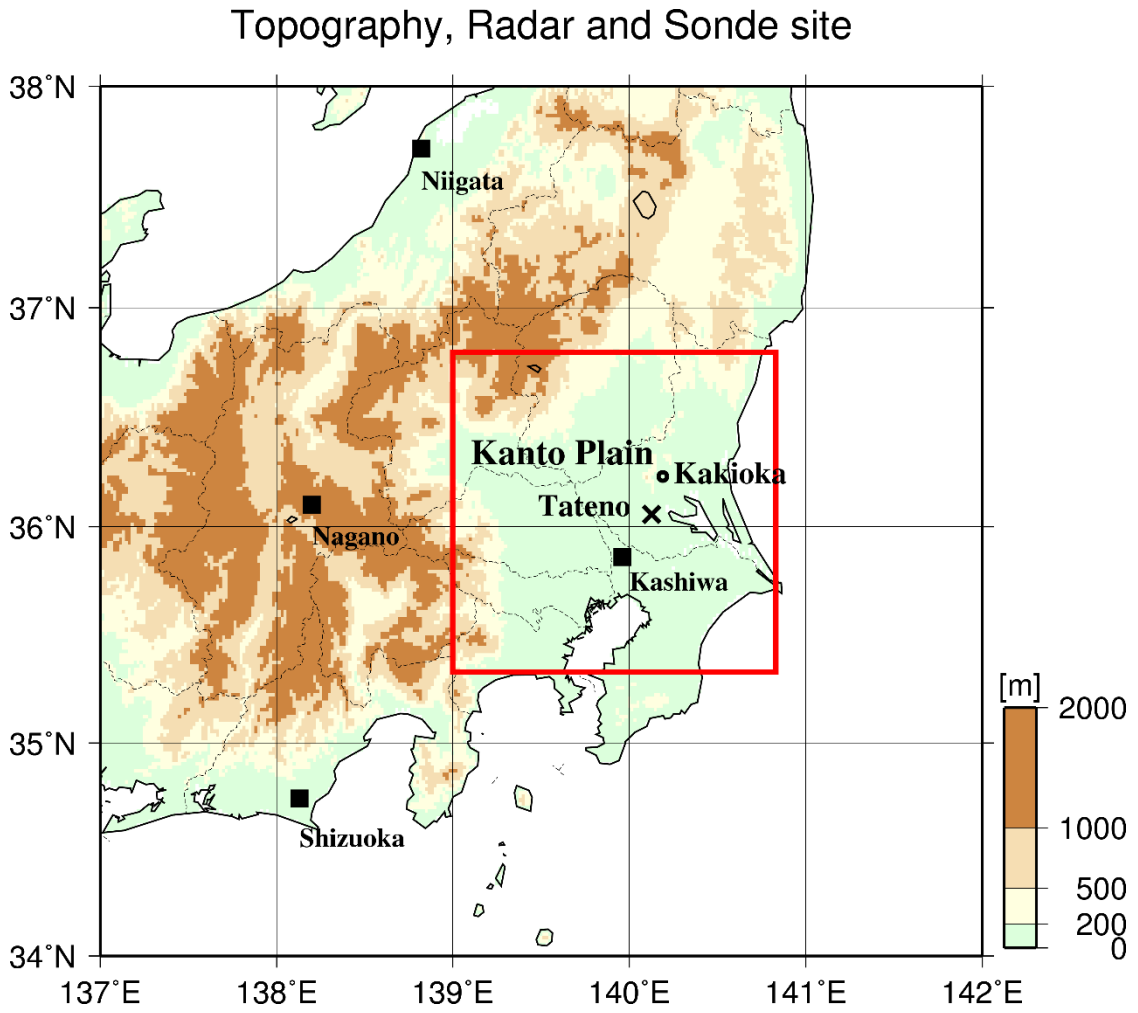

Figure 3.1 Topography of the central Japan (color shade), depicting the analysis area of the Kanto Plain for this study surrounded by the thick red square box (black square: the JMA operational radar location, black cross: the radiosonde site, and black circle: the JMA Kakioka surface rain gauge).

The analyzed area is located in the Kanto Plain, covering 160 km^2 between latitudes 35.3° N–36.8° N and longitudes 139.0° E–140.8° E (Fig. 3.1). It opens in both the south and east to the Pacific Ocean and is bound by mountains in the north and west. Aerological data used in this study are for 00:00 UTC (UTC = Japan Standard Time − 9 h) recordings of the Tateno radiosonde site (36.05° N, 140.13° E), which is operated by the JMA.

The JMA has 20 operational C-band weather radars across Japan. This study used data from the Kashiwa, Niigata, Nagano, and Shizuoka radar sites, which are located in and around the analyzed area (Fig. 3.1). The operational specifications of these radars include a 5.3 GHz frequency, a 5.6 cm wavelength, 16 elevation angles ranging from − 0.5° to 25.0°, a range resolution of 250 m, and a 1° azimuth resolution, with a volume scan performed every 10 min (Table 3.1). The JMA integrates radar data from these 20 sites to create 3D composite radar data that are stored every 10 min. The stored data are characterized by a 1 km horizontal resolution and a 1 km vertical resolution from longitudes 118° E–150° E and latitudes 20° N–48° N of the radar coverage area. From these composites, this study exploited data for isotherm height radar reflectivity with a vertical resolution of 5 °C (5 to − 35 °C: 9 layers), echo top height, and VIL.

The JMA has operated the lightning detection network (LIDEN) system since 2001 (Ishii et al. 2014) as a means of detecting the location of CG and IC over Japan (see Sec 1.1.2). The location of CG relies on the time of arrival method (Fig. 2.3), calculating the time difference between radiations received from CG by five or more antennas for the low-frequency band (Kawasaki et al. 1994). The location of IC is determined from the intersection of two azimuths calculated using the interferometric method for each antenna using the very high-frequency band (Hayenga and Warwick 1981). Location errors for CG and IC are a few kilometers. According to Ishii et al. (2014; Fig. 1.3b), the Kanto Plain is the most active area of lightning activity in Japan during summertime, with the majority of lightning being observed during the afternoon in inland areas.

Table 3.1 Hardware specifications and observation pattern of JMA operational radar.

	Specifications
Frequency	5.3 GHz (C-band)
Beam width	1.0 degree
Range	400 km radius
Range resolution	250 m
Volume scan	28 PPI (16 elevations), every 10 min.
Antenna rotation rate	4 rpm

3.2.3 Cell-tracking and lightning analysis

Cell-tracking was performed using the JMA 3D composite radar data based on TITAN (Dixon and Wiener 1993). The first step of TITAN involved selection of the area of the radar grid with continuous horizontal or vertical radar reflectivity greater than 35 dBZ. This was followed by an elliptic horizontal approximation of the selected area, with the elliptic area defined, herein, as the cell. Cell characterization was performed for each volume scan time (every 10 min in this study), and all identified cells were tracked by calculating the cost function through established criteria, thus quantitatively evaluating their relevance. The criteria for the cost function included the shortest center distance from a past cell location to present one and the similarity of radar data characteristics, including volume and speeds not exceeding the maximum possible traveling speed of the storm. Without considering cell mergers, the cell with the larger cost function reaches the end of its life; however, cell splits were considered, and after splitting, these cells are treated as multiple cells. In this study, TITAN was modified to enable a greater accuracy of tracking by considering the vertical structure of radar reflectivity in each cell. This led to improvement in two features: i) multiple layers exceeding 35 dBZ radar reflectivity were required in each cell, and ii) the history of each cell was maintained after splitting, with the entire lifetime of growth weakness recorded. TITAN cell-tracking results included cell identification numbers and histories, the center position, the elliptical parameter, and the area. LIDEN data for every 10 min were related to radar data with cell information including the lifetime, size, maximum echo top height, maximum radar reflectivity, maximum VIL, and CG and IC flash count. Those cells were then categorized as the "CGIC cell" to signify that they represented a cell with at least one CG occurrence during its lifetime (acceptable with the occurrence of ICs in its lifetime), the "IC cell" to denote a cell with only IC occurrences during its lifetime, and the "NoL cell" in the case of cells without either CG or IC occurrences. The statistical features of these three cell categories were then evaluated.

3.3 Cell characteristics

3.3.1 Overview

Analyses were performed for 00:00–24:00 UTC on July 25, 2010, and the locations and times of the CG are presented in Fig. 3.2(a). According to LIDEN observations, this day was notable for exhibiting the highest number of CG occurrences in the Kanto Plain in 2010. During the East Asian summer, thunderstorms with heavy precipitation and lightning frequently occur on the inland side near the coast in the afternoon (e.g., Hyun et al. 2010; Ishii et al. 2014).

On July 25, 2010, multiple thunderstorms occurred in the Kanto Plain because of strong surface heating since the early morning and a favorable environment for connective initiation (described later). The JMA rain gauge of Kakioka (36.23° N, 140.19° E, near the Tateno radiosonde site, black circle in Fig. 3.1) recorded 88.5 mm h^{-1} 1-hour accumulated rainfall at 10:30 UTC (19:30 local time), breaking the historical record of one-hour maximum rainfall at this site since 1976. Furthermore, rainfall exceeding 50 mm h^{-1} was recorded at three other surface JMA rain gauge sites near Kakioka.

Lightning activity was recorded by LIDEN (Fig. 3.2(a)). Most CG lightning occurred between 03:00 and 12:00 UTC (12:00–21:00 local time). For 03:00–08:00 UTC, CG lightning was primarily observed in the mountainous area to the north and west of the analyzed area. After 08:00 UTC, much CG lightning was observed in the central Kanto Plain, a rural and non-mountainous region, before moving eastward (Figs. 3.1, 3.2(a), (b)). Lightning activity and cell movements suggest that the observed cumulonimbus clouds are uncharacteristic of the frontline of a cyclone or a squall line. These clouds simultaneously developed in the Kanto Plain and moved eastward, with many cells being displaced more than 100 km.

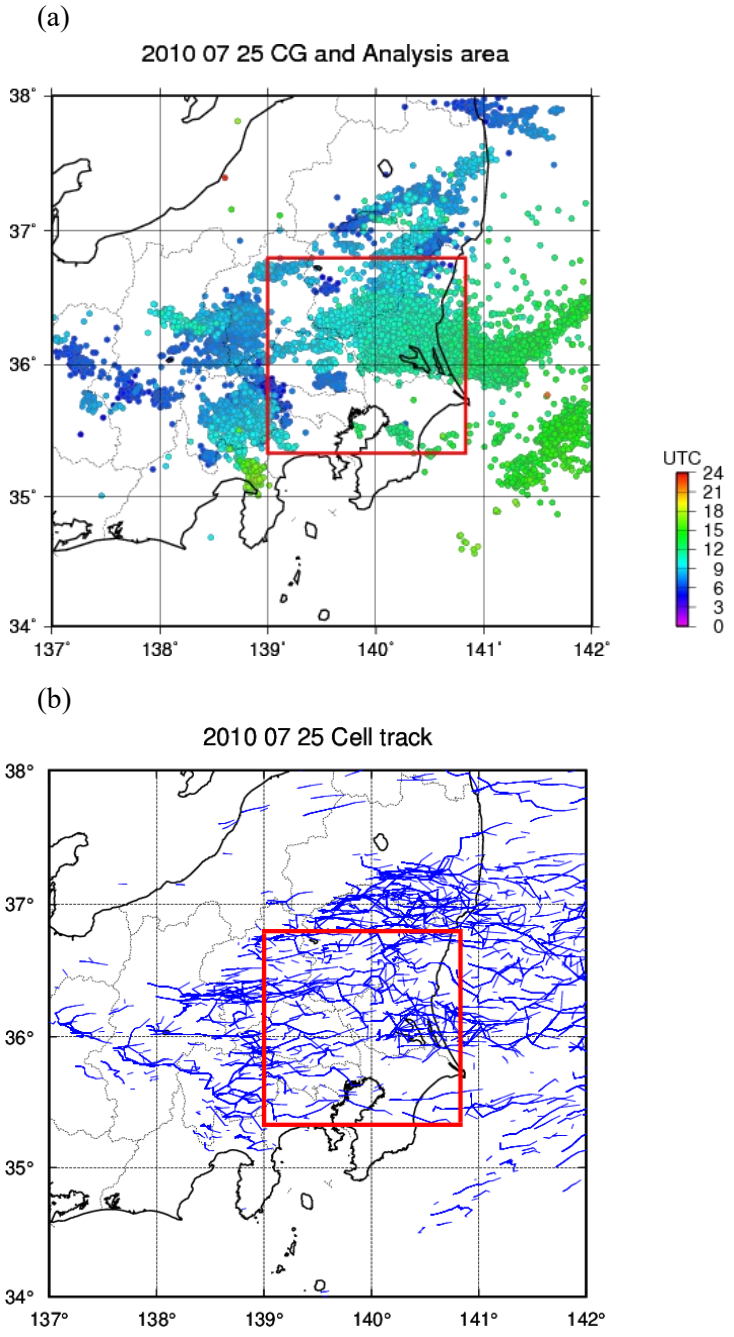

Figure 3.2 (a) Lightning location over time differentiated by color and (b) identified cell tracks. The red square box represents the same analysis area illustrated in Fig. 3.1

Unstable atmospheric conditions favorable for generating deep convection were observed by radiosonde at the Tateno site around 00:00 UTC on July 25, 2010 (Fig. 3.3). This observation was characterized by the convective available potential energy (CAPE) of 750 J kg^{-1}, a convective inhibition (CIN) of 190 J kg^{-1}, a lifting condensation level of 849 m (921 hPa equivalent), a level of free convection (LFC) around 3539 m (671 hPa equivalent), and a level of neutral buoyancy (LNB) of 12,240 m (206 hPa equivalent). The isotherm height, considered important for charge separation and lightning initiation (e.g., Takahashi 1978; Saunders and Peck 1998; MacGorman and Rust 1998), was 4.6 km at 0 °C, 6.5 km at − 10 °C, and 8.1 km at − 20 °C, respectively. In the morning of July 25, strong surface heating was noted, and surface air temperatures exceeding 30 °C were recorded in the Kanto Plain. Although the high LFC was disadvantageous to the initiation of deep convection, an air parcel ascended to the cloud top to attain the 12 km equivalent to the LNB after reaching the LFC due to buoyancy imparted by strong surface heating. The 12 km LNB exhibited a sufficiently cold temperature to contain ice crystals and graupels, which are important for lightning discharge in cumulonimbus clouds (e.g., MacGorman and Rust 1998).

3.3.2 Radar observation and cell-tracking

A total of 265 cells were observed in the region of analysis on July 25, 2010 (Fig. 3.2(b)). Among these cells, 103 were identified as CGIC cells (including those with both CG and IC in their lifetime), 30 were IC cells (IC only), and 132 were NoL cells (neither CG nor IC). There was no CG-only cell. The lifetime, area, and average value for each radar parameter are presented in Table 3.2. The values are averaged from the start to the end of the cell-tracking of the cells identified in each category. Underlined values in Table 3.2 indicate all values exhibiting statistically significant differences (p value < 0.01).

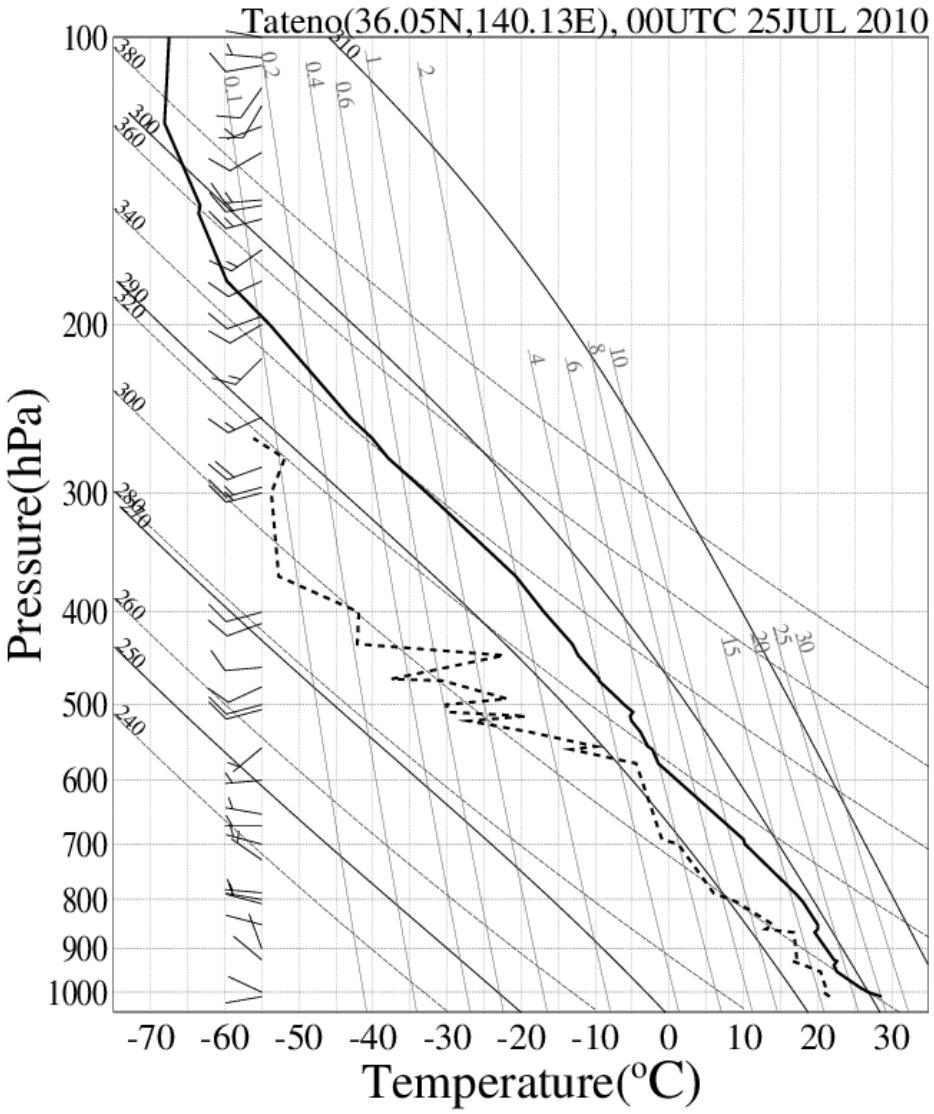

Figure 3.3 Vertical profile of atmosphere by radiosonde observation at Tateno at 00:00 UTC on July 25, 2010. Temperature (thick black line), dew point temperature (dashed line), wind speed and direction (wind barb, on − 55 °C with pressure axis).

Table 3.2 Comparison of averaged values for radar parameters associated with CGIC, IC, and NoL cells

	CGIC cell	IC cell	NoL cell	ALL
No. of cells	103	30	132	265
Lifetime (min)	110.6	64.0	22.0	65.5
Size (km^2)	234.2	174.9	110.9	173.3
Echo top (m)	13.7	12.6	10.9	
VIL ($kg\ m^{-2}$)	10.8	3.4	2.9	
Maximum radar reflectivity	46.6	40.3	37.0	
Radar reflectivity at the −10 ° C isotherm	41.6	33.7	30.0	

Underlined values indicate statistically significant differences from each cell categories (p value < 0.01)

CGIC cells that produced CG lightning had the highest values for lifetime, area, echo top height, VIL, maximum radar reflectivity, and radar reflectivity at the − 10 °C isotherm height (Table 3.2). Furthermore, CGIC cells have twice the lifetime of IC cells and quintuple that of NoL cells, whereas the area of CGIC cells is 1.3 times that of IC cells and twice that of NoL cells, respectively. The echo top values of CGIC cells are 1 km higher than those of IC cells and 3 km higher than those of NoL cells. VIL in CGIC cells is more than three times higher than that in IC and NoL cells. At maximum values of radar reflectivity, the reflectivity is 6.3 dBZ higher in CGIC cells than that in IC cells and 9.6 dBZ higher than that in NoL cells. For the radar reflectivity at the − 10 °C isotherm height, values in CGIC cells exceed those in IC cells by 7.9 dBZ and those in NoL cells by 11.6 dBZ, with the differences higher than the maximum radar reflectivity. Comparing the IC and NoL cells, the former has higher values in all of lifetimes, areas, echo top heights, VILs, maximum radar reflectivities, and radar reflectivities at the − 10 °C isotherm height; however, the magnitudes of the differences are smaller than those between the CGIC cells and the IC cells. These results demonstrate that CGIC cells have the longest lifetime, largest area, highest echo top height, largest maximum radar reflectivity, and largest radar reflectivity at the − 10 °C isotherm height. This suggests that the CGIC cell represents a cumulonimbus cloud

with larger and stronger updraft compared to those of the other cells. Although IC cells have values between those of the CGIC cells and the NoL cells, they exhibit characteristics similar to those of NoL cells, with the exception of lifetime, area, and echo top.

The average values of features for lightning activity and area according to the lifetimes of CGIC cells are given in Table 3.3. CGIC cells with lifetimes below 20 min are characterized by small areas, indicating low lightning activity. When the lifetime exceeds 50 min, the cell areas exceed 200 km^2, and the flash rate increases. The maximum number of CGIC cells appears at a lifetime of 90 min, followed by 100 min and 140 min. CGIC cells with a lifetime of 150 min have the highest flash rates peak, and cells with a lifetime of 60 min have the second greatest peak. CGIC cells with a 150-min lifetime correspond to the largest area, around 386 km^2. The lifetimes and areas of CGIC cells are positively correlated up to a lifetime of 60 min, but no correlation exists beyond this point. No correlation exists between the CGIC cell lifetime and the CG flash rate and between the CGIC cell lifetime and the IC flash rate. Similarly, there is no correlation between cell lifetime and the total number of CG and IC cells. The average CG flash rate in all CGIC cells, approximately 0.65 min^{-1}, was found to be approximately five times lower than the corresponding IC flash rate of 3.13 min^{-1}. The averaged area of all CGIC cells is 234.2 km^2, i.e., it can be approximated to a square with a side length of 15 km. This is smaller than the averaged single flash area, which is 25 km^2 (Yoshida et al. 2018).

Table 3.3 Number of CGIC cells, CG and IC lightning activity, and area in each lifetime

Lifetime (min)	number	CG / cell in lifetime	CG / min Flash rate	IC / cell in lifetime	IC / min Flash rate	area / cell [km^2]
10	9	3.7	0.4	18.6	1.9	83.9
20	3	4.0	0.2	40.3	2.0	72.2
30	2	6.5	0.2	138.5	4.6	178.5
40	5	28.0	0.7	123.6	3.1	179.7
50	4	54.8	1.1	254.8	5.1	235.1
60	2	94.5	1.6	460.0	7.7	261.7
70	6	14.5	0.2	39.5	0.6	232.9
80	3	35.7	0.5	70.0	0.9	229.6
90	10	61.1	0.7	289.0	3.2	256.8
100	9	93.1	0.9	559.4	5.6	262.4
110	7	82.1	0.8	295.7	2.7	277.4
120	7	102.0	0.9	496.1	4.1	266.9
130	1	37.0	0.3	7.0	0.1	246.9
140	8	109.5	0.8	566.0	4.0	308.8
150	3	265.7	1.8	1180.3	7.9	385.6
160	4	168.8	1.1	886.5	5.5	325.2
170	4	56.8	0.3	183.8	1.1	295.6
180	3	68.0	0.4	45.7	0.3	322.7
190	1	2.0	0.0	2.0	0.0	261.8
200	3	204.0	1.0	1228.3	6.1	313.4
210	2	51.0	0.2	39.5	0.2	319.8
220	1	2.0	0.0	2.0	0.0	265.7
230	2	51.0	0.2	41.0	0.2	315.8
240	2	51.5	0.2	35.0	0.2	327.3
>240	2	4.0	0.0	1.0	0.0	219.1
Average	103	70.7	0.65	324.8	3.13	234.2

(a)

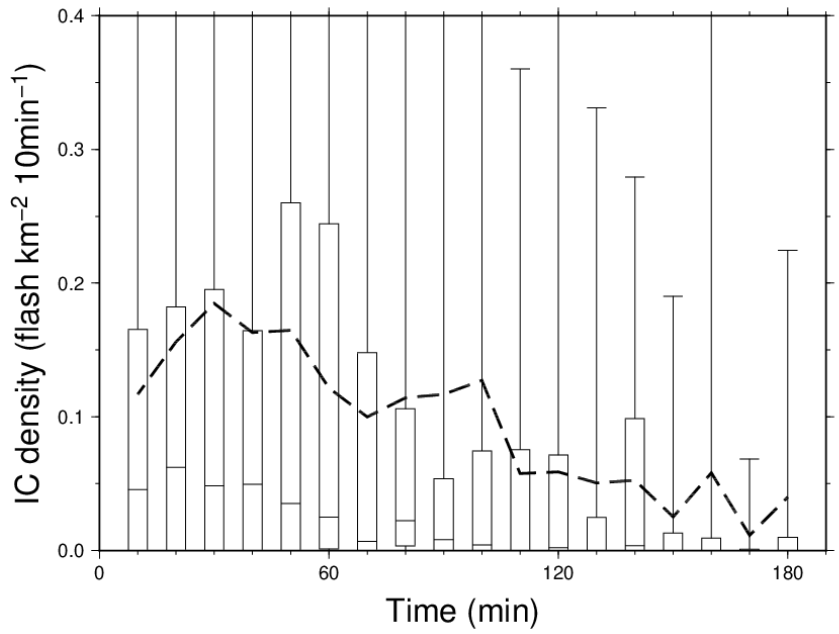

(b)

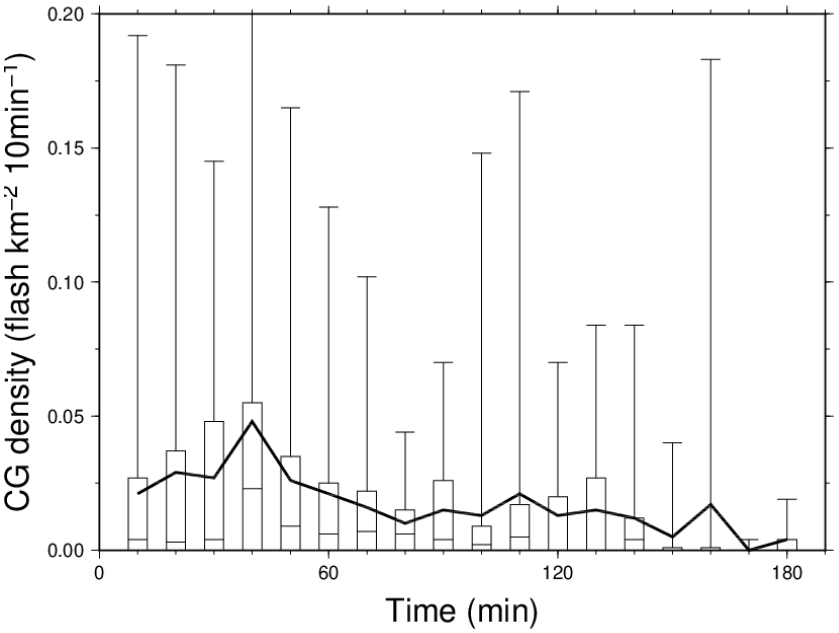

Figure 3.4 Box and whisker plot for lightning activity as a time-series for (a) IC and (b) CG in 10-min intervals for the CGIC cell. Solid and dashed lines indicate the respective averages. The box at each time depicts the median and quarter value, and the upper and lower ends of the bar are indicative of the maximum and minimum values, respectively

The average 10-min IC flash rate peaked earlier (30 min into the cell lifetime) than the CG flash rate (which peaked at 40 min) (Fig. 3.4). The median of the CG flash rate also peaked at 40 min, whereas the median of the IC flash rate peaked earlier, at around 20 min, and gradually decreased until 70 min. After the peak in both the mean and the median of CG and IC flash rates, both gradually decreased. Ohno (2001) noted that the maximum value of CG density occurs during the mature stage of the thunderstorm. In this study, CG activity yielded a maximum peak 40 min after a cell was identified, and CG activity declined thereafter; these findings are consistent with those of Ohno (2001). The appearance of the IC peak before that of the CG peak in cumulonimbus clouds was previously found by MacGorman et al. (1989) and MacGorman et al. (2011). The first peak at 30–40 min is clearer than the second peak at 100–110 min. Contrarily, the second peak may have a larger deviation than the first one. The small peak at 160 min occurs, because the median and quarter values are close to 0, such that the average value is strongly affected by the small number of long-lived cells.

The averaged time-series of echo top heights for the three cell categories indicates the highest echo top heights, on average, for cells that produce CG lightning, which consistently exceed 13 km (Fig. 3.5). This height exceeds the LNB and is close to the tropopause. Clearly, the CGIC cell is accompanied by strong buoyancy and upward motion. The height of the echo top is lower in the IC cell (dashed line) than in the CGIC cell (solid line), followed by that in the NoL cell (gray line). The echo top height of the NoL cell does not reach the LNB, suggesting limited buoyancy or upward motion. The echo top height of the IC cell is intermediate between that of the CGIC cell and that of the NoL cell. The echo top height of the CGIC cell increases monotonously up to 50 min, at which point it yields the highest value of 14.5 km. This maximum occurs 10 min after the CG density peak illustrated in Fig. 3.4(a). Taken together, these results suggest a close relationship between the vertical development of the cumulonimbus and corresponding lightning activity (e.g., Yoshida et al. 2017). These data also indicate that the peak of the echo top is unsuitable as a lightning index, because it lags behind the peak of CG activity.

The time-series variation of VIL according to the categories in Fig. 3.5, is illustrated in Fig. 3.6. At any time, the VIL of CGIC cells is three-to-five times higher than that of other cell categories, whereas the VIL of IC cells is slightly higher than that of NoL cells. The VIL of CGIC cells peaks around 20.2 kg m^{-2} at 30 min after the cell identification. This coincides with the peak IC activity, but occurs 10 min before the peak CG flash rate (Fig. 3.4), indicating that maximum lightning activity is attained simultaneously or immediately after the emergence of a vertically continuous strong radar reflectivity. This is also consistent with the report of Shafer et al. (2000), indicating that the presence of large particles indicating strong radar reflectivity in the cumulonimbus is important for a high lightning flash rate.

The time-series of vertical radar reflectivity by isotherm height averaged across each cell category is displayed in Fig. 3.7(a) (CGIC cell), Fig. 3.7(b) (IC cell), and Fig. 3.7(c) (NoL cell). Isotherm height was converted from the observed altitude and temperature using the radiosonde observation data at 00:00 UTC at the Tateno site (Fig. 3.3), which is almost the same isotherm height at 12:00 UTC at Tateno (not shown). The abscissa represents the elapsed time from the start of cell identification.

In the CGIC cell (Fig. 3.7(a)), the radar reflectivity exceeding 40 dBZ rapidly reaches the − 35 °C isotherm height from 10 to 30 min, coinciding with a sharp increase in IC density. At around 30–40 min, a region in which radar reflectivity is equal to or greater than 48 dBZ is observed in the lower portion of the cloud at the 0 to − 5 °C isotherm height, whereas a region of 46 dBZ or higher is widely observed between the − 5 to − 15 °C isotherm height. The maximum CG density is observed at 40 min, and the appearance of a secondary CG density peak at approximately 110 min coincides with the emergence of a region of 44 dBZ or higher reflectivity at the 5–0 °C isotherm height. A region of 42 dBZ is observed around the − 5 °C isotherm height at 90 min, expanding to the − 10 °C isotherm height at 110 min. Concurrently, CG density indicates a small peak at 110 min, although a radar reflectivity of 42 dBZ observed at the − 10 °C isotherm height at 80 min indicates no CG density peak. The cause of the difference between the two small CG peaks remains unclear.

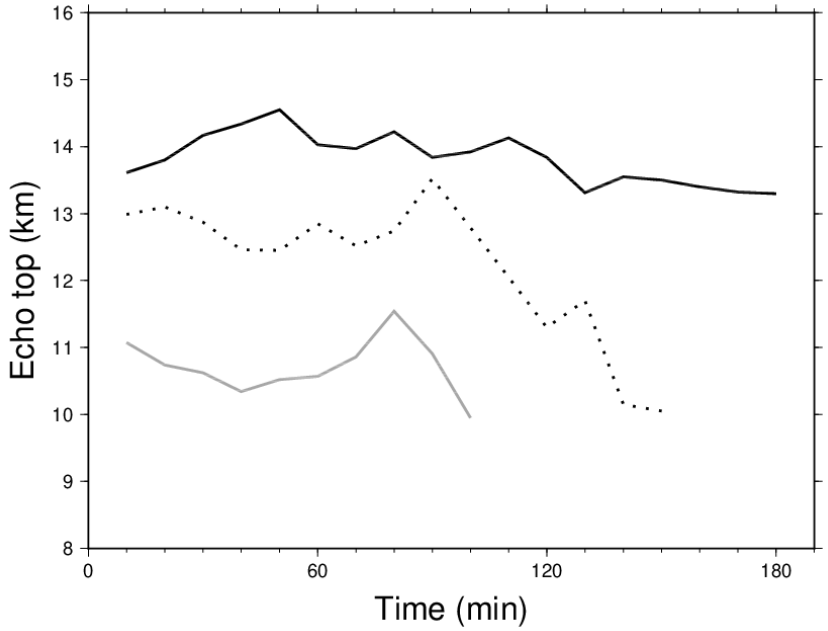

Figure 3.5 Time-series of the averaged echo top height with a solid line for the CGIC cell, a dashed line for the IC cell, and a gray line for the NoL cell at 10-min intervals.

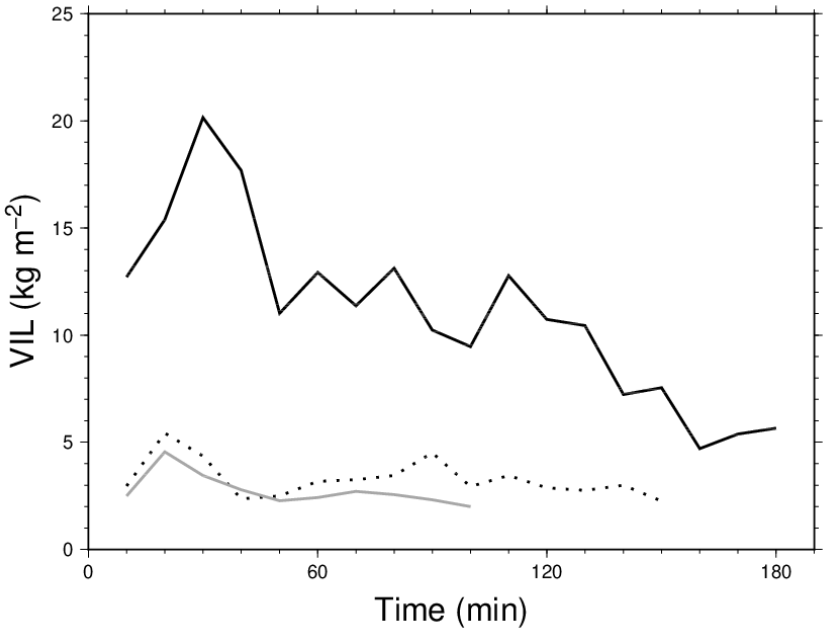

Figure 3.6 Same as Fig. 3.5, except for time series of averaged VIL.

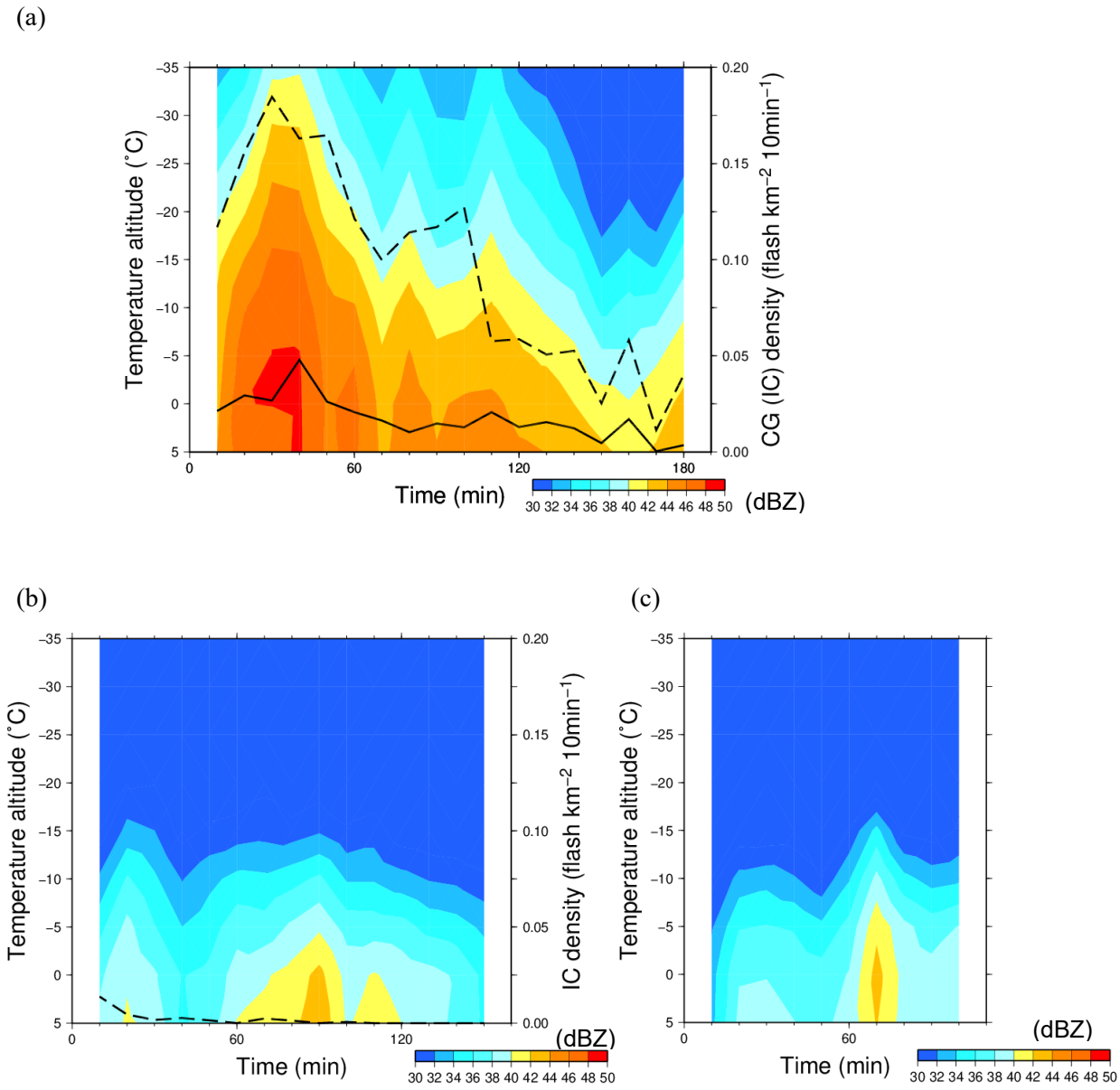

Figure 3.7 The vertical profile of the composite radar reflectivity (dBZ) over time for (a) the CGIC cell, (b) the IC cell, and (c) the NoL cell. The solid line represents the CG lightning activity, whereas the dashed line represents the IC lightning activity at 10-min intervals

After the secondary peak of CG density at 110 min, the area of strong radar reflectivity exceeding 40 dBZ shrinks rapidly at 140 min in the upper freezing level; simultaneously, CG and IC flash rates decrease. These results indicate radar reflectivity exceeding 42 dBZ around the 0 to − 10 °C isotherm height in the middle portion of the thunderstorm, when the CG flash rate increases. Additionally, IC density increases when the region of radar reflectivity exceeding 40 dBZ reaches a lower temperature, corresponding to a higher altitude in the cumulonimbus. According to the charge separation mechanism of Takahashi (1978), the formation of graupel or hail and the presence of supercooled water around the − 10 °C isotherm height are considered to be the most important factors in charge production and separation in thunderclouds. In this study, maximum CG densities were observed at 40 min, 10 minutes after the strongest radar reflectivity region had appeared in the isotherm layer from 0 to − 5 °C at 30 min; therefore, the presence of graupel or hail is strongly suggested. In addition, Figure 3.7 demonstrates that the large VIL of the CGIC cell in Fig. 3.6 is caused by the presence of deep convection with a high echo top and strong radar reflectivity.

A region of radar reflectivity of 42 dBZ or higher appears locally near the 0 °C isotherm in the IC cell (Fig. 3.7(b)), but its radar reflectivity and duration are lower than those of the CGIC cell. In the CGIC cell, the altitude in the region of 40 dBZ exceeds the − 30 °C isotherm, but the IC cell does not reach the altitude of the − 15 °C isotherm, even in the region of 34 dBZ radar reflectivity. This is consistent with the low echo top height and small VIL indicated in Figs. 3.5 and 3.6, respectively. Similarly, the NoL cell (Fig. 3.7(c)) exhibits a weaker radar reflectivity, and its height is lower than that of the CGIC cell. The time at which radar reflectivity exceeds 40 dBZ is even shorter than that in the IC cell. From these results, the region of radar reflectivity exceeding 44 dBZ at the 0 to − 5 °C isotherm height is a feature appearing only in the CGIC cell, suggesting a strong relationship between the existence of graupel and high CG and IC flash rates.

3.3.3 Lightning index

This section examines prediction scores of radar observations as lightning indices. The threshold of VIL and maximum radar reflectivity at each temperature height were verified as lightning indices. This verification was performed by the same method used in the weather

forecast. Individual cells were classified into categories including Hit, False, Miss, and No–No. Within 20 min (0, 10, and 20 min were used) after exceeding the threshold set for each radar parameter, a cell that observed CG for the first time in its lifetime was set as Hit. Cases where CG was not observed within 20 min, even when the threshold was exceeded, were False, whereas those where CG was observed without exceeding the threshold were Miss. Cases in which CG and the exceeding threshold were not observed were referred to as No–No (not used in this study). These evaluations were made using the CSI, the probability of detection (PoD), and the false alarm rate (FAR) according to the following equations (Wilks 2011):

$$\mathrm{CSI} = \mathrm{Hit} / (\mathrm{Hit} + \mathrm{Miss} + \mathrm{False}),$$

$$\mathrm{PoD} = \mathrm{Hit} / (\mathrm{Hit} + \mathrm{Miss}) \text{ and}$$

$$\mathrm{FAR} = \mathrm{False} / (\mathrm{Hit} + \mathrm{False}).$$

When CSI and PoD are close to 1 and FAR is close to 0, the prediction accuracy increases.

The CG prediction score for each threshold of VIL is presented in Table 3.4(a). Watson et al. (1995) stated that the rate of lightning activity increased when VIL exceeded 15.0 kg m^2, and Shafer et al. (2000) found that lightning occurred only when VIL exceeded 10.0 kg m^2. In this study, using VIL of 15.0 kg m^2 as the threshold, the first CG of the cell occurred in 55 out of the 265 cases, yielding a CSI of 0.50, a PoD of 0.54, and an FAR of 0.14. The FAR is the lowest of all VIL thresholds and, even when a threshold VIL of 10.0 kg m^2 is used, the CSI is highest at 0.66, with high PoD and low FAR, synthetically demonstrating the best index among the VIL thresholds. In this study, although the value of FAR at VIL of 15.0 kg m^2 was the lowest among the VIL thresholds, the 10.0 kg m^2 threshold was found to be the most appropriate out of the CSI, PoD and FAR. These results are consistent with those of Watson et al. (1995) and Shafer et al. (2000).

Table 3.4 Statistical scores (CSI, PoD, and FAR) with the various thresholds: (a) from VIL, (b) from radar reflectivity at − 10 °C, (c) at − 20 °C, and (d) at − 30 °C isotherm heights

(a)

VIL	5.0 kg/m^2	10.0 kg/m^2	15.0 kg/m^2	20.0 kg/m^2
CSI	0.59	0.66	0.50	0.30
PoD	0.85	0.82	0.54	0.32
FAR	0.33	0.22	0.14	0.18

(b)

Radar Reflectivity −10 °C	30 dBZ	35 dBZ	40 dBZ	45 dBZ
CSI	0.41	0.54	0.59	0.64
PoD	1.00	0.90	0.85	0.76
FAR	0.59	0.43	0.34	0.19

(c)

Radar Reflectivity −20 °C	30 dBZ	35 dBZ	40 dBZ	45 dBZ
CSI	0.58	0.66	0.75	0.69
PoD	0.96	0.87	0.84	0.74
FAR	0.40	0.27	0.12	0.07

(d)

Radar Reflectivity −30 °C	30 dBZ	35 dBZ	40 dBZ	45 dBZ
CSI	0.76	0.82	0.73	0.41
PoD	0.87	0.86	0.75	0.41
FAR	0.14	0.06	0.03	0.00

CG prediction scores, with radar reflectivity at the isotherm height chosen as a threshold, are presented in Table 3.4(b)–(d). Higher isotherm height and lower radar reflectivity threshold result in larger values of PoD, indicating that the prediction target is expanded when the region of lower radar reflectivity is included in the higher temperature area, and the number of Miss cells is consequently reduced. However, because the number of cells analyzed increases, the number of False cells also increases, resulting in high FAR values. Therefore, a high PoD is not sufficient for displaying a good score. The CSI with the best prediction accuracy is that of the 35 dBZ radar reflectivity at the − 30 °C isotherm, with a CSI of 0.82, a PoD of 0.86, and an FAR of 0.06. This threshold yields well-balanced values with high CSI, high PoD, and low FAR. Previous research by Gremillion and Orville (1999) stated that the best prediction was 40 dBZ at the − 10 °C isotherm, based on an investigation of summer lightning in the USA. When this criterion is applied in this study, it yields a CSI of 0.59, a PoD of 0.85, and an FAR of 0.34. Although the detection rate based on this criterion is high, the FAR is also high. These results suggest that a better threshold of radar reflectivity for summer lightning in Japan is lower than that for cases of Gremillion and Orville's study, and this can be attributed to differences in the strength and structure of updrafts inside the cumulonimbus associated with the different atmospheric conditions. However, these differences are beyond the scope of this study and will be the subject of future work.

3.4 Summary and conclusions

In this chapter, the author investigated the relationship between radar observations and lightning activity in the lightning lifetime using a cell-tracking method. The author classified cells into CGIC, IC, and NoL cells according to the characteristic type of lightning discharge and demonstrated statistically significant differences for each radar observation. Since these cells occurred in the same area and at the same period, it was difficult to distinguish the type of cell according to lightning discharge purely based on their geographical location and time. CGIC cells had the largest values of lifetime, area, echo top height, VIL, maximum radar reflectivity, and radar reflectivity at the − 10 °C isotherm height. NoL cells yielded the lowest values, whereas IC cells produced intermediate values. The features of CGIC cells depicted here are consistent with

the previous studies (e.g., Shafer et al. 2000; Lang and Rutledge 2011). This study demonstrates that the values of CGIC cells are significantly different from those of IC and NoL cells. The VIL and the maximum radar reflectivity of the CGIC cells had especially large differences when compared to corresponding values in IC and NoL cells, and are, therefore, considered to be good indicators of lightning. These results were obtained by tracking the cells and classifying the type of lightning occurring during their lifetime. As highlighted in Sec. 3.3.2, the lifetime and area of CGIC cells were simultaneously increased until 60 min after cell identification, but the relation became unclear thereafter. No correlation exists among cell lifetime, the total number of lightning flashes, and the flash rate. Multiple peaks of lightning activity suggest that small secondary peaks are caused by differences in the timing of the second and subsequent updraft occurrence of each cell in the case of long-lived cells (Fig. 3.4). This result highlights the difficulty of predicting lightning activity using the second and subsequent peaks, even though the cells can be traced to their lifetime. The echo top height of the CGIC cells monotonously increased up to 10 min after the first peak of CG activity and then gradually declined regardless of the CG activity. The relationship between the increases in CG activity and echo top height appearing in the first peak is consistent with the findings of Yoshida et al. (2017); however, this relationship was unclear during the latter part of the lifetime. Moreover, in this case, the peak of the echo top height appeared later than the peak CG activity, suggesting that the echo top height is an unsuitable predictor of lightning activity.

The characteristics of the lifetime of the CGIC, IC, and NoL cells throughout their lifetime were clarified through the temporal variation of the vertical distribution of radar reflectivity (Fig. 3.7). In this study, the author traced temporal variations in the radar reflectivity of each cell category for the ice phase area, which is considered important for charge production and separation (e.g., Takahashi 1978; Saunders and Peck 1998). CGIC cells had the strongest radar reflectivity above the freezing level. The peak CG activity at 40 min after cell identification coincided with the radar reflectivity region exceeding 48 dBZ at the 0 to − 5 °C isotherm height from 20 to 40 min. This feature was absent in IC and NoL cells. The existence of a radar reflectivity region exceeding 48 dBZ above the 0 °C isotherm height coupled with graupel occurrence and lightning initiation, stated in previous studies, suggests the presence of graupel in

this region. In addition, temporal variations in the vertical distribution of radar reflectivity exceeding 42 dBZ appears to correspond to the activity of CG and IC, suggesting a correlation between the vertical development of cumulonimbus and lightning activity. The vertical extension of strong radar reflectivity in the CGIC cells explains why a large VIL emerges only for CGIC cells (Fig. 3.6).

The accuracy of the lightning index using radar parameters was also evaluated. A VIL of 10.0 kg m^{-2} emerged as a good threshold, although it was found to be better to use maximum radar reflectivity at an isotherm height as a lightning index. For the maximum radar reflectivity, the 40 dBZ at the − 10 °C temperature height threshold adopted in the previous research (e.g., Gremillion and Orville 1999) produced lower scores of 0.59 for CSI, 0.85 for PoD, and 0.34 for FAR. In this study, a threshold of 35 dBZ at the − 30 °C height delivered better scores of 0.82 for CSI, 0.86 for PoD and 0.06 for FAR. Differences in the threshold may be explained by the existence of a strong radar reflectivity region at lower temperatures, which is an indicator of deep vertical growth of the cumulonimbus and, consequently, facilitates a demonstration of the existence of graupel and charge production. However, the reason for the high score for the radar reflectivity at a higher altitude in this study remains unclear. Many previous studies targeted North America (Antonescu et al. 2013); therefore, the inconsistencies noted may be caused by differences in the strength and structure of updrafts inside cumulonimbus associated with variations in atmospheric conditions between the USA and Japan.

The present study reveals significant differences between CGIC, IC, and NoL cells that are identifiable through radar observations during their lifetimes and allow cell-tracking of summertime thunderstorms. This work has also produced values of lightning indices using radar observations. The applicability of these indices in different atmospheric conditions remains unclear, because this study was conducted using radar data corresponding to only 1 day. The investigation of generalized lightning indices will, therefore, be a future research topic.

References of Chapter 3

Antonescu, B., S. Burcea, and A. Tănase, 2013: Forecasting the onset of cloud-to-ground lightning using radar and upper-air data in Romania. *International Journal of Climatology*, **33**, 1579-1584, https://doi.org/10.1002/joc.3533

Curran, E. B., R. L. Holle, and R. E. López, 2000: Lightning casualties and damages in the United States from 1959 to 1994. *Journal of Climate,* **13**, 3448-3464, https://doi.org/10.1175/1520-0442(2000)013%3C3448:LCADIT%3E2.0.CO;2

Dixon, M., and G. Wiener, 1993: TITAN: Thunderstorm identification, tracking, analysis, and nowcasting—A radar-based methodology. *Journal of Atmospheric and Oceanic Technology*, **10**, 785-797, https://doi.org/10.1175/1520-0426(1993)010%3c0785:TTITAA%3e2.0.CO;2

Elsom, D. M., and J. D. Webb, 2014: Deaths and injuries from lightning in the UK, 1988–2012. *Weather*, **69** 221–226, https://doi.org/10.1002/wea.2254

Fujibe, F., 2017: Long-term change in lightning mortality and its relation to annual thunder days in Japan. *Journal of Natural Disaster Science*, **38**, 17-29, https://doi.org/10.2328/jnds.38.17

Greene, D. R., and R. A. Clark, 1972: Vertically integrated liquid water—A new analysis tool. *Monthly Weather Review*, **100**, 548-552, https://doi.org/10.1175/1520-0493(1972)100%3c0548:VILWNA%3e2.3.CO;2

Gremillion, M. S., and R. E. Orville, 1999: Thunderstorm characteristics of cloud-to-ground lightning at the Kennedy Space Center, Florida: A study of lightning initiation signatures as indicated by the WSR-88D. *Weather and Forecasting*, **14**, 640-649, https://doi.org/10.1175/1520-0434(1999)014%3C0640:TCOCTG%3E2.0.CO;2

Hayenga, C. O., and J. W. Warwick, 1981: Two-dimensional interferometric positions of VHF lightning sources. *Journal of Geophysical Research: Oceans*, **86**, 7451-7462, https://doi.org/10.1029/JC086iC08p07451

Hyun, Y. K., S. K. Kar, K. J. Ha, and J. H. Lee, 2010: Diurnal and spatial variabilities of monsoonal CG lightning and precipitation and their association with the synoptic weather conditions over South Korea. *Theoretical and Applied Climatology*, **102**, 43-60, https://doi.org/10.1007/s00704-009-0235-5

Ishii, K., S. Hayashi, and F. Fujibe, 2014: Statistical analysis of temporal and spatial distributions of cloud-to-ground lightning in Japan from 2002 to 2008. *Journal of Atmospheric Electricity*, **34**, 79-86, https://doi.org/10.1541/jae.34.79

Kawasaki, Z. I., K. Yamamoto, K. Matsuura, P. Richard, T. Matsui, Y. Sonoi, and N. Shimokura, 1994: SAFIR operation and evaluation of it's performance. *Geophysical Research Letters*, **21**, 1133-1136. https://doi.org/10.1029/93GL02788

Kiany, M. S. K., R. C. Balling Jr, R. S. Cerveny, and D. S. Krahenbuhl, 2018: Diurnal variations in seasonal precipitation in Iran from TRMM measurements. *Advances in Space Research*, **62**, 2418-2430, https://doi.org/10.1016/j.asr.2018.07.003.

Kummerow, C., and Coauthors, 2000: The status of the tropical rainfall measuring mission (TRMM) after two years in orbit. *Journal of Applied Meteorology*, **39**, 1965–1968, https://doi.org/10.1175/1520-0450(2001)040%3C1965:TSOTTR%3E2.0.CO;2

Lang, T. J., and S. A. Rutledge, 2011: A framework for the statistical analysis of large radar and lightning datasets: results from STEPS 2000. *Monthly Weather Review,* **139**, 2536–2551, https://doi.org/10.1175/MWR-D-10-05000.1

Lang, T. J., and Coauthors, 2004: The severe thunderstorm electrification and precipitation study. *Bulletin of the American Meteorological Society,* **85**, 1107–1126, https://doi.org/10.1175/BAMS-85-8-1107

Liu, C., and E. J. Zipser, 2008: Diurnal cycles of precipitation, clouds, and lightning in the tropics from 9 years of TRMM observations. *Geophysical Research Letters,* **35**, L04819, https://doi.org/10.1029/2007GL032437

MacGorman D. R., and W. D. Rust, 1998. *The Electrical Nature of the Storms.* Oxford University Press, 422pp.

MacGorman D. R., D. W. Burgess, V. Mazur, W. D. Rust, W. L. Taylor, and B. C. Johnson, 1989: Lightning rates relative to tornadic storm evolution on 22 May 1981. *Journal of the Atmospheric Sciences,* **46**, 221–251, https://doi.org/10.1175/1520-0469(1989)046%3c0221:LRRTTS%3e2.0.CO;2

MacGorman, D. R., I. R. Apostolakopoulos, N. R. Lund, N. W. Demetriades, M. J. Murphy, and P. R. Krehbiel, 2011: The timing of cloud-to-ground lightning relative to total lightning activity. *Monthly Weather Review*, **139**, 3871–3886. https://doi.org/10.1175/MWR-D-11-00047.1

Michimoto, K., 1991: A study of radar echoes and their relation to lightning discharge of thunderclouds in the Hokuriku district. Part I: Observations and analysis of thunderclouds in summer and winter. *Journal of the Meteorological Society of Japan*, **69**, 327–335, https://doi.org/10.2151/jmsj1965.69.3_327

Mills, B., D. Unrau, L. Pentelow, and K. Spring, 2010: Assessment of lightning-related damage and disruption in Canada. *Natural Hazards,* **52**:481–499 https://doi.org/10.1007/s11069-009-9391-2

Mosier, R. M., C. Schumacher, R. E. Orville, and L. D. Carey, 2011: Radar nowcasting of cloud-to-ground lightning over Houston, Texas. *Weather and Forecasting*, **26**, 199–212, https://doi.org/10.1175/2010WAF2222431.1

Ohno, H., 2001: *Thunderstorm and meso-meteorology*. Tokyodo Shuppan Co., Ltd., 309pp. (in Japanese)

Rowe, A. K., S. A. Rutledge, and T. J. Lang, 2011: Investigation of microphysical processes occurring in isolated convection during NAME. *Monthly Weather Review*, **139**, 424–443, https://doi.org/10.1175/2010MWR3494.1

Roy, S. S., and R. C. Balling Jr, 2013a: Diurnal variations in summertime lightning activity in Tropical Asia. *International Journal of Climatology*, **33**, 1830–1836, https://doi.org/10.1002/joc.3658

Roy, S. S., and R. C. Balling Jr, 2013b: Spatial patterns of diurnal variations in summer-season lightning activity across the tropical and subtropical regions of the Northern Hemispheric Americas. *Meteorology and Atmospheric Physics*, **121**, 199–206, https://doi.org/10.1007/s00703-013-0259-3

Saunders, C. P. R., S. L. Peck, 1998: Laboratory studies of the influence of the rime accretion rate on charge transfer during crystal/graupel collisions. *Journal of Geophysical Research: Atmospheres,* **103**, 13949–13956. https://doi.org/10.1029/97JD02644

Shafer, M. A., D. R. MacGorman, and F. H. Carr, 2000: Cloud-to-ground lightning throughout the lifetime of a severe storm system in Oklahoma. *Monthly Weather Review*, **128**, 1798–1816, https://doi.org/10.1175/1520-0493(2000)128%3c1798:CTGLTT%3e2.0.CO;2

Takahashi, T., 1978: Riming electrification as a charge generation mechanism in thunderstorms. *Journal of the Atmospheric Sciences*, **35**, 1536–1548, https://doi.org/10.1175/1520-0469(1978)035<1536:REAACG>2.0.CO;2

Vincent, B. R., L. D. Carey, D. Schneider, K. Keeter, and R. Gonski, 2005: Using WSR-88D reflectivity for the prediction of cloud-to-ground lightning: a central North Carolina study. *Conference on Meteorological Applications of Lightning Data*, San Diego, CA, American Meteorological Society, 3.2, https://ams.confex.com/ams/Annual2005/techprogram/paper_84669.htm

Watson, A. I., R. L. Holle, and R. E. López, 1995: Lightning from two national detection networks related to vertically integrated liquid and echo-top information from WSR-88D Radar. *Weather and Forecasting,* **10**, 592–605, https://doi.org/10.1175/1520-0434(1995)010%3c0592:LFTNDN%3e2.0.CO;2

Wilks, D. S., 2011: *Statistical methods in the atmospheric sciences, 3rd edition*. Academic press, 676pp.

Xu, W., and E. J. Zipser, 2011: Diurnal variations of precipitation, deep convection, and lightning over and east of the eastern Tibetan Plateau. *Journal of Climate*, **24**, 448–465, https://doi.org/10.1175/2010JCLI3719.1

Yang, Y. H., and P. King, 2010: Investigating the potential of using radar echo reflectivity to nowcast cloud-to-ground lightning initiation over southern Ontario. *Weather and Forecasting*, **25**, 1235–1248, https://doi.org/10.1175/2010WAF2222387.1

Yoshida, S, T. Adachi, K. Kusunoki, S. Hayashi, T. Wu, T. Ushio, and E. Yoshikawa, 2017: Relationship between thunderstorm electrification and storm kinetics revealed by phased array weather radar. *Journal of Geophysical Research: Atmospheres*, **122**, 3821–3836, https://doi.org/10.1002/2016JD025947

Yoshida, S, E. Yoshikawa, T. Adachi, K. Kusunoki, S. Hayashi, and H. Inoue, 2018: Three-dimensional radio images of winter lightning in japan and characteristics of associated charge structure. *IEEJ Transactions on Electrical and Electronic Engineering*, **14**, 175–184, https://doi.org/10.1002/tee.22795

Yuan, W, R. Yu, M. Zhang, W. Lin, H. Chen, and J. Li, 2012: Regimes of diurnal variation of summer rainfall over subtropical East Asia. *Journal of Climate*, **25**, 3307–3320, https://doi.org/10.1175/JCLI-D-11-00288.1

Chapter 4
The relationship between lightning flash rate and ice-related volume derived from dual-polarization radar

4.1 Introduction

As mentioned in Chapter 1, lightning strikes can be a serious risk to the safe operation of aircrafts. Therefore, the JMA operates the Doppler radar for airport weather (DRAW) network at the major Japanese international airports to reduce the aircraft damage, ground staff injuries, and operation delay caused by lightning strikes, gusts, or downbursts (Tsukamoto et al. 2016). Since 2016, the JMA has begun installing dual-polarization Doppler radars in Japan. One of the reasons for this update is to improve the accuracy of the lightning predictions. Microphysical particle information can be obtained via dual-polarization radar observation (Hall et al. 1984; Aydin et al. 1986; Vivekanandan et al. 1999), and it is well known that lightning initiation and the microphysical particle distribution within a thunderstorm are closely related (Takahashi 1984; Ziegler and MacGorman 1994; Carey and Rutledge 1996). Therefore, it is crucial to clarify the relationship between cloud electrification and radar-derived properties and to subsequently improve the prediction performance in terms of the initiation and cessation of lightning activity.

It is widely accepted that the interaction between the graupel and the ice particles in thunderstorms plays an important role in the electrical charge separation within the mixed-phase region (0 °C to −40 °C), which includes the supercooled cloud water droplets from the non-inductive charging mechanism (NIC) (Takahashi 1978; Saunders and Peck 1998). In view of the NIC, the charge distribution in a thunderstorm has a bipolar or tripolar structure due to the differences in charge polarity, which depends on the temperature and the droplet terminal fall velocity of each ice particle type (Takahashi 1984; Ziegler and MacGorman 1994). Around the updraft core, which is the main charging region, it has been observed that the charge-carrying microphysical particles have a complex distribution, which makes it difficult to understand the relationship between the microphysical particles and the cloud electrification in thunderstorms (Stolzenburg and Marshall 1998; Bruning et al. 2007). In Chapter 3 using single polarimetric radar,

it is demonstrated that the presence of strong radar reflectivity (e.g., 30 dBZ, 35 dBZ or 40 dBZ) in the mixed-phase region is a good indicator of lightning discharge (e.g., Dye et al. 1989; Gremillion and Orville 1999; Shafer et al. 2000; Vincent et al. 2005; Mosier et al. 2011; Seroka et al. 2012). Here, the assumption is that the strong radar reflectivity existing in the mixed-phase region is a proxy for graupel, and that it could be used as a good lightning index indirectly based on the theory of NIC.

Recently, dual-polarization radar has been adopted for both research and operational purposes, largely because it has a high sensitivity to the shape and size of the microphysical particles in a mixed-phase region that are important for cloud electrification (Krehbiel et al. 1996; Carey and Rutledge 2000). Using dual-polarization radar with the hydrometeor classification algorithm (HCA) makes it possible to deduce the microphysical particle type in any given thunderstorm. Obtaining information related to the ice hydrometeor particles and their distribution within a thunderstorm is crucial for understanding the thunderstorm electrification and lightning production based on the NIC (Ziegler et al. 1991; López and Aubagnac 1997). The observation of the distribution of microphysical particles within a thunderstorm via dual-polarization radar allows for directly comparing the microphysical properties in relation to the lightning activity. The cloud kinematic parameters (e.g., updraft volume, maximum updraft velocity) and the microphysical parameters (e.g., graupel volume, graupel mass, 35 dBZ volume) can be obtained using dual-polarization radar with HCA and updraft analysis via multiple Doppler radars. A number of case studies related to the relationship between cloud parameters and lightning flash activity have been conducted (e.g., Carey and Rutledge 2000; Deierling and Petersen 2008; Lund et al. 2009; Akita et al. 2011; Calhoun et al. 2013; Basarab et al. 2015; Mecikalski et al. 2015; Stolzenburg et al. 2015; van Lier-Walqui et al. 2016; Wang et al. 2016). Here, Carey and Rutledge (2000) investigated cloud electrification and the correlation between lightning flash rate and the hydrometeors' horizontal and vertical structure within a tropical convection using a dual-polarization radar and a two-dimensional lightning location system for one multi-cell storm case in Australia. The results showed there was a high correlation between the retrieved graupel mass and cloud-to-ground lightning (CG). Meanwhile, Mecikalski et al. (2015) conducted a case study of a thunderstorm using the three-dimensional lightning discharge observation system (lightning

mapping array (LMA), Rison et al. 1999) and dual-polarization radar observation for a single thunderstorm that occurred in Alabama, the USA on 21 May 2012. Here, it was found that graupel volume and graupel mass had a higher correlation with total lightning (TTL, the summation of CG and intra-cloud lightning (IC)) flash rate than with the updraft parameters. Elsewhere, Stolzenburg et al. (2015) compared the LMA data for New Mexico with the ground electric field measurement, dual-polarization parameters, and radiosonde data in terms of three cases from the summer of 1999. The results showed that the initial lightning discharge started above the precipitation core in the thunderstorm and that prolate graupel particles existed below the discharge initiation point.

A number of statistical studies involving numerous thunderstorm observations have been conducted based on the relationships obtained in previous case studies. Among them, Deierling and Petersen (2008) investigated the relationship between thunderstorm properties and lightning discharge using LMA, dual-polarization radar and dual Doppler radar for 11 cases in Northern Alabama. Here, they found that an updraft volume of greater than 5 m s^{-1} had a high linear correlation (Pearson correlation coefficient, $r = 0.93$) with the flash rate of TTL. Deierling et al. (2008) demonstrated that the relationship between precipitating ice mass flux and TTL had a high correlation ($r = 0.85$) in the same 11 cases. Elsewhere, Basarab et al. (2015) compared and verified flash rates through the LMA and thunderstorm properties obtained via radar, including graupel volume, mixed-phase 35dBZ volume (VOL35), and ice mass flux, for 11 cases in Colorado. The results indicated that the VOL35 demonstrated the best correlation. Carey et al. (2019) subsequently increased the number of sample cases to 33 to perform a similar analysis in Alabama, where it was found that graupel volume had the best correlation. Here, the error was found to be smaller for the microphysical parameters than for the kinematic parameters, especially at the low flash rate regime.

Although many of these statistical analysis studies adopted a similar method, different lightning indices were found to be the best, while the linear regression slope also varied. In terms of the use of HCA in previous studies, only graupel and hail based on NIC were considered, while ice particles (including cloud ice and snow), which are also important to NIC theory, were largely ignored. While Deierling et al. (2008) did note the importance of non-precipitating ice mass

within a certain range of the subfreezing temperature regions within thunderstorms, advanced research that combines radar reflectivity and hydrometeor information has yet to be carried out. In the previous studies, the radar reflectivity considering the temperature at the altitude is used as the lightning index. The radar reflectivity consists of all liquid and solid water substances. Since the ice phase particles are more important for lightning initiation based on NIC than liquid precipitation particles, it is possible to obtain a better relation between radar parameters and lightning if liquid water can be removed. In view of these points, it is necessary to investigate a better lightning index that combines radar reflectivity volume and HCA, including in terms of ice and snow particles. In addition, as Bovalo et al. (2019) noted, the previous studies described above tended to target the same geographical location (mid- and south-USA) and lacked generalization in terms of thunderstorm type.

The next-generation Geostationary Operational Environmental Satellite R series (GOES-R) is equipped with a geostationary lightning mapper (GLM), which enables wide-area real-time observation (Goodman et al. 2013). The knowledge of lightning indicators on a global scale is useful for the research on climate change and the data assimilation of global and regional models. Therefore, it is crucial to investigate lightning indicators in different geographical and atmospheric environment fields.

The purpose of this chapter is to clarify the relationship between microphysical properties and lightning flash rate, especially in terms of the effect of ice-related particles, and to demonstrate the value of the microphysical properties derived from the dual-polarization radar parameters as a lightning index. To this end, the relationship between the C-band operational dual-polarization data and the lightning flash rate is investigated. In the process, the author analyzes 10 cases of multi-cell thunderstorms in different regions to those involved in the previous studies, including in terms of lightning initiation to cessation. Section 4.2 describes the data and the analysis method, while Sec. 4.3 introduces the analysis of one case (Sec. 4.3.1), and addresses the relationship between microphysical properties and lightning flash rate using 10 cases (Sec. 4.3.2, 4.3.3, 4.3.4 and 4.3.5). Finally, the author summarizes the results in Sec. 4.4.

4.2 Data and method

4.2.1 Dual-polarization radar data

The JMA has installed a number of airport weather Doppler radar (DRAW) systems to monitor severe weather around the airports (Tsukamoto et al. 2016), with Narita Airport's DRAW updated in 2016 as a dual-polarization radar (hereafter NRT-DP-DRAW, Fig. 4.1). The NRT-DP-DRAW uses a 5.3 GHz C-band, and the detection range is 120 km, the range resolution 150 m, and the beam width 0.7 degrees, while the volume scan is every 5 min (Table 4.1). In this chapter, the author used 11 plan position indicator (PPI) scan data every 5 min from the volume scan data, excluding the zenith observation and the overlapping minimum elevation observations.

Table 4.1 Hardware specifications and observation pattern of dual-polarization radar for airport weather at Narita Airport

	Specifications
Frequency	5.3 GHz (C-band)
Beam width	0.7 degree
Antenna rotation rate	4 rpm
Range	120 km radius
Range resolution	150 m
Volume scan	16 PPI, every 5 min.
Elevations	0.7 (5 times), 1.1, 1.5, 2.1, 2.8, 3.8, 5.1, 6.9, 9.2, 12.5, 17.0, 90.0 (not used in this study)
Polarization	dual-polarization

4.2.2 Lightning location data

In this chapter, LIDEN was also used for the lightning location data as in Chapter 3 (see Sec. 3.2.2). According to Ishii et al. (2014), the Kanto Plain, where the NRT-DP-DRAW is located, is the most active area of CG lightning activity in Japan during the summer period (Fig. 1.3b).

4.2.3 Atmospheric sounding data

The sounding data of the Tateno station (36.056°N, 140.125°E) operated by the JMA is used as the representative temperature for the thunderstorms (Fig. 4.1(a)). Observations are made twice a day at 00:00 and 12:00 UTC (UTC = Japan Standard Time − 9 hour), and the sounding data close to before the initiation of a thunderstorm are used in this study. From this observation data, the condition of the atmospheric environment (CAPE = convective available potential energy, LCL = lifting condensation level, LFC = level of free convection, EL = equilibrium level) was obtained for each case.

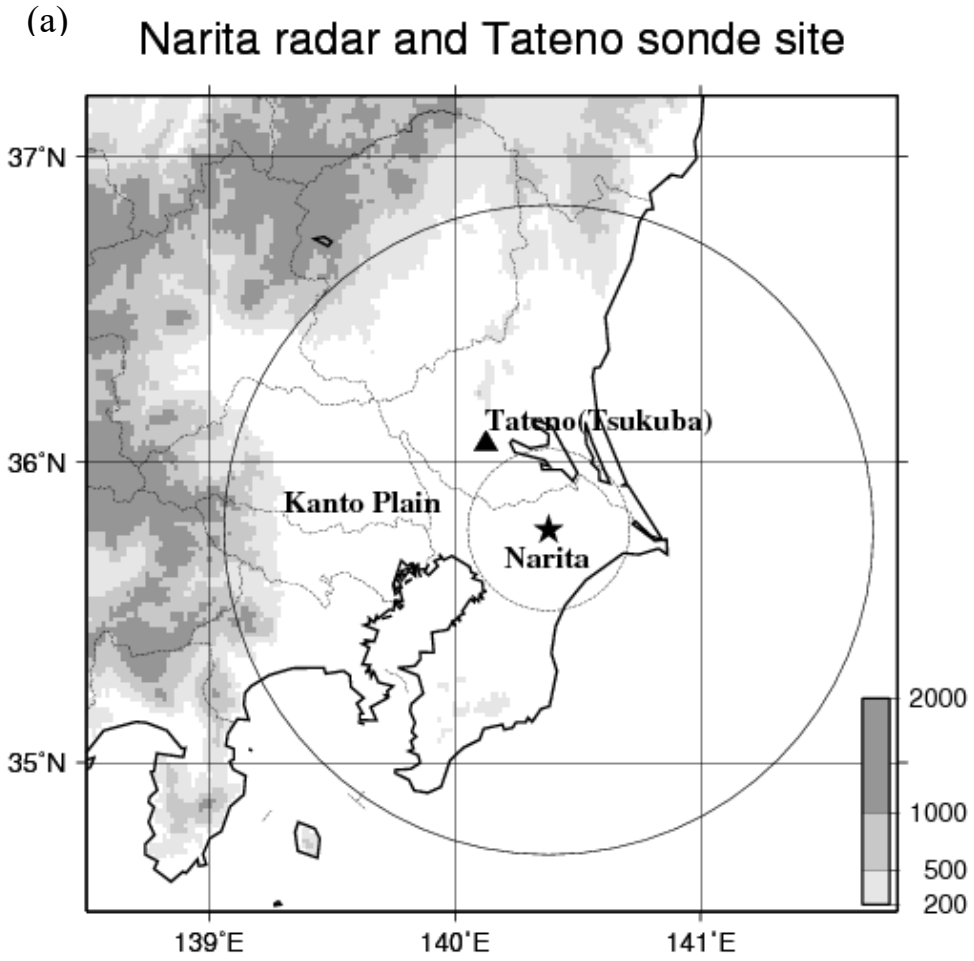

Figure 4.1 (a) Map of the Kanto Plain with topography. The location of the NRT-DP-DRAW (black star) with 30 and 120 km black circles. The black triangle is the Tateno radiosonde site. (b) NRT-DP-DRAW site (from Narita Aviation Weather Service Center)

(b)

Figure 4.1 (continued)

4.2.4 Hydrometeor classification algorithm (HCA)

To identify the microphysical properties in the thunderstorms, an HCA developed by Umehara et al. (2019) for operational purposes was applied to the NRT-DP-DRAW (details in Sec. 2.3). The HCA was implemented with NRT-DP-DRAW observations of reflectivity at horizontal polarization (Z_{hh}), differential reflectivity (Z_{DR}), copolar correlation coefficient (ρ_{hv}), specific differential phase (K_{DP}), S (differential phase between copolar received signals (Ψ_{DP})), $S(Z_{DR})$ and $S(\rho_{hv})$, (here the function $S(X)$ represents the median absolute deviation of X) and environmental temperature profiles as inputs. The temperature data were obtained via the JMA meso-scale analysis (Honda et al. 2005) and the melting layer detection algorithm with specific dual-polarization variables.

4.2.5 Target cases and analysis methods

The author manually selected a case in which an isolated thunderstorm with CG and IC was observed within the observation range of the NRT-DP-DRAW for its entire life cycle from initiation to cessation. Any thunderstorm moving out of radar or intruding from outside of the range during its life cycle was not selected. Ten cases from the summers of 2017 and 2018 were selected. The tracking from the thunderstorm initiation to cessation was conducted manually, and the selected thunderstorm was separated from the other thunderstorms and their attendant lightning flash activity. A total of 351 volume scans from the 10 cases were used from the NRT-DP-DRAW data (Table 4.2). The total CG for each thunderstorm lifecycle varied widely from 35 to 1536 flashes, while the maximum flash rate in each case was also widely distributed from 5 [five min^{-1}] to 190 flashes [five min^{-1}]. The magnitude of CAPE and the total CG were not correlated. The LFC and EL also varied greatly from case to case and were unrelated to the total CG. Meanwhile, the LCL ranged from 860 to 960 hPa, with the common feature that the lower atmosphere was moist and the cloud base was at low altitude. It should be noted that no distinction was made between the smallest separable radar echo cells in any thunderstorm used in this study. In fact, the objective of this study was to track the entire lifecycle of a thunderstorm consisting of multi-cells from initiation to cessation and it is difficult to distinguish a small echo cell in a multi-cell thunderstorm with lightning activity, largely because the lightning propagation between the

small cells is observed in a multi-cell thunderstorm (Mecikalski et al. 2015). In this study, only the “isolated thunderstorm”, which was distinguished from the other thunderstorms, was selected.

The HCA outlined in Sec. 4.2.4 was applied to the 10 target cases, and the volume of microphysical particles contained in the thunderstorm was integrated. The following microphysical parameters were used for comparison with the lightning flash rate. First, graupel volume (GV) was used, which, as Deierling and Petersen (2008) noted, is undoubtedly correlated with lightning activity. Second, the total volume of graupel or hail (GHV), and the total of all ice-related particle volumes (ALICV, including cloud ice, snow, graupel and hail) were also used. ALICV was subsequently converted to ALICMS (ice mass of ALICV) using the conversion equation devised by Carey and Rutledge (2000), while GHV was converted to GHMS (ice mass of graupel or hail). In addition, radar reflectivity volumes of greater than 35 dBZ and 40 dBZ above freezing level, which have been used as the lightning indicator in previous research (e.g., Zipser and Lutz 1994; Liu et al. 2012; Basarab et al. 2015), were used and denoted as V35F and V40F, respectively. As noted in Sec. 1, since the presence of ice particles is strongly related to NIC and thunderstorm electrification, the author also used V35IC, V40IC, which are volumes greater than 35 dBZ and 40 dBZ, and classified as an ice-related grid deduced from the HCA, respectively. The author compared and verified the relationship between these microphysical properties retrieved via dual-polarization radar and lightning flash rate.

Table 4.2 Summary of thunderstorms: duration, number of radar observations, number of lightning, lightning flash rate, and atmospheric conditions from radiosonde sounding.

Case	Date	start time	end time	number of scans	CG	CG+	IC	Positive CG ratio [%]	Max. CG Rate [/ 5 min.]	CAPE [J/kg]	LCL [hPa]	LFC [hPa]	EL [hPa]
1	2017-08-18	1400	1640	33	40	7	110	18	8	1016	957	872	205
2	2017-08-22	0830	1100	31	1427	169	3537	12	190	546	950	657	224
3	2017-09-25	0830	1320	59	1316	134	3878	10	52	183	922	792	340
4	2018-07-11	1040	1640	73	1536	99	3306	6	57	31	915	703	386
5	2018-07-22	1400	1530	19	120	37	149	31	32	1250	875	793	141
6	2018-08-03	0900	1100	25	169	16	399	9	27	-	866	-	-
7	2018-08-10	0540	0720	20	41	2	55	5	7	678	916	785	184
8	2018-08-11	0440	0700	29	105	46	832	44	34	42	917	561	311
9	2018-08-26	0900	1020	17	155	6	163	4	25	490	895	672	231
10	2018-09-17	0840	1220	45	125	19	812	15	14	-	919	-	-
Sum.				351	5034	535	13241						

4.3 Results

In Sec. 4.3.1, a single thunderstorm is analyzed to demonstrate the correlations between lightning and the microphysical properties derived via dual-polarization radar data. The linear relationships between lightning flash rate and the radar-derived microphysical properties are then identified from the whole 10-case dataset in Sec. 4.3.2. For the microphysical parameters that demonstrated a high correlation, the author evaluates the attendant linear relationships and errors in Sec. 4.3.3. The relationship between lightning flash type and the vertical distribution of the microphysical parameters is investigated in Sec. 4.3.4. To examine the usefulness of proposed indices for lightning nowcasting, the time-lag correlations are calculated in Sec. 4.3.5. Finally, the author examines in what environment these proposed lightning indices can be applied.

4.3.1 Example of lightning and microphysical properties on 25 September 2017

The CG and CGp (positive polarity CG) distributions and the accumulated precipitation in 6 h obtained via the JMA-RA (JMA radar/rain-gauge-analyzed precipitation, Makihara et al. 1996) on 25 September 2017 (Case 3 in Table 4.2) are shown in Fig. 4.2(a). This multi-cell storm with heavy precipitation occurred at 08:30 UTC (17:30 local time) on the north side of the radar observation area, before it developed with a southward movement and finally disappeared at 13:20 UTC. The maximum size of the thunderstorm was 50 km in the east-west and 70 km in the north-south. The maximum accumulated rainfall for 6 h according to the JMA-RA was 89 mm, and the hourly maximum rainfall recorded by the rain-gauge was 46 mm h^{-1}. The total number of CG instances during the lifecycle was 1316, while the number for IC was 3878, and for TTL 5194. These were the largest values among the 10 cases investigated in this study. The time-height cross-section of the V35IC distribution within the thunderstorm, as derived from the NRT-DP-DRAW, is shown in Fig. 4.2(b), while the time-series of the flash rate for CG, IC, and CGp is also depicted. The CG and IC activity both started and ended at the same time. When this activity started, the V35IC regions of over 30 km^3 were simultaneously colder than 0 °C and were widely distributed from 3 to 8 km altitude in the thunderstorm during the mature period of 09:00 to 11:40 UTC. This larger V35IC region coincided with the 0 °C to −30 °C range, which is important for thunderstorm

electrification in NIC theory. The presence of a large number of ice-related particles in this region was consistent with the large lightning flash rate in NIC theory. Both the IC and the CG flash rates decreased from their peak at 11:40 UTC to their cessation at 13:00 UTC. At the same time, the height of greater than 20 km^3 of V35IC simultaneously decreased from 9 km to 4 km in altitude, and the maximum value of V35IC also decreased from 100 km^3 to 20 km^3. These results suggest that the decrease in V35IC and lightning flash rate were synchronized. CGp was mostly observed during the period between 10:00 UTC and 10:50 UTC when the V35IC of over 20 km^3 in height reached the highest point in the lifecycle but was barely observed during other periods. Using time-series multi-cell storm data, the author could obtain the relationship between flash rate and the accumulated V35IC, and could create a linear regression equation for each lightning flash type (Fig. 4.2(c)–(f)). The V35IC showed a high correlation with CG (Pearson correlation coefficient, r = 0.82), and a slightly lower correlation with TTL (r = 0.74) and IC (r = 0.70), while CGp showed the lowest correlation (r = 0.47) with no clear relationship. Regardless of the relatively high correlation between V35IC and flash rate, except for CGp, the large V35IC of over 500 km^3 displayed a great dispersion.

4.3.2 Overview of the correlations between lightning and microphysical properties

As show in Table 4.2, HCA was applied to all 10 cases to calculate the microphysical and radar properties, the flash rate for each lightning type (CG, IC, CGp, total), and the linear correlation coefficient (r) (Fig. 4.3(a)–(d)). In terms of CG flash rate, GV, GHV, V35IC, V40IC, and GHMS demonstrated high correlations (r > 0.55) in all cases. For the correlation coefficient of the CG flash rate in relation to GHV, the maximum was 0.97 and the minimum 0.58 in all cases (Fig. 4.3(a)). The relationship between microphysical properties and IC was similar to that of CG, but the difference in the correlation coefficient among all the cases decreased (Fig. 4.3(b)). In terms of the relationship between CGp and the microphysical properties, the correlation coefficients for all the microphysical properties were lower than those for CG (Fig. 4.3(c)). Only in Case 2 did the relationship with CGp show a high correlation (r > 0.7) in terms of any index. The TTL relationship revealed similar results to those for the CG and IC relationships (Fig. 4.3(d)).

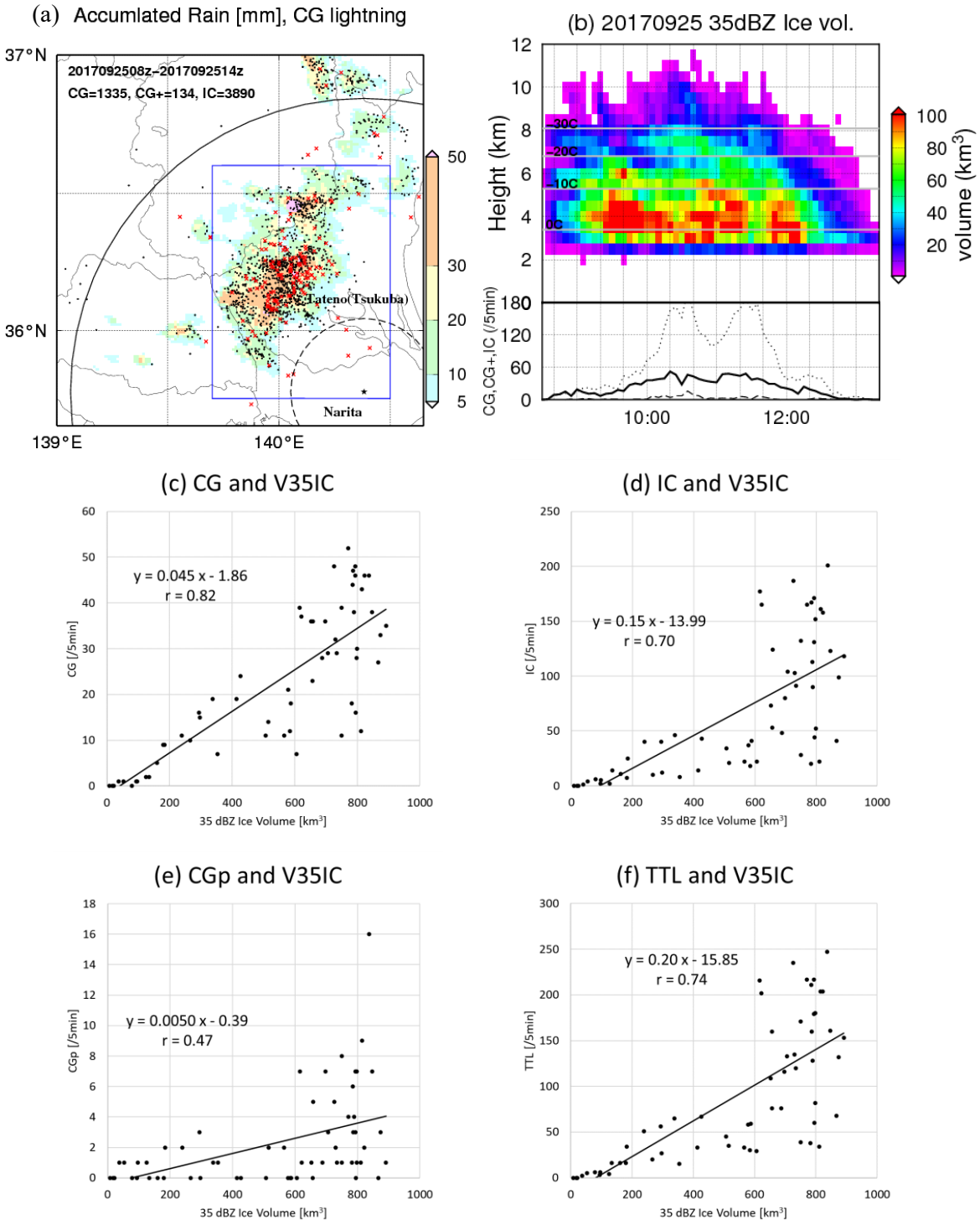

Figure 4.2 Case3, 25 September 2017: (a) accumulated precipitation (color shade), CG (black dot) and CGp (red cross); (b) time-height cross-section of V35IC with time-series of the flash rate line of CG (solid), IC (dotted), and CGp (dashed) every 5 min with isotherm from 0 to −30 °C (gray line); (c) scatter plots and liner regression of V35IC vs. CG, (d) IC (e) CGp, and (f) TTL.

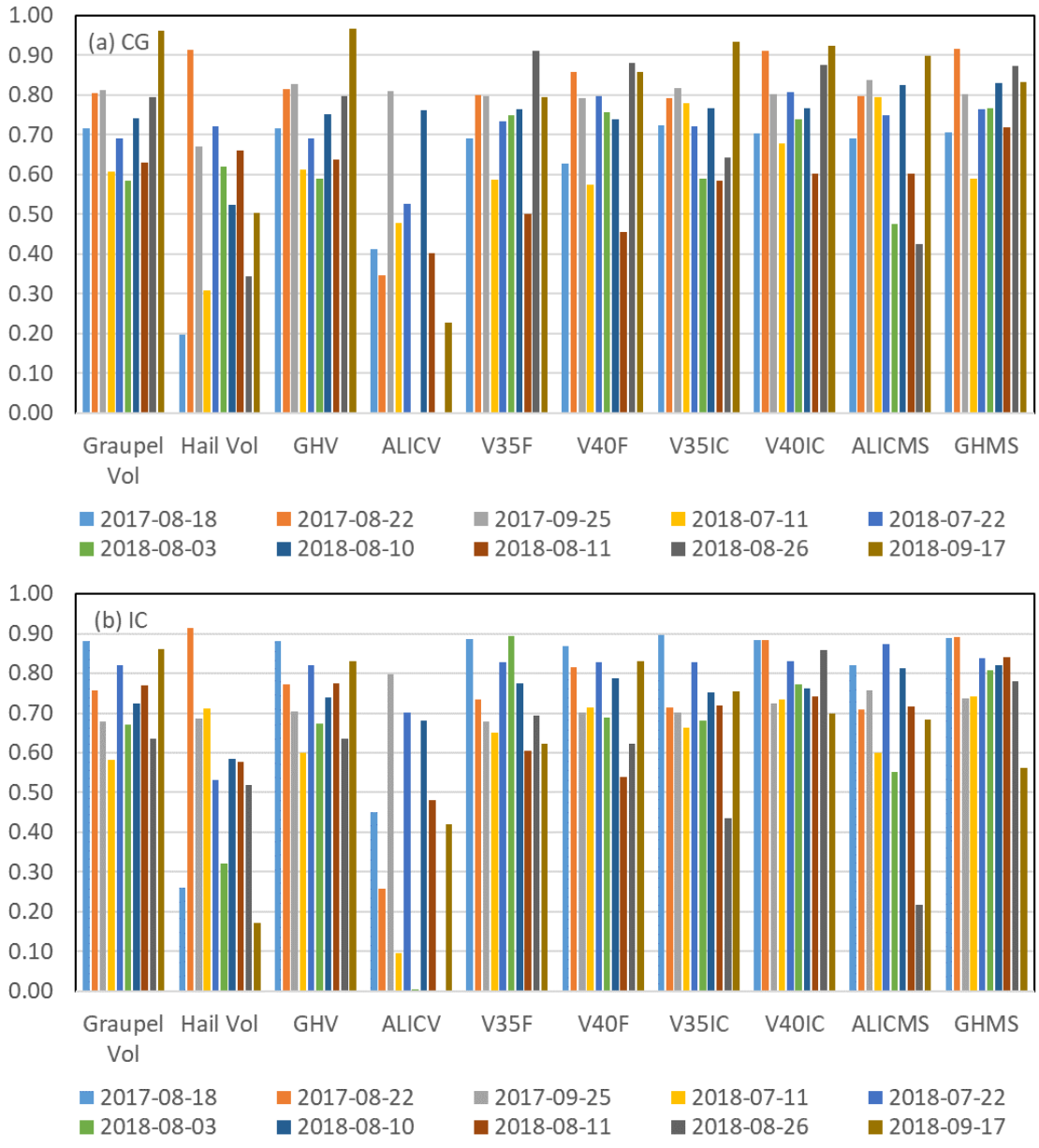

Figure 4.3 Bar plots of the correlation coefficients in each case for graupel vol., hail vol., GHV, V35F, V40F, V35IC, V40IC, ALICMS, and GHMS, (a) CG, (b) IC, (c) CGp, and (d) TTL.

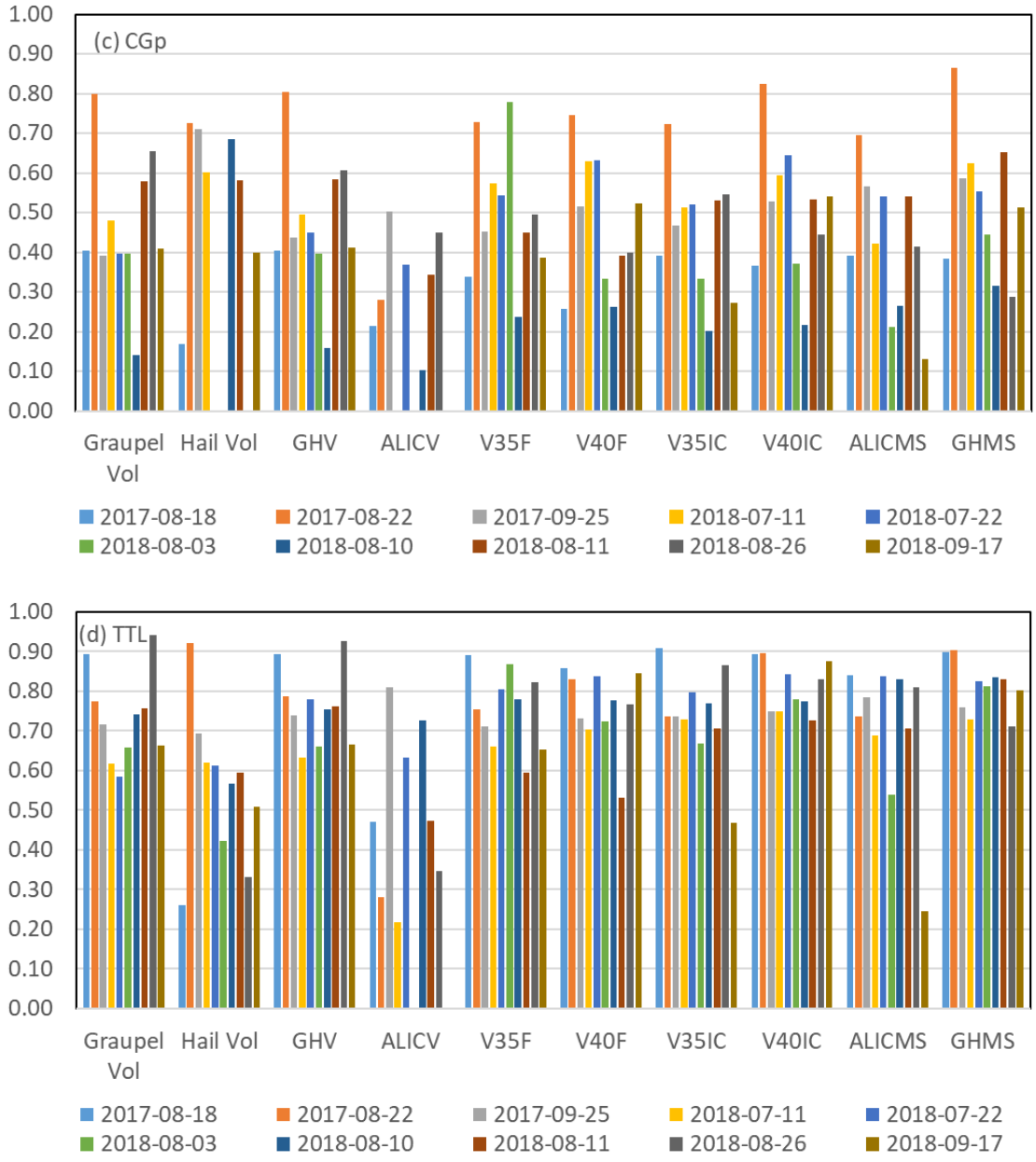

Figure 4.3 (continued)

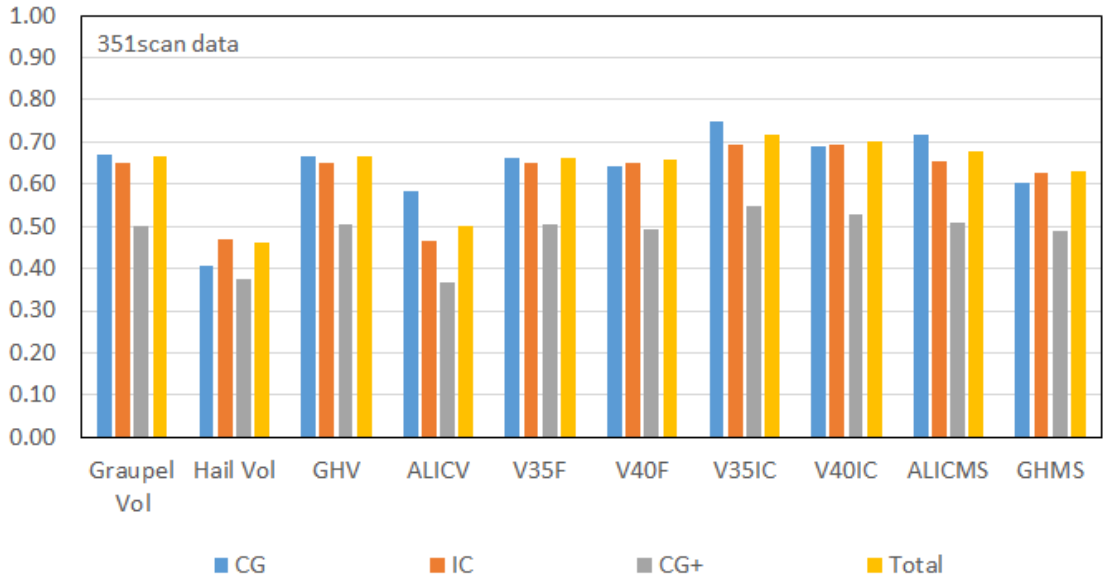

Figure 4.4 Bar plots of correlation coefficients for 351 scans of all 10 cases in terms of each lightning flash type.

The correlation coefficient was calculated using all the 351 volume scan data for the 10 cases (Fig. 4.4). For the volumes using only particle information from HCA, GV and GHV showed the best correlations for all lightning flash types. The correlation coefficient between the volume of all particle types and all discharge types was smaller than that for both GV and GHV (not shown). In the volumes using radar reflectivity, V35IC and V40IC, which involved the addition of ice-related particle information, showed a higher correlation coefficient than with V35F and V40F, which only involved the temperature. Both Liu et al. (2012) and Basarab et al. (2015) introduced a mixed-phased volume of radar reflectivity greater than 35 dBZ (VOL35) and demonstrated a high correlation between VOL35 and TTL activity. The difference between the VOL35 to the V35IC used in this study is that the latter excluded any locations where rain and rain-related were classified as the dominant hydrometeor type. As a result, a better correlation was obtained than with the radar reflectivity volume with temperature only. Taking Case 3 as an example, the volumes of greater than 35 dBZ existed at less than 0 °C with large amounts of greater than 100 km^3 (Fig. 4.5(a)), while part of VOL35, from 20 to 80 km^3, was due to raindrops or rain-related droplets (Fig. 4.5(b)). This suggests that removing raindrops or rain-related

droplets from radar reflectivity volumes, which are not part of NIC theory, are important for obtaining a better relationship between lightning activity and the microphysical properties.

While Deierling et al. (2005) noted the limited contribution of non-precipitating ice to the lightning activity of thunderstorms, in this study, the effect of considering all ice-related particles is more clearly shown. Here, ALICMS shows a higher correlation than ALICV. Because the volume of the weak radar reflectivity was converted to a small mass, while the strong radar reflectivity was converted to a large mass, it can be assumed that the result is similar to that of V35IC using strong radar reflectivity. However, the reason why the correlation of GHMS was slightly lower than that of GHV is not clear, while it is possible that the influence of the differences in radar reflectivity was small because almost all graupel or hail grids have strong radar reflectivity, meaning the uncertainty related to mass conversion becomes stronger.

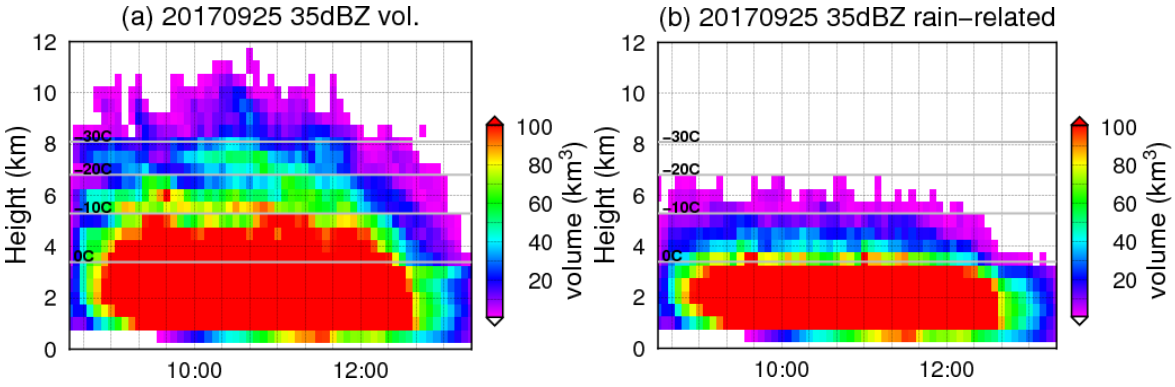

Figure 4.5 Same as Fig. 4.2(b), except for (a) 35dBZ vol., (b) 35dBZ vol. with rain/rain-related particle only

4.3.3 Linear relationships and errors

As shown in the previous section, GHV, V35IC, and ALIMS show stronger correlations with flash rate than the other microphysical properties (Fig. 4.4). From here, detailed investigations related to linear correlations and errors are conducted, especially for these three indicators. The scatterplots representing lightning flash rate in 5 min versus radar parameter for 10 cases are shown in Fig. 4.6, while the linear correlation equation and the errors are presented in Table 4.3. The scatterplot for lightning flash rate and the radar-derived microphysical parameters for all 10 cases was much larger spread than that for the case on 25 September 2017 (Figs. 4.2(c)–(f)).

In terms of GHV, the NRMSE was 9.4% for CG, and 8.5% for IC and TTL, while the scatterplot was small spread with high correlations except for CGp (Figs. 4.6(a), (d), (g), (j)). The linear regression equation slope was smallest with a CGp of 0.0076 and largest with a TTL of 0.27 (Table 4.3). Basarab et al. (2015) investigated the relationship between graupel echo volume (GEV, similar to GHV) and total lightning flash rate (the same as TTL) via LMA and found that the linear regression slope for GEV and TTL was 0.070 and that the NRMSE was 13.6%. Since the lightning flash rate unit used here was per 1 min, the regression equation slope was 0.35 when the unit was per 5 min, as was the case in this study, where the slope was close to 0.27. Meanwhile, the regression equation slope of GV and LMA flash rate (min^{-1}) identified by Carey et al. (2019) was 0.055, which is almost equal to the figure found in this study when the same unit was incorporated. The NRMSE in Carey et al.'s study was 13.1%, meaning the NRMSE of GHV for TTL here was smaller than that found by both Basarab et al. (2015) and Carey et al. (2019). The lack of negative bias in the high flash rate region pointed out by Basarab et al. (2015) may be the cause of the small NRMSE (Fig. 4.6(j)).

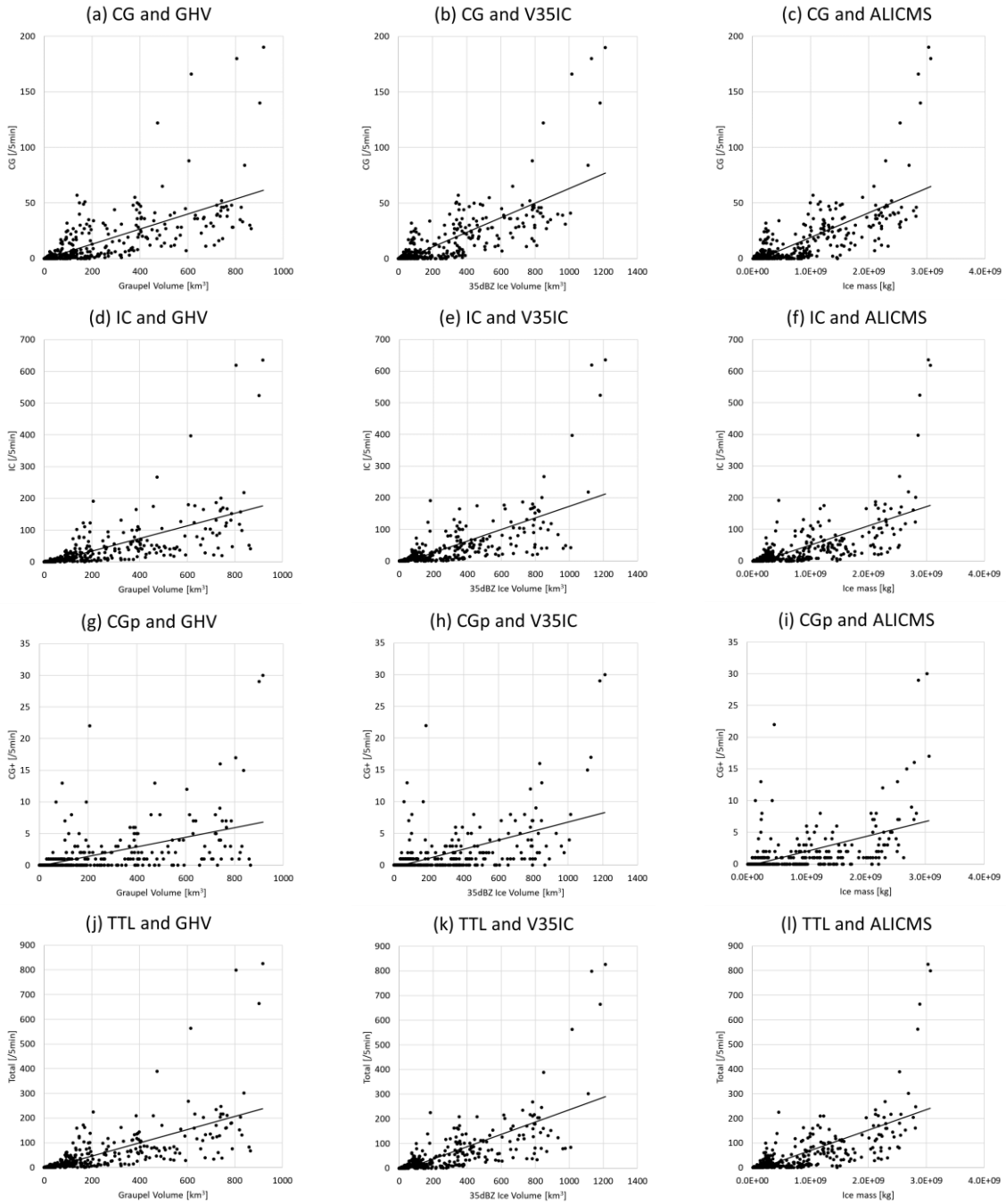

Figure 4.6 Same as Fig. 4.2(c), scatter plots (dot) and liner regression (black line), except for the flash type vs. radar properties for all 10 thunderstorms.

(a) CG vs. GHV, (b) CG vs. V35IC, (c) CG vs. ALICMS,

(d) IC vs. GHV, (e) IC vs. V35IC, (f) IC vs. ALICMS,

(g) CGp vs. GHV, (h) CGp vs. V35IC, (i) CGp vs. ALICMS,

(j) TTL vs. GHV, (k) TTL vs. V35IC, (l) TTL vs. ALICMS.

Table 4.3 Summary of linear equation and errors.

GHV	Linear regression equation	Correlation coefficient	RMSE [flash / 5min]	NRMSE [%]
CG	$0.068 \times GHV - 0.53$	0.67	17.8	9.4
IC	$0.20 \times GHV - 6.05$	0.65	54.2	8.5
CGp	$0.0076 \times GHV - 0.14$	0.50	3.0	10.1
TTL	$0.27 \times GHV - 6.58$	0.67	70.1	8.5

V35IC	Linear regression equation	Correlation coefficient	RMSE [flash / 5min]	NRMSE [%]
CG	$0.066 \times V35IC - 2.66$	0.75	15.8	8.3
IC	$0.18 \times V35IC - 9.61$	0.69	51.6	8.1
CGp	$0.0071 \times V35IC - 0.31$	0.55	2.9	9.8
TTL	$0.25 \times V35IC - 12.26$	0.72	65.5	7.9

ALICMS	Linear regression equation	Correlation coefficient	RMSE [flash / 5min]	NRMSE [%]
CG	$2.22 \times 10^{-8} \times ALICMS - 3.22$	0.72	16.6	8.7
IC	$6.08 \times 10^{-8} \times ALICMS - 10.39$	0.65	54.1	8.5
CGp	$0.23 \times 10^{-8} \times ALICMS - 0.32$	0.51	3.0	10.1
TTL	$8.29 \times 10^{-8} \times ALICMS - 13.62$	0.68	68.9	8.3

The V35IC showed a higher correlation than GHV for all lightning types. The linear regression slope was 0.066 for CG, 0.18 for IC, 0.0071 for CGp, and 0.25 for TTL, all of which are slightly smaller than those for GHV for all lightning types. After comparing Figs. 4.6(a), (d), (g), (j) and (b), (e), (h), (k), V35IC showed a 10–20% larger value than GHV for the same flash rate for all lightning types. This is because V35IC contains ice-related particle volume in addition to graupel and hail, and is, therefore, larger than GHV. This relationship between GV and VOL35 is similar to that described by Carey et al. (2019). The NRMSE of V35IC was smaller than that of GHV and ALICMS in terms of all lightning types. The VOL35 used by Basarab et al. (2015) had a linear regression slope of 0.072 and an NRMSE of 12.4%. Comparing the V35IC of TTL with the same units in Basarab et al.'s results, the linear regression slope in this study is smaller and the NRMSE is better.

The linear correlation coefficient of ALICMS is the mid-value between GHV and V35IC, and the NRMSE of ALICMS revealed a similar result (Table 4.3). For all lightning types, the ALICMS and lightning flash rate plots demonstrated some scatter but no bias (Figs. 4.6(c), (f), (i), (l)). The slope of TTL (five min^{-1}) for ALICMS was 8.3×10^{-8}. According to Basarab et al. (2015), the slope of the LMA flash rate (min^{-1}) for precipitating ice mass was 1.2×10^{-7}, while the slope of the LMA flash rate for graupel mass, as demonstrated by Carey et al. (2019), was 5.08×10^{-8}. Although it is difficult to directly compare these results because the definitions of the microphysical properties were different, the difference between the studies may be due to the fact that converted ice mass has a larger difference than the volumes in a thunderstorm. According to Ryan (1996), the intercept parameter N_0, which formed part of the conversion equation, varies according to geophysical location and temperature. In this study, the intercept parameter $N_0 = 4 \times 10^6\ m^{-4}$, as adopted by Carey and Rutledge (2000) in their tropical convection modeling, was used. However, further research is needed to allow us to set more appropriate N0 values.

Overall, GHV showed similar results as those found in previous studies. V35IC showed the highest correlation coefficient, and the smallest NRMSE, while ALICMS showed a mid-value between GHV and V35IC. The correlation coefficients of this study are slightly smaller than those in previous studies (see Table 1.2). Further investigation is also needed to clarify the reason for this.

4.3.4 Relationship between lightning type and the vertical distribution of the microphysical parameters

In the previous section, the relationships between the microphysical properties of the entire thunderstorm and the flash rate were investigated. Here, the author discusses the relationship between the volume of the thunderstorm, as classified according to temperature altitude, and lightning flash type. As indicated in NIC theory, in a thunderstorm, there are generally positive charges due to ice in the upper part, negatively charged graupel and ice in the middle part, and positive charges due to graupel in the lower part (Takahashi 1984; Ziegler and MacGorman 1994). The correlations of flash rate with volume above and below temperature thresholds of −5 °C, −10 °C, −15 °C, −20 °C, and − 25 °C are shown in Fig. 4.7.

The correlation coefficients of GHV in the warmer part of the thunderstorm at −5 °C were lower than with other temperature thresholds in terms of all flash types (Figs. 4.7(a), (d), (g), (j)). This suggests that any graupel or hail in the warmer region contributes relatively less to the electrification of a thunderstorm. NIC theory indicates that the presence of graupel at temperatures colder than −10 °C is more important than that within a warmer region, which is consistent with our result. Here, the correlation of GHV in the lower part of the thunderstorm at any temperature threshold was consistently smaller than that for the whole thunderstorm and for the upper part. The correlation of GHV in the upper part gradually increased in colder thresholds. In terms of IC and TTL, high correlations exceeding 0.8 were revealed. However, the data amount decreased due to the nonexistence of microphysical particles in the colder temperature region that exceeded the radar echo top. Meanwhile, the presence of graupel or hail in the colder region suggests that a thunderstorm has strong updrafts and develops to high altitudes (Heymsfield 1983; Miller et al. 1990; Tessendorf et al. 2005; Barnes and Houze 2014). Elsewhere, Deierling and Petersen (2008) revealed a high correlation ($r = 0.93$) between TTL and an updraft volume of stronger than 5 m s^{-1}. Assuming that the existence of GHV in a colder temperature region is a proxy for the strong updraft, it holds that a higher correlation for GHV indicates a colder region. Based on NIC theory, the reason why CGp and GHV had a higher correlation with the colder region may relate to how the positively charged ice or snow particles carried to the upper part of the thunderstorm, but this is not verified in this study. In fact, this verification requires the confirmation of the initiation

point of CGp and the attendant class of hydrometeor through 3D lightning observation such as LMA and HCA via dual-polarization radar.

Unlike the correlation coefficients of GHV, the those of V35IC in the warmer part of the thunderstorm at −5 °C demonstrated no decrease (Figs. 4.7(b), (e), (h), (k)). For CG and V35IC, the colder temperature threshold of the upper part of the thunderstorm demonstrated a higher correlation coefficient, much like for GHV. With the exception of the upper part of the thunderstorm at a − 25 °C threshold, the correlation for the entire thunderstorm in terms of V35IC and ALICMS was higher in relation to CG flash rate. This is because snow and ice were widely distributed throughout the thunderstorm and had less locality than the graupel or hail (Tessendorf et al. 2005; Barnes and Houze 2014). ALICMS demonstrated the smallest variation in temperature threshold for CG (Fig. 4.7(c)). Similar to V35IC, ALICMS demonstrated no decrease in terms of the correlation coefficient of the lower part of the thunderstorm at the −5 °C threshold in relation to all types of lightning (Figs. 4.7(c), (f), (i), (l)). The difference of correlation coefficients for GHV and the others in this warm region was caused by including/excluding of snow and ice crystals. It is possible that the charge enhancement due to ice crystal formation by Hallett-Mossop processes in the lower part of cumulonimbus in the developing stage (Mansell and Ziegler 2013) contributed, although this study does not have enough data to prove this hypothesis. The correlation coefficient of ALICMS for IC and TTL was higher at the colder thresholds, which was not the case for CG. This suggests that the existence of ice-related particles in the colder part of thunderstorms is more correlated with IC and TTL than with CG.

The correlations for CGp demonstrated a similar variety as for IC and TTL at any threshold (Figs. 4.7(g)–(i)) and the lowest correlation with the warmer part of the thunderstorm in terms of GHV. According to NIC theory, this low correlation would be inconsistent if the positive charge in the lower part of a thunderstorm related to CGp is carried by the positively charged graupel. Conversely, if the positive charge of the upper part of a thunderstorm is carried by the positively charged ice particles related to CGp, it will follow that the correlation becomes higher at colder temperatures. However, this requires further investigation in terms of observing the initiation and propagation height of the CGp through 3D lightning observation methods such as LMA, and is not verified in this study.

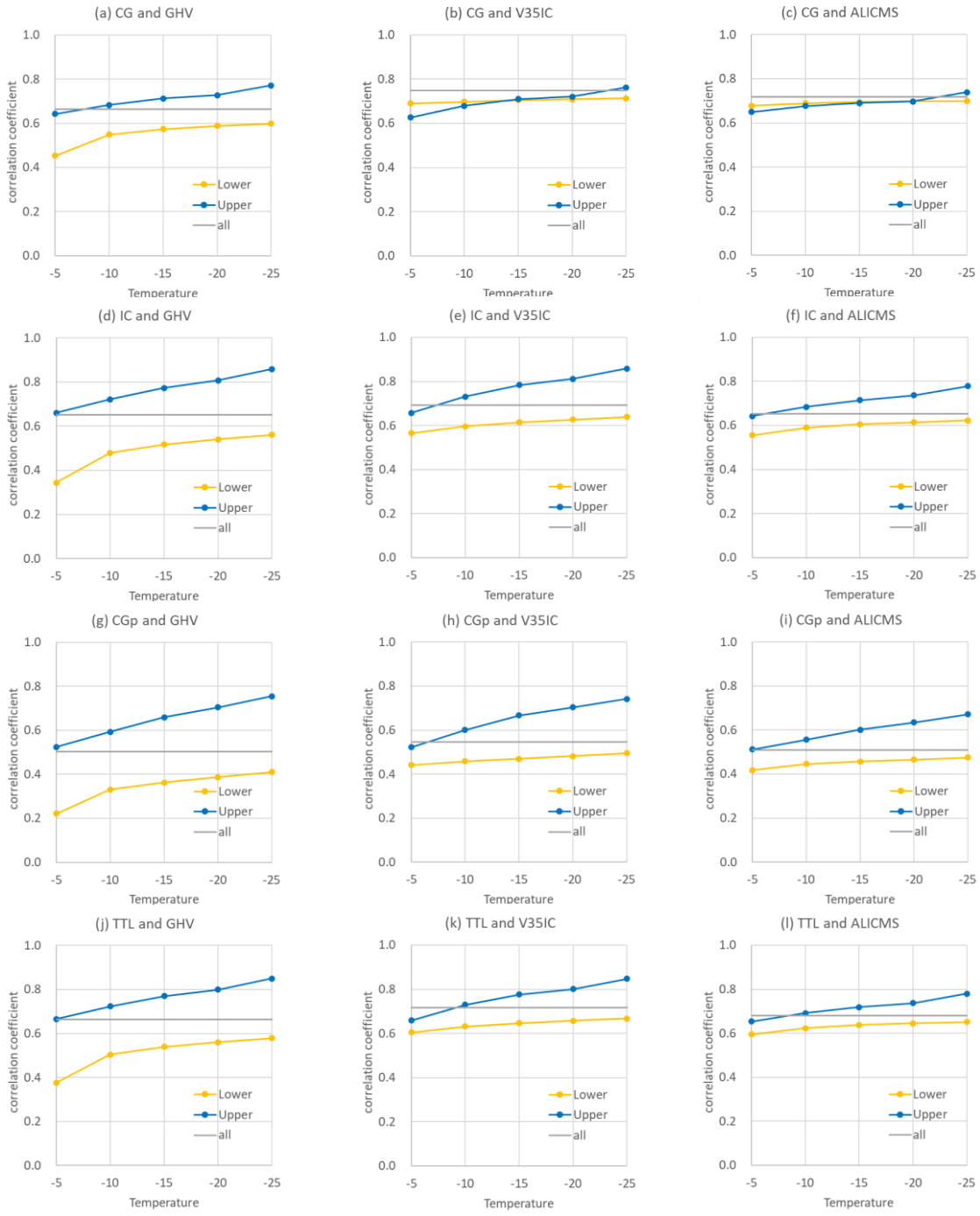

Figure 4.7 Correlations between the part of the volume (lower, yellow; upper, blue; entire cloud, gray) in the thunderstorm and the lightning flash rate according to temperature threshold.

(a) CG vs. GHV, (b) CG vs. V35IC, (c) CG vs. ALICMS,

(d) IC vs. GHV, (e) IC vs. V35IC, (f) IC vs. ALICMS,

(g) CGp vs. GHV, (h) CGp vs. V35IC, (i) CGp vs. ALICMS,

(j) TTL vs. GHV, (k) TTL vs. V35IC, (l) TTL vs. ALICMS.7

4.3.5 Time-lag correlation for nowcasting

Sections 4.3.2 and 4.3.3 revealed that the microphysical properties of the dual-polarization radar using HCA have a high correlation with lightning flash rate. To investigate the possibility of using these relationships for nowcasting, time-lag correlations for GHV, V35IC and ALICMS were calculated every 5 min from 0 min to −30 min prior to lightning activity (Fig. 4.8). Here, the correlation coefficient of GHV decreased rapidly to −15 min, while the correlations for IC and TTL demonstrated a particularly high decrease compared with those for CG. The correlation coefficient of V35IC for CG decreased more slowly (r = 0.75–0.65 in 30 min) than for GHV (r = 0.67–0.54). Much like with GHV, the correlation coefficients of V35IC for IC and TTL demonstrated a rapid decrease in correlation coefficient up to −15 min. Meanwhile, ALICMS demonstrated a gradual decrease in correlation coefficient for all lightning types. Contrary to previous studies (e.g., Goodman et al. 1988; MacGorman et al. 2011; Schultz et al. 2011), where it was found that TTL precedes CG as a precursor, TTL had a lower correlation coefficient than CG at any time point in the present study. While this difference may be related to locality, case specificity or the lightning observation system, the reason for it remains unclear. The change in GHV is related to the increase and decrease in updraft intensity and volume in the core region of thunderstorms (Tessendorf et al. 2005; Lerach et al. 2010; Barnes and Houze 2014). However, ALICMS, which included all ice-related particles, was generated through the entire thunderstorm by the weak to strong updraft region. Therefore, the time-lag correlation may be better over a longer time period because the timescale of ALICMS is longer than that of GHV. Previous studies have pointed out that charge generation begins 10–20 min before the lightning initiation (Takahashi 1978; Dye et al. 1986; Bringi et al. 1997). In more severe convection, the time-lag between the charge generation and lightning initiation reduces to a few minutes (e.g., Bruning and MacGorman 2013; Calhoun et al. 2014; Schultz et al. 2015). To verify the relationship between these studies and the time-lag, it is necessary to analyze both the updraft and the HCA with lightning, and this is a topic for the future. While these results are not directly applicable to lightning nowcasting, they do indicate the possibility of using microphysical properties in terms of HCA for better lightning nowcasting, especially with regard to V35IC and ALICMS.

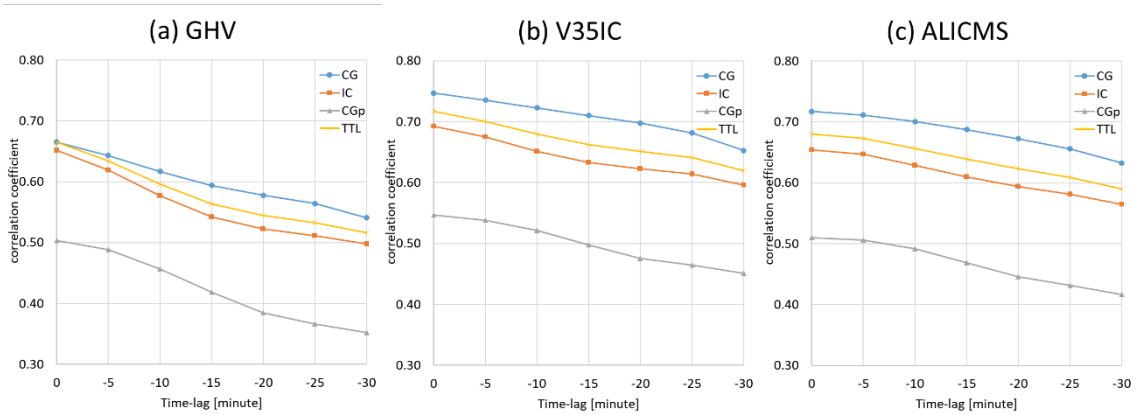

Figure 4.8 Time-lag correlations from 0 min to −30 min for (a) GHV, (b) V35IC, and (c) ALICMS for each lightning flash type.

4.3.6 Generality of the present results

Lightning indices using radar-derived parameters are proposed in this chapter. This survey was conducted under limited conditions for isolated thunderstorms only. The author examines the environments in which these proposed lightning indices can be applied.

The number of CG per day that occurred within 120 km from the NRT-DP-DRAW for 2017 and 2018 was investigated (Fig. 4.1(a)). Table 4.4 shows the number of days categorized by the number of CG and the categories to which this chapter's cases apply. Of the 730 days in the two years, 52 days exceeded 100 CG, and 18 days exceeded 1,000 CG. Mora et al. (2015) investigated thunderstorm days and the number of CG throughout Spain, and setting CG >= 2 days as indicating a thunderstorm day and exceeding 2,000 CG per day as a severe thunderstorm day (1,138 days and 72 days, respectively). In their study, approximately 6% of thunderstorm days were defined as "severe." This ratio is consistent with results shown in Table 4.4, where 18 days exceeding 1,000 CG represents 6.1% of 292 days exceeding 1 CG. In this section, 1,000 CG is defined as a severe thunderstorm day.

The synoptic patterns of 18 days exceeding 1,000 CG are classified in Table 4.5 by subjective classification derived from the weather map. Five of the 18 days that exceeded 1,000

CG per day were included in this study. Accordingly, on severe thunderstorm days, the number of days affected by an anticyclone was eight days. The number of days affected by an extratropical cyclone and a front was nine days. Since this study targeted isolated thunderstorms, it included four cases that occurred on a clear sky day with an anticyclone and only one case with another synoptic pattern. Accordingly, the analysis of thunderstorms associated with various synoptic patterns was insufficient even in severe thunderstorms. As such, further investigation of the relationship between lightning and radar parameters in various synoptic patterns is required.

Table 4.4 The number of categorized lightning days in the Kanto Plain for the 2017 and 2018 summer seasons.

Number of CG / 1day	Days	Cases in Chapter 4
=0	438	
>=1	292*	
>=10	138*	
>=100	52*	Case 1, 5, 6, 8, 10
>=1000	18*	Case 2, 3, 4, 7, 9
>=10000	1	

* Includes the number of days in the upper ranks.

Table 4.5 Synoptic patterns exceeding 1,000 CG per day for the 2017 and 2018 summer seasons.

Synoptic pattern	Severe thunderstorm days	Severe cases in Chapter 4
Anticyclone	8	Case 2, 3, 7, 9
Extratropical cyclone	5	
Front	4	Case 4
Other	1	

4.4 Summary and conclusion

The relationships between the microphysical properties retrieved from the NRT-DP-DRAW using HCA and the lightning flash rate for each lightning type observed by LIDEN were investigated. Clarifying these relationships is important for lightning nowcasting and the prediction of lightning development and cessation. The author used 351 volume scan data at five min intervals and a flash rate (five min^{-1}) for 10 cases, which were selected as isolated thunderstorms observed within the radar detection range, from their initiation to cessation in the summer periods of the Kanto Plain in Japan. These isolated thunderstorms were distinguishable from the surrounding radar echoes and lightning activity, and their entire lifecycle was tracked. For this dataset, the microphysical properties related to lightning flash rate were evaluated with reference to previous studies. GHV demonstrated better correlations, which was similar to GV investigated by Carey et al. (2019), while V35IC demonstrated the highest correlation (r = 0.75) and the lowest NRMSE (NRMSE = 8.3%). V35IC demonstrated a higher correlation than V35F (r = 0.64) without considering the particle type. While V35IC in this instance was similar to VOL35 used in both Liu et al. (2012) and Basarab et al. (2015), it incorporated HCA to remove raindrops and rain-related particles. This incorporation suggested that excluding raindrops and rain-related droplets from the radar reflectivity volumes, which were not part of NIC theory, and including all ice-related particle volumes were important for obtaining a better relationship between lightning activity and microphysical properties. ALICMS demonstrated the second highest correlation (r = 0.72), which was in line with the second highest correlation for a precipitating ice mass found by Basarab et al. (2015). GHV and V35IC slope coefficients for lightning flash rates were similar to those found by Basarab et al. (2015) and Carey et al. (2019); thus, these may be common parameters for land regardless of geographical variability. It was established the relationship between the size of a thunderstorm and lightning activity would differ depending on whether it takes place over an ocean or land (Yoshida et al. 2009). Further investigation is required to determine whether the relationship found here holds for ocean thunderstorms. The correlation coefficients of this study are slightly smaller than those in previous studies (see Table 1.2). Further investigation is also needed to clarify the reason for this. The slope coefficient for the flash rate of ALICMS differed from that found in the previous studies, which

may indicate the dependency of geographical locality or case variability in terms of the N_0 factor included in the equation for converting radar reflectivity to ice mass (Carey and Rutledge 2000). Clarifying these differences would require observational studies or sensitivity experiments involving numerical simulations.

The relationship between the microphysical properties and flash rate was investigated by dividing the temperature threshold. As a result, GHV of the part warmer than −5 °C demonstrated low correlations, while GHV of the part colder than −25 °C demonstrated high correlations. The charged graupel/hail particles produced by the NIC theory above the freezing level may have a higher correlation coefficient due to advection and accumulation in the colder temperature region. Since graupel or hail in the colder region is considered a strong updraft proxy (Heymsfield 1983; Miller et al. 1990), a robust correlation is assumed between lightning activity and updraft (Deierling and Petersen 2008), which is consistent with the high correlation for GHV. Meanwhile, V35IC and ALICMS demonstrated no decrease in correlation in the upper part of the thunderstorm. Like GHV, the higher correlation was found at the colder temperature threshold, while the increment was less gradual than GHV. This was because snow and ice were widely distributed throughout the thunderstorm and a lower degree of locality (Barnes and Houze 2014). GHV and CGp demonstrated a low correlation in the lower part of the thunderstorm, while GHV and V35IC demonstrated a higher correlation in the upper part. This suggested that the positive charge in the thunderstorm that caused the CGp had not been due to the lower level of graupel but the upper ice particles. However, this verification requires further investigation to observe the initiation and propagation height of CGp via 3D observation methods such as LMA. When the time-lag correlation was obtained from the time-series dataset, it was found that the GHV correlation coefficient decreased rapidly up to −15 min. Overall, V35IC and ALICMS demonstrated a slow decrease in the time correlation. These results encourage the application of V35IC and ALICMS for deriving a lightning nowcast index.

To accurately verify the effects of ice-related particle distributions for lightning indices, it is necessary to analyze both the updraft intensity and the particle distribution within a thunderstorm. This is an issue that must be addressed in future research. Overall, CG demonstrated a higher correlation with the radar parameters compared with TTL for all indices.

Interestingly, in this study, TTL was not a precursor for CG. These results do not correspond with those presented in previous studies (e.g., Goodman et al. 1988; MacGorman et al. 2011; Seroka et al. 2012). Recent studies have shown that ground-based CG observations like those used in the present study detect only part of multiple lightning with a wide spatial extent compared with observations by LMA or GLM (Harkema et al. 2019; Lang et al. 2017; Lyons et al. 2020). The ground-based observation used in this study did not capture such a detailed lightning structure, therefore, the relationship between TTL and CG may be one of the reasons that differed from the previous studies. It is necessary to investigate whether these differences were due to case variances, based on regionality, or measuring instrument differences.

References of Chapter 4

Akita, M., S. Yoshida, Y. Nakamura, T. Morimoto, T. Ushio, Z. Kawasaki, and D. Wang, 2011: Effects of charge distribution in thunderstorms on lightning propagation paths in Darwin, Australia. *Journal of the Atmospheric Sciences*, **68**, 719-726, https://doi.org/10.1175/2010JAS3597.1

Aydin, K., T. A. Seliga, and V. Balaji, 1986: Remote sensing of hail with a dual linear polarization radar. *Journal of climate and applied meteorology*, **25**, 1475-1484, https://doi.org/10.1175/1520-0450(1986)025%3C1475:RSOHWA%3E2.0.CO;2

Barnes, H. C., and R. A. Houze, 2014: Precipitation hydrometeor type relative to the mesoscale airflow in mature oceanic deep convection of the Madden–Julian Oscillation. *Journal of Geophysical Research: Atmospheres*, **119**, 13990-14014, https://doi.org/10.1002/2014JD022241

Basarab, B. M., S. A. Rutledge, and B. R. Fuchs, 2015: An improved lightning flash rate parameterization developed from Colorado DC3 thunderstorm data for use in cloud-resolving chemical transport models. *Journal of Geophysical Research: Atmospheres*, **120**, 9481-9499, https://doi.org/10.1002/2015JD023470

Bovalo, C., C. Barthe, and J. P. Pinty, 2019: Examining relationships between cloud-resolving model parameters and total flash rates to generate lightning density maps. *Quarterly Journal of the Royal Meteorological Society*, **145**, 1250-1266, https://doi.org/10.1002/qj.3494

Bringi, V. N., K. Knupp, A. Detwiler, L. Liu, I. J. Caylor, and R.A. Black, 1997: Evolution of a Florida thunderstorm during the convection and precipitation/electrification experiment: the case of 9 August 1991. *Monthly weather review*, **125**, 2131-2160, https://doi.org/10.1175/1520-0493(1997)125%3C2131:EOAFTD%3E2.0.CO;2

Bruning, E. C., and D. R. MacGorman, 2013: Theory and observations of controls on lightning flash size spectra. *Journal of the Atmospheric Sciences*, **70**, 4012-4029, https://doi.org/10.1175/JAS-D-12-0289.1

Bruning, E. C., W. D. Rust, T. J. Schuur, D. R. MacGorman, P. R. Krehbiel, and W. Rison, 2007: Electrical and polarimetric radar observations of a multicell storm in TELEX. *Monthly weather review*, **135**, 2525-2544, https://doi.org/10.1175/MWR3421.1

Calhoun, K. M., D. R. MacGorman, C. L. Ziegler, and M. I. Biggerstaff, 2013: Evolution of lightning activity and storm charge relative to dual-doppler analysis of a high-precipitation supercell storm. *Monthly weather review*, **141**, 2199-2223, https://doi.org/10.1175/MWR-D-12-00258.1

Calhoun, K. M., E. R. Mansell, D. R. MacGorman, and D. C. Dowell, 2014: Numerical simulations of lightning and storm charge of the 29–30 May 2004 Geary, Oklahoma, supercell thunderstorm using EnKF mobile radar data assimilation. *Monthly weather review*, **142**, 3977-3997, https://doi.org/10.1175/MWR-D-13-00403.1

Carey, L. D., and S. A. Rutledge, 1996: A multiparameter radar case study of the microphysical and kinematic evolution of a lightning producing storm. *Meteorology and Atmospheric Physics,* **59**, 33-64, https://doi.org/10.1007/BF01032000

Carey, L. D., and S. A. Rutledge, 2000: The relationship between precipitation and lightning in tropical island convection: a c-band polarimetric radar study. *Monthly weather review*, **128**, 2687-2710, https://doi.org/10.1175/1520-0493(2000)128%3C2687:TRBPAL%3E2.0.CO;2

Carey, L. D., E. V. Schultz, C. J. Schultz, W. Deierling, W. A. Petersen, A. L. Bain, and K. E. Pickering, 2019: An evaluation of relationships between radar-inferred kinematic and microphysical parameters and lightning flash rates in Alabama storms. *Atmosphere*, **10**, 796, https://doi.org/10.3390/atmos10120796

Deierling, W., and W. A. Petersen, 2008: Total lightning activity as an indicator of updraft characteristics. *Journal of Geophysical Research: Atmospheres*, **113**, D16210, https://doi.org/10.1029/2007JD009598

Deierling, W., J. Latham, W. A. Petersen, S. M. Ellis, and H. J. Christian Jr., 2005: On the relationship of thunderstorm ice hydrometeor characteristics and total lightning measurements. *Atmospheric Research,* **76**, 114-126, https://doi.org/10.1016/j.atmosres.2004.11.023

Deierling, W., W. A. Petersen, J. Latham, S. Ellis, and H. J. Christian, 2008: The relationship between lightning activity and ice fluxes in thunderstorms. *Journal of Geophysical Research: Atmospheres*, **113**, D15210, https://doi.org/10.1029/2007JD009700

Dye, J. E., J. J. Jones, W. P. Winn, T. A. Cerni, B. Gardiner, D. Lamb, R. L. Pitter, J. Hallett, and C. P. R. Saunders, 1986: Early electrification and precipitation development in a small, isolated Montana cumulonimbus. *Journal of Geophysical Research: Atmospheres*, **91**, https://doi.org/10.1029/JD091iD01p01231

Dye, J. E., W. P. Winn, J. J. Jones, and D. W. Breed, 1989: The electrification of New Mexico thunderstorms, 1. Relationship between precipitation development and the onset of electrification. *Journal of Geophysical Research: Atmospheres*, **94**, 8643-8656, https://doi.org/10.1029/JD094iD06p08643

Goodman, S. J., D. E. Buechler, P. D. Wright, and W. D. Rust, 1988: Lightning and precipitation history of a microburst-producing storm. *Geophysical Research Letters*, **15**, 1185-1188, https://doi.org/10.1029/GL015i011p01185

Goodman, S. J., and Coauthors, 2013: The GOES-R geostationary lightning mapper (GLM). *Atmospheric research,* **125**, 34-49, https://doi.org/10.1016/j.atmosres.2013.01.006

Gremillion, M. S., and R. E. Orville, 1999: Thunderstorm characteristics of cloud-to-ground lightning at the Kennedy Space Center, Florida: A study of lightning initiation signatures

as indicated by the WSR-88D. *Weather and Forecasting*, **14**, 640-649, https://doi.org/10.1175/1520-0434(1999)014%3C0640:TCOCTG%3E2.0.CO;2

Hall, M. P. M., J. W. F. Goddard, and S. M. Cherry, 1984: Identification of hydrometeors and other targets by dual–polarization radar. *Radio Science,* **19**, 132-140, https://doi.org/10.1029/RS019i001p00132

Harkema, S. S., C. J. Schultz, E. B. Berndt, and P. M. Bitzer, 2019: Geostationary lightning mapper flash characteristics of electrified snowfall events. *Weather and Forecasting*, **34**, 1571-1585, https://doi.org/10.1175/WAF-D-19-0082.1

Heymsfield, A. J., 1983: Case study of a hailstorm in Colorado. Part IV: Graupel and hail growth mechanisms deduced through particle trajectory calculations. *Journal of the Atmospheric Sciences*, **40**, 1482-1509, https://doi.org/10.1175/1520-0469(1983)040<1482:CSOAHI>2.0.CO;2

Honda, Y., M. Nishijima, K. Koizumi, Y. Ohta, K. Tamiya, T. Kawabata, and T. Tsuyuki, 2005: A pre-operational variational data assimilation system for a nonhydrostatic model at Japan Meteorological Agency: formulation and preliminary results. *Quarterly Journal of the Royal Meteorological Society,* **131**, 3465-3475, https://doi.org/10.1256/qj.05.132

Ishii, K., S. Hayashi, and F. Fujibe, 2014: Statistical analysis of temporal and spatial distributions of cloud-to-ground lightning in Japan from 2002 to 2008. *Journal of Atmospheric Electricity*, **34**, 79-86, https://doi.org/10.1541/jae.34.79

Krehbiel, P., T. Chen, S. McCrary, W. Rison, G. Gray, and M. Brook, 1996: The use of dual channel circular-polarization radar observations for remotely sensing storm electrification. *Meteorology and Atmospheric Physics,* **59**, 65-82, https://doi.org/10.1007/BF01032001

Lang, T. J., and Coauthors, 2017: WMO world record lightning extremes: longest reported flash distance and longest reported flash duration. *Bulletin of the American Meteorological Society,* **98**, 1153-1168, https://doi.org/10.1175/BAMS-D-16-0061.1

Lerach, D. G., S. A. Rutledge, C. R. Williams, and R. Cifelli, 2010: Vertical structure of convective systems during NAME 2004. *Monthly Weather Review*, **138**, 1695-1714, https://doi.org/10.1175/2009MWR3053.1

Liu, C., D. J. Cecil, E. J. Zipser, K. Kronfeld, and R. Robertson, 2012: Relationships between lightning flash rates and radar reflectivity vertical structures in thunderstorms over the tropics and subtropics. *Journal of Geophysical Research: Atmospheres*, **117**, D06212, https://doi.org/10.1029/2011JD017123

López, R. E., and J. P. Aubagnac, 1997: The lightning activity of a hailstorm as a function of changes in its microphysical characteristics inferred from polarimetric radar observations. *Journal of Geophysical Research: Atmospheres*, **102**, 16799-16813, https://doi.org/10.1029/97JD00645

Lund, N. R., D. R. MacGorman, T. J. Schuur, M. I. Biggerstaff, and W. D. Rust, 2009: Relationships between lightning location and polarimetric radar signatures in a small mesoscale convective system. *Monthly Weather Review*, **137**, 4151-5170, https://doi.org/10.1175/2009MWR2860.1

Lyons, W. A., E. C. Bruning, T. A. Warner, D. R. MacGorman, S. Edgington, C. Tillier, and J. Mlynarczyk, 2020: Megaflashes: just how Long can a lightning discharge get? *Bulletin of the American Meteorological Society,* **101**, E73-E86, https://doi.org/10.1175/BAMS-D-19-0033.1

MacGorman, D. R., I. R. Apostolakopoulos, N. R. Lund, N. W. Demetriades, M. J. Murphy, and P. R. Krehbiel, 2011: The timing of cloud-to-ground lightning relative to total lightning activity. *Monthly Weather Review*, **139**, 3871–3886. https://doi.org/10.1175/MWR-D-11-00047.1

Makihara, Y., N. Uekiyo, A. Tabata, and Y. Abe, 1996: Accuracy of radar-AMeDAS precipitation. *IEICE Transactions on Communications,* **E79-B**, 751-762.

Mansell, E. R., and C. L. Ziegler, 2013: Aerosol effects on simulated storm electrification and precipitation in a two-moment bulk microphysics model. *Journal of the Atmospheric Sciences*, **70**, 2032-2050, https://doi.org/10.1175/JAS-D-12-0264.1

Mecikalski, R. M., A. L. Bain, and L. D. Carey, 2015: Radar and lightning observations of deep moist convection across northern Alabama during DC3: 21 May 2012. *Monthly Weather Review*, **143**, 2774-2794, https://doi.org/10.1175/MWR-D-14-00250.1

Miller, L. J., J. D. Tuttle, and G. B. Foote, 1990: Precipitation production in a large Montana hailstorm: airflow and particle growth trajectories. *Journal of the Atmospheric Sciences*, **47**, 1619-1646, https://doi.org/10.1175/1520-0469(1990)047<1619:PPIALM>2.0.CO;2

Mora, M., J. Riesco, F. de Pablo Dávila, and L. Rivas Soriano, 2015: Atmospheric background associated with severe lightning thunderstorms in Central Spain. *International Journal of Climatology,* **35**, 558-569. https://doi.org/10.1002/joc.4002

Mosier, R. M., C. Schumacher, R. E. Orville, and L. D. Carey, 2011: Radar nowcasting of cloud-to-ground lightning over Houston, Texas. *Weather and Forecasting*, **26**, 199–212, https://doi.org/10.1175/2010WAF2222431.1

Rison, W., R. J. Thomas, P. R. Krehbiel, T. Hamlin, and J. Harlin, 1999: A GPS-based three-dimensional lightning mapping system: initial observations in Central New Mexico. *Geophysical Research Letters,* **26**, 3573-3576, https://doi.org/10.1029/1999GL010856

Ryan, B.F., 1996: On the global variation of precipitating layer clouds. *Bulletin of the American Meteorological Society,* **77**, 53-70, https://doi.org/10.1175/1520-0477(1996)077<0053:OTGVOP>2.0.CO;2

Saunders, C. P. R., S. L. Peck, 1998: Laboratory studies of the influence of the rime accretion rate on charge transfer during crystal/graupel collisions. *Journal of Geophysical Research: Atmospheres,* **103**, 13949–13956. https://doi.org/10.1029/97JD02644

Schultz, C. J., W. A. Petersen, and L. D. Carey, 2011: Lightning and severe weather: a comparison between total and cloud-to-ground lightning trends. *Weather and Forecasting,* **26**, 744-755, https://doi.org/10.1175/WAF-D-10-05026.1

Schultz, C. J., L. D. Carey, E. V. Schultz, and R. J. Blakeslee, 2015: Insight into the kinematic and microphysical processes that control lightning jumps. *Weather and Forecasting,* **30**, 1591-1621, https://doi.org/10.1175/WAF-D-14-00147.1

Seroka, G. N., R. E. Orville, and C. Schumacher, 2012: Radar nowcasting of total lightning over the Kennedy Space Center. *Weather and Forecasting,* **27**, 189-204, https://doi.org/10.1175/WAF-D-11-00035.1

Shafer, M. A., D. R. MacGorman, and F. H. Carr, 2000: Cloud-to-ground lightning throughout the lifetime of a severe storm system in Oklahoma. *Monthly Weather Review*, **128**, 1798–1816, https://doi.org/10.1175/1520-0493(2000)128%3c1798:CTGLTT%3e2.0.CO;2

Stolzenburg, M., and T. C. Marshall, 1998: Charged precipitation and electric field in two thunderstorms. *Journal of Geophysical Research: Atmospheres,* **103**, 19777-19790, https://doi.org/10.1029/98JD01675

Stolzenburg, M., T. C. Marshall, and P. R. Krehbiel, 2015: Initial electrification to the first lightning flash in New Mexico thunderstorms. *Journal of Geophysical Research: Atmospheres,* **120**, 11253-11276, https://doi.org/10.1002/2015JD023988

Takahashi, T., 1978: Riming electrification as a charge generation mechanism in thunderstorms. *Journal of the Atmospheric Sciences*, **35**, 1536–1548, https://doi.org/10.1175/1520-0469(1978)035<1536:REAACG>2.0.CO;2

Takahashi, T., 1984: Thunderstorm electrification—a numerical study. *Journal of the Atmospheric Sciences*, **41**, 2541–2558, https://doi.org/10.1175/1520-0469(1984)041<2541:TENS>2.0.CO;2

Tessendorf, S. A., L. J. Miller, K. C. Wiens, and S. A. Rutledge, 2005: The 29 June 2000 supercell observed during STEPS. Part I: kinematics and microphysics. *Journal of the Atmospheric Sciences*, **62**, 4127-4150, https://doi.org/10.1175/JAS3585.1

Tsukamoto, N., H. Yamauchi, H. Okumura, A. Umehara, and Y. Kajiwara, 2016: JMA's C-band dual-polarization Doppler weather radars with SSPAs. *WMO/CIMO/TECO-2016*, Madrid, Spain, https://www.wmo.int/pages/prog/www/IMOP/publications/IOM-125_TECO_2016/Session_2/P2(68)%20Tsukamoto_JMA-radars.pdf

Umehara, A., T. Koike, K. Yamamoto, N. Nagumo, and H. Yamauchi, 2019: Development of a practical hydrometeor classification algorithm via a Bayesian approach using C-band dual-polarization radar. *39th International Conference on Radar Meteorology*, Nara, Japan, Poster2-63, https://cscenter.co.jp/icrm2019/program/data/abstracts/Poster2-63.pdf

van Lier-Walqui, M., A. M. Fridlind, A. S. Ackerman, S. Collis, J. Helmus, D. R. MacGorman, K. North, P. Kollias, and D. J. Posselt, 2016: On polarimetric radar signatures of deep convection for model evaluation: columns of specific differential phase observed during MC3E. *Monthly Weather Review*, **144**, 737-758, https://doi.org/10.1175/MWR-D-15-0100.1

Vincent, B. R., L. D. Carey, D. Schneider, K. Keeter, and R. Gonski, 2005: Using WSR-88D reflectivity for the prediction of cloud-to-ground lightning: a central North Carolina study. *Conf. on Meteorological Applications of Lightning Data*, San Diego, CA, American Meteorological Society, 3.2, https://ams.confex.com/ams/Annual2005/techprogram/paper_84669.htm

Vivekanandan, J., D. S. Zrnic, S. M. Ellis, R. Oye, A. V. Ryzhkov, and J. Straka, 1999: Cloud microphysics retrieval using S-band dual-polarization radar measurements. *Bulletin of the American Meteorological Society,* **80**, 381-388, https://doi.org/10.1175/1520-0477(1999)080<0381:CMRUSB>2.0.CO;2

Wang, J., S. Zhou, B. Yang, X. Meng, and B. Zhou, 2016: Nowcasting cloud-to-ground lightning over Nanjing area using S-band dual-polarization Doppler radar. *Atmospheric Research,* **178**, 55-64, https://doi.org/10.1016/j.atmosres.2016.03.007

Yoshida, S., T. Morimoto, T. Ushio, and Z. Kawasaki, 2009: A fifth-power relationship for lightning activity from Tropical Rainfall Measuring Mission satellite observations. *Journal of Geophysical Research: Atmospheres,* **114**, D09104, https://doi.org/10.1029/2008JD010370

Ziegler, C. L., and D. R. MacGorman, 1994: Observed lightning morphology relative to modeled space charge and electric field distributions in a tornadic storm. *Journal of the Atmospheric Sciences*, **51**, 833-851, https://doi.org/10.1175/1520-0469(1994)051<0833:OLMRTM>2.0.CO;2

Ziegler, C. L., D. R. MacGorman, J. E. Dye, and P. S. Ray 1991: A model evaluation of noninductive graupel-ice charging in the early electrification of a mountain thunderstorm. *Journal of Geophysical Research: Atmospheres*, **96**, 12833-12855, https://doi.org/10.1029/91JD01246

Zipser, E. J., and K. R. Lutz, 1994: The vertical profile of radar reflectivity of convective cells: a strong indicator of storm intensity and lightning probability? *Monthly Weather Review*, **122**, 1751-1759, https://doi.org/10.1175/1520-0493(1994)122<1751:TVPORR>2.0.CO;2

Chapter 5
General conclusions

5.1 Conclusion

This thesis aimed to reveal the relationship between radar-derived parameters and lightning activity. It proposed lightning indices to improve lightning nowcasting. The Kanto Plain of Japan is the country's most populated and congested aviation area. It is heavily affected by lightning strikes and the damages caused by them. There is thus a strong social demand for accurate lightning prediction during summer thunderstorms. For this purpose, the statistical classification of lightning and non-lightning cells in the Kanto Plain was performed using conventional single-polarization radar with a cell-tracking method. The author also investigated the relationship between radar-derived parameters from the dual-polarization radar with HCA and lightning activity in isolated thunderstorms in the Kanto Plain.

The main conclusions are summarized as follows.

According to the characteristic type of lightning discharge, the author classified cells into CGIC, IC, and NoL cells and demonstrated statistically significant differences for each radar observation. The CGIC cells had the largest lifetime, area, echo top height, VIL, maximum radar reflectivity, and radar reflectivity at a − 10 °C isotherm height. The NoL cells yielded the lowest values and the IC cells produced intermediate values. This study demonstrated that the values of the CGIC cells were significantly different from those of the IC and NoL cells. The characteristics related to the lifetime of the CGIC, IC, and NoL cells were clarified through temporal variation of the vertical distribution of radar reflectivity. The CGIC cells had the strongest radar reflectivity above the freezing level. At 40 min after cell identification, the peak CG activity coincided with the radar reflectivity region exceeding 48 dBZ at the 0 °C to − 5 °C isotherm height, from 20 to 40 min. This feature was absent in the IC and NoL cells. The presence of a radar reflectivity region exceeding 48 dBZ above the 0 °C isotherm height, coupled with graupel occurrence and lightning initiation (see, e.g., Takahashi 1978; Jayaratne et al. 1983), suggests the presence of graupel in

this region. Additionally, temporal variations in the vertical distribution of radar reflectivity exceeding 42 dBZ appeared to correspond to CG and IC activity, suggesting a correlation between the vertical development of cumulonimbus and lightning activity. The accuracy of the lightning index using radar parameters was also evaluated. For maximum radar reflectivity, 40 dBZ at the −10 °C temperature height threshold (adopted in previous research; see Gremillion and Orville 1999) produced lower scores of 0.59 for CSI, 0.85 for PoD, and 0.34 for FAR. Conversely, a threshold of 35 dBZ at the − 30 °C height delivered better scores of 0.82 for CSI, 0.86 for PoD, and 0.06 for FAR. Strong radar reflectivity regions may explain threshold differences at lower temperatures, indicating deep vertical growth of cumulonimbi and, as such, facilitating a demonstration of the existence of graupel and charge production.

The relationships between the microphysical properties retrieved from the NRT-DP-DRAW using HCA and the lightning flash rate for each lightning type observed by LIDEN were investigated. The author used 351 volume scan radar data at five min intervals and the flash rate (five min^{-1}) for 10 cases, which were selected as isolated thunderstorms. For this dataset, the microphysical properties related to lightning flash rate were evaluated. V35IC demonstrated the highest correlation ($r = 0.75$) and the lowest NRMSE (NRMSE = 8.3%). V35IC also demonstrated a higher correlation than V35F ($r = 0.64$) when not considering particle type. V35IC incorporates HCA to remove raindrops and rain-related particles from a radar reflectivity volume greater than 35 dBZ. This result suggested that excluding raindrops and rain-related droplets from the radar reflectivity volumes, which are not part of NIC theory, and including all ice-related particle volumes were important for obtaining a better relationship between lightning activity and microphysical properties. The GHV and V35IC slope coefficients for lightning flash rates were similar to those found by both Basarab et al. (2015) and Carey et al. (2019); as such, these may be common land-based parameters, regardless of geographical variability. The relationship between the microphysical properties and flash rate was investigated by dividing the temperature threshold. As a result, the GHV of the part warmer than −5 °C demonstrated low correlations, while the GHV of the part colder than −25 °C demonstrated high correlations. The charged graupel/hail particles produced by the NIC theory above the freezing level may have a higher correlation coefficient due to advection and accumulation in the colder temperature region.

Meanwhile, V35IC and ALICMS demonstrated no decrease in correlation in the upper part of the thunderstorm. Like GHV, the higher correlations of V35IC and ALICMS were found at the colder temperature threshold while the increment was less gradual than GHV. There were because snow and ice were widely distributed throughout the thunderstorm and had less locality. When the time-lag correlation was obtained from the time-series dataset, the correlation coefficient of GHV decreased rapidly until −15 min. Overall, V35IC and ALICMS demonstrated a slow decrease in the time correlation. These results encourage the application of V35IC and ALICMS to a lightning nowcast index.

5.2 Availability of the proposed lightning indices

Selected lightning indices were proposed in the previous chapters. In this section, the author examines the possibility of using these indices in addition to the lightning nowcast.

Lightning can cause wildfires and a production source of nitrogen oxides in the atmosphere ($NO + NO_2 \rightarrow NO_x$). Estimating these changes in lightning incidence in future climate is important for determining a social response to climate change (see, e.g., Basarab et al. 2015; Carey et al. 2019). Therefore, it is important to estimate the amount of lightning from predicted physical variables in a climate prediction model. However, as noted in Chapter 1, the development of the numerical simulation of lightning with electrical processes remains ongoing; furthermore, it is impossible to directly simulate lightning using a climate prediction model as it requires enormous computing resources. Romps et al. (2014) predicted changes in lightning activity based on simulated atmospheric instability in climate models that do not directly simulate individual clouds with horizontal resolutions of tens to hundreds of kilometers (CMIP5, Taylor et al. 2012). Conversely, a climate prediction model using a cloud-resolving model with a horizontal resolution of several kilometers has in recent years progressed to the practical stage and future predictions including, such as cloud microphysical variables are becoming possible (e.g., Prein et al. 2015; Kendon et al. 2017). Furthermore, numerical weather prediction experiments that can directly represent the updraft and ice particles in thunderstorm cores within a sub-kilometer horizontal resolution are conducted (e.g., Ito et al. 2017). If the relationship between cloud microphysical variables and lightning is clarified using the results in the current thesis, it will be possible to

accurately predict lightning by incorporating the findings in a future cloud-resolving climate model. This will help improve the prediction accuracy of future climates regarding NO_x and wildfires and support social demands.

Data assimilation of lightning observations into numerical models currently underway (e.g., Mansell 2014; Wang et al. 2017; Fierro et al. 2019). With the initiation of lightning observations by the Geostationary Lightning Mapper (GLM, Goodman et al. 2013), it has become possible to accurately supplement lightning strikes on the sea, for which information had until now been scarce. The amount of ice particles is a forecast variable in the regional cloud-resolving model of the numerical weather prediction in operation. To effectively assimilate lightning observation data into a cloud-resolving model, it is necessary to associate the lightning observation amount with the cloud microphysical quantity of the numerical model (e.g., Mansell 2014; Wang et al. 2017; Fierro et al. 2019). The relationship between lightning and cloud microphysical quantities is precisely the information that is required. As noted in this section, the results obtained in this thesis have wide applicability.

5.3 Future work

Lightning indices using radar-derived parameters were proposed in Chapters 3 and 4. Both surveys were conducted under limited conditions (single day and isolated thunderstorms, respectively). Four of five cases on a severe thunderstorm day (Chapter 4) occurred on a clear sky day with an anticyclone. Accordingly, the analysis of thunderstorms associated with various synoptic patterns was insufficient even in severe thunderstorms. As noted in Chapter 1, the risk of lightning strikes exists during all seasons in Japan. Further investigation of the relationship between lightning and radar parameters in various synoptic patterns is needed. The proposed lightning indices were applied to a more different environment, and their accuracy must be verified. Reducing aircraft triggered-lightning strikes for aviation safety requires an investigation of whether these proposed indices apply to charged but no-lightning clouds.

In July 2018, a dual-polarization phased-array radar (MP-PAWR) was installed on the campus of Saitama University, located at the center of the Kanto Plain. The radar is expected to

improve the resolution of vertical and temporal data and will enable the acquisition of particle information with higher observation frequencies and accuracy than conventional parabolic antenna radar.

To accurately verify the effects of ice-related particle distributions, it is necessary to analyze updraft intensity, lightning propagation, and hydrometer particle distribution within a thunderstorm. These verifications will require further investigation in terms of observing the initiation and the propagation of lightning, which can be effected via high-precision 3D observation, e.g., LMA. Furthermore, a 3D lightning observation system has also been developed in Japan (see, e.g., Nishihashi et al. 2012; Yoshida et al. 2014). The National Research Institute for Earth Science and Disaster Resilience (NIED) research group in Japan installed LMA in the Kanto area, where is the same as this thesis, and have begun observations (Tokyo-LMA, Sakurai et al. 2019). Lightning prediction studies should be expanded by their observational data.

References of Chapter 5

Basarab, B. M., S. A. Rutledge, and B. R. Fuchs, 2015: An improved lightning flash rate parameterization developed from Colorado DC3 thunderstorm data for use in cloud-resolving chemical transport models. *Journal of Geophysical Research: Atmospheres*, **120**, 9481-9499, https://doi.org/10.1002/2015JD023470

Carey, L. D., E. V. Schultz, C. J. Schultz, W. Deierling, W. A. Petersen, A. L. Bain, and K. E. Pickering, 2019: An evaluation of relationships between radar-inferred kinematic and microphysical parameters and lightning flash rates in Alabama storms. *Atmosphere*, **10**, 796, https://doi.org/10.3390/atmos10120796

Fierro, A. O., Y. Wang, J. Gao, and E. R. Mansell, 2019: Variational assimilation of radar data and GLM lightning-derived water vapor for the short-term forecasts of high-impact convective events. *Monthly Weather Review*, **147**, 4045–4069, https://doi.org/10.1175/MWR-D-18-0421.1

Goodman, S. J., and Coauthors, 2013: The GOES-R geostationary lightning mapper (GLM). *Atmospheric research,* **125**, 34-49, https://doi.org/10.1016/j.atmosres.2013.01.006

Gremillion, M. S., and R. E. Orville, 1999: Thunderstorm characteristics of cloud-to-ground lightning at the Kennedy Space Center, Florida: A study of lightning initiation signatures as indicated by the WSR-88D. *Weather and Forecasting*, **14**, 640-649, https://doi.org/10.1175/1520-0434(1999)014%3C0640:TCOCTG%3E2.0.CO;2

Ito, J., S. Hayashi, A. Hashimoto, H. Ohtake, F. Uno, H. Yoshimura, T. Kato, and Y. Yamada, 2017: Stalled improvement in a numerical weather prediction model as horizontal resolution increases to the sub-kilometer scale. *SOLA*, **13**, 151-156, https://doi.org/10.2151/sola.2017-028

Jayaratne, E. R., C. P. R. Saunders, and J. Hallett, 1983: Laboratory studies of the charging of soft-hail during ice crystal interactions. *Quarterly Journal of the Royal Meteorological Society*, **109**, 609-630, https://doi.org/10.1002/qj.49710946111

Kendon, E. J., and Coauthors, 2017: Do convection-permitting regional climate models improve projections of future precipitation change? *Bulletin of the American Meteorological Society,* **98**, 79–93, https://doi.org/10.1175/BAMS-D-15-0004.1.

Mansell, E. R. 2014: Storm-scale ensemble Kalman filter assimilation of total lightning flash-extent data. *Monthly Weather Review*, **142**, 3683-3695, https://doi.org/10.1175/MWR-D-14-00061.1

Nishihashi, M., K. Shimose, K. Kusunoki, S. Hayashi, K. Arai, H. Y. Inoue, W. Mashiko, M. Kusume, and H. Morishima, 2012: Three-dimensional VHF lightning mapping system for winter thunderstorms. *Journal of atmospheric and oceanic technology*, **30**, 325-335, https://doi.org/10.1175/JTECH-D-12-00084.1

Prein, A. F., and Coauthors, 2015: A review on regional convection-permitting climate modeling: Demonstrations, prospects, and challenges. *Reviews of geophysics,* **53**, 323– 361. https://doi.org/10.1002/2014RG000475.

Romps, D. M., J. T. Seeley, D. Vollaro, and J. Molinari, 2014: Projected increase in lightning strikes in the United States due to global warming. *Science*, **346**, 851-854, https://doi.org/10.1126/science.1259100

Sakurai et al. 2019, Lightning characteristics of a supercell thunderstorm observed by Tokyo LMA, X-Band polarimetric radars, and an X-Band phased array weather radar in Tokyo, Japan. *Ninth Conference on the Meteorological Application of Lightning Data*. Phoenix, AZ, American Meteorological Society, Poster272, https://ams.confex.com/ams/2019Annual/meetingapp.cgi/Paper/352975

Takahashi, T., 1978: Riming electrification as a charge generation mechanism in thunderstorms. *Journal of the Atmospheric Sciences*, **35**, 1536–1548, https://doi.org/10.1175/1520-0469(1978)035<1536:REAACG>2.0.CO;2

Taylor, K. E., R. J. Stouffer, and G. A. Meehl, 2012: An overview of CMIP5 and the experiment design. *Bulletin of the American Meteorological Society,* **93**, 485-498, https://doi.org/10.1175/BAMS-D-11-00094.1

Wang, H., and Coauthors, 2017: Improving lightning and precipitation prediction of severe convection using lightning data assimilation with NCAR WRF-RTFDDA. *Journal of Geophysical Research: Atmospheres,* **122**, 12296–12316, https://doi.org/10.1002/2017JD027340

Yoshida, S., T. Wu, T. Ushio, K. Kusunoki, and Y. Nakamura, 2014: Initial results of LF sensor network for lightning observation and characteristics of lightning emission in LF band. *Journal of Geophysical Research: Atmospheres*, **119**, 12-034, https://doi.org/10.1002/2014JD022065

List of Publications

Note: This thesis is based on the articles numbered **4** and **5** of the following lists.

Peer-reviewed articles (Lead author)

1. **Hayashi, S**., 2006: Numerical simulation of electrical space charge density and lightning by using a 3-dimensional cloud-resolving model. *SOLA*, **2**. 124-127, https://doi.org/10.2151/sola.2006-032

2. **Hayashi, S.**, 2016: Statistical relationships of precipitation rate and wind gust intensity to lightning activity in Japan. *Journal of Atmospheric Electricity*, **35**, 43-51, https://doi.org/10.1541/jae.35.43

3. **Hayashi S.**, and C. Marui, 2016: Frequency and seasonal variation of single lightning flash storm, "Ippatsurai", in Japan (in Japanese). *Journal of Atmospheric Electricity*, **36**, 13-22, https://doi.org/10.1541/jae.36.13

4. **Hayashi, S**., C. Nakaike, and F. Fujibe, 2021: Radar characteristics of summer thunderstorms in the Kanto Plain of Japan with and without cloud-to-ground lightning. *Meteorology and Atmospheric Physics*. **133**, 233-244, https://doi.org/10.1007/s00703-020-00748-z

5. **Hayashi, S**., A. Umehara, N. Nagumo, and T. Ushio, 2021: The relationship between lightning flash rate and ice-related volume derived from dual-polarization radar. *Atmospheric Research*. **248**, 105166, https://doi.org/10.1016/j.atmosres.2020.105166

Peer-reviewed articles (co-author)

1. Nishihashi, M., K. Shimose, K. Kusunoki, **S. Hayashi,** K. Arai, H. Y. Inoue, W. Mashiko, M. Kusume, and H. Morishima, 2012: Three-dimensional VHF lightning mapping system for winter thunderstorms. *Journal of atmospheric and oceanic technology*, **30**, 325-335, https://doi.org/10.1175/JTECH-D-12-00084.1

2. Ishii, K., **S. Hayashi,** and F. Fujibe, 2014: Statistical analysis of temporal and spatial distribution of cloud-to-ground lightning in Japan from 2002 to 2008. *Journal of Atmospheric Electricity*, **34**, 79-86. https://doi.org/10.1541/jae.34.79

3. Nishihashi, M., K. Arai, C. Fujiwara, W. Mashiko, S. Yoshida, **S. Hayashi**, and K. Kusunoki, 2015: Characteristics of lightning jumps associated with a tornadic supercell on 2 September 2013. *SOLA*, **11**, 18-22, https://doi.org/10.2151/sola.2015-005

4. Yoshida, S., T. Adachi, K. Kusunoki, **S. Hayashi,** T. Wu, T. Ushio, and E. Yoshikawa, 2017: Relationship between thunderstorm electrification and storm kinetics revealed by phased array weather radar. *Journal of Geophysical Research Atmosphere*, **122**, 3821-3836, http://dx.doi.org/10.1002/2016JD025947

5. Ito, J., S. **Hayashi,** A. Hashimoto, H. Ohtake, F. Uno, H. Yoshimura, T. Kato, and Y. Yamada, 2017: Stalled improvement in a numerical weather prediction model as horizontal resolution increases to the sub-kilometer scale. *SOLA*, **13**, 151-156, https://doi.org/10.2151/sola.2017-028

6. Yoshida, S., E. Yoshikawa, T. Adachi, K. Kusunoki, **S. Hayashi,** and H. Inoue, 2018: Three dimensional radio images of winter lightning in Japan and characteristics of associated charge structure. *IEEJ Transactions on Electrical and Electronic Engineering*, **14**, 175-184, https://doi.org/10.1002/tee.22795